Development of Imaging Methods for the Lithium-Pilocarpine Model of Epilepsy

Ben Andrew Duffy

Submitted for the degree of Doctor of Philosophy

Division of Medicine, University College London

Declaration

I, Ben Andrew Duffy, confirm that the work presented in this thesis is my own. Where information has been derived from other sources, I confirm that this has been indicated in the thesis. This work is based on research which has been conducted by me during the time period of September 2010 to December 2013 at University College London, UK, Dartmouth College, USA and Tohoku University, Japan.

Ben Andrew Duffy

Abstract

Anti-inflammatory therapies are promising candidates for the prevention of brain injury following prolonged seizures (status epilepticus). Biomarkers for therapy monitoring are needed to translate these recent findings to the clinic. The aim of this thesis was to develop imaging methods that can be used to monitor anti-inflammatory therapies and monitor disease progression following prolonged seizures.

In order to achieve these goals, the lithium-pilocarpine model was used as a model of status epilepticus and novel MRI imaging methods were employed. Various imaging approaches including: quantitative, structural, molecular and functional imaging were tested for their possible investigative utility as imaging biomarkers for neuroprotective therapies. Alongside this, two different anti-inflammatory therapies were tested for their effectiveness to alter brain injury following status epilepticus.

This thesis demonstrates that molecular imaging has potential to monitor neuroprotective therapies. Surprisingly, there was little evidence that the anti-inflammatory therapies tested here had beneficial effects. However, this thesis shows that employing novel imaging approaches and automated analysis methods can enable accurate *in vivo* assessment of disease altering therapies.

Acknowledgements

Firstly, I am grateful to my supervisors: Mark Lythgoe and Rod Scott for continued support and guidance throughout my PhD. Rod has been an inspiration due to his unassailable knowledge of all things related to epilepsy and Mark always displays a boundless passion for biomedical imaging and continues to nurture an environment for learning. I am also much indebted to ManKin Choy for teaching me about animal models, perfuse fixations and for continued discussion and advice. I am thankful to Johannes Riegler for his patience and scepticism as well as much helpful scientific discussion.

The following people also actively contributed to the work contained within this project and therefore their help is greatly acknowledged: Niral Patel and Dr Erik Årstad for help with radiochemistry, Professor Matthew Walker, Professor David Gadian for valuable discussions, Katherine Ordidge, Alex Bender and Dr Radu Stan for help with cell culture, immunohistochemistry and western blotting, Dr Akira Sumiyoshi for extensive help with fMRI experiments, Dr Hideaki Suzuki for help with physiological monitoring, Sun Chun for proofreading and help with statistical analyses and Professor Ryuta Kawashima for agreeing to be my JSPS host researcher.

I also am thankful to: Ali Titiz, Kyle Jenks, Marcella Lucas, Professor Gregory Holmes as well as the other members of the Epilepsy, Cognition and Development group at Dartmouth College for making my time there so enjoyable.

I wish to thank the people who have surrounded me during my years at UCL: my friends: Adam Walters, Adam Young, Burak Gunsoy, Carla Prata, Daniel Kwan, Kimberley Hockley, Maija Maskuniity, Matthew Ash, Richard Bradshaw, and the current and past members of CABI: Adam Badar, Adrienne Campbell, Angela D'Esposito, Anthony Price, Arun Niranjan, Bernard Siow, Daniel Stuckey, Holly Holmes, Isabel Christie, Jack Wells, James O'Callaghan, Jane Kung, Laurence Jackson, Miguel Goncalves, Niall Colgan, Rupinder Ghatrora, Ma Da, Nicholas Powell, Niral Patel, Ozama Ismail, Rajiv Ramasawmy, Simon Richardson, Simon Walker-Samuel, Tammy Kalber, Tom Roberts, Valerie Taylor, Yanan Zhu, Yichao Yu.

Most importantly, my deepest gratitude goes to my parents and my brother for encouraging me throughout this journey and for proofreading my thesis. And finally, I need to thank my wonderful girlfriend, Yingli Rao for her boundless love and support.

Table of Contents

List of Figures

List of Tables

Abbreviations

2D	Two-dimensional
3D	Three-dimensional
ACP-1	Aquaporin-1
AED	Anti-epileptic drug
BBB	Blood-brain barrier
CA	Contrast agent
CNR	Contrast-to-noise ratio
COX-2	Cyclooxygenase-2
CSE	Convulsive status epilepticus
CSF	Cerebrospinal fluid
DEX	Dexamethasone
EEG	Electroencephalography
EP	Ethyl pyruvate
EPI	Echo-planar imaging
ETL	Echo train length
FA	Flip angle
FC	Functional connectivity
FDR	False discovery rate
fMRI	Functional magnetic resonance imaging
FSE	Fast spin-echo
FWE	Family-wise error
GABA	γ-aminobutyric acid
HCV	Hippocampal volume
HMGB1	High mobility group box protein 1
HS	Hippocampal sclerosis
IgG	Immunoglobulin G
i.p.	Intraperitoneal

i.v.	Intravenous
ICA	Independent component analysis
ICE	Interleukin converting enzyme
ID	Injected dose
Il-1β	Interleukin-1β
ILAE	International League Against Epilepsy
Iodogen	1,3,4,6-tetrachloro-3α,6α-diphenylglucoluril
KA	Kainic acid
MFS	Mossy fibre sprouting
MPIO	Micron-sized particles of iron oxide
MRI	Magnetic resonance imaging
mTLE	Medial temporal lobe epilepsy
mTOR	Mammalian target of rapamycin
NCC	Normalised clustering coefficient
NF-κB	Nuclear factor-κB
NMDA	N-methyl-D-aspartate
NMR	Nuclear magnetic resonance
NTFs	Neurotrophic factors
PBS	Phosphate-buffered saline
PET	Positron emission tomography
PFA	Paraformaldehyde
RARE	Rapid acquisition with refocused echoes
RF	Radiofrequency
rHCV	Relative hippocampal volume
ROI	Region-of-interest
rsfMRI	Resting state functional magnetic resonance imaging
SD	Standard deviation
SEM	Standard error of the mean
SE	Status epilepticus
SNR	Signal-to-noise ratio
SPGR	Spoiled gradient-echo
SRS	Spontaneous recurrent seizures
T_1	Longitudinal magnetisation relaxation time constant

T_2	Transverse magnetisation relaxation time constant
TBI	Traumatic brain injury
TBV	Total brain volume
TE	Echo time
TE_{eff}	Effective echo time
TLE	Temporal lobe epilepsy
TNF-α	Tumour necrosis factor-α
tosyl	p-toluenesulfonyl
TR	Repetition time
VBM	Voxel-based morphometry
VCAM-1	Vascular cell adhesion molecule-1

Thesis Outline

The focus of this thesis is the development and application of novel imaging approaches for the lithium-pilocarpine rat model of epilepsy. The emphasis is on the identification of biomarkers for therapy monitoring. Chapter 1 discusses the current state of epilepsy research, the processes involved in the development of epilepsy and the need for animal models of epilepsy. Chapter 2 provides the theory behind magnetic resonance imaging and the different imaging pulse sequences that are used in this project. Chapter 3 outlines the development of experimental protocols and image analysis methods. Chapter 4 describes the development and characterisation of the iron oxide contrast agent that is used in molecular imaging studies. Chapter 5 details the application of this molecular imaging approach to the lithium-pilocarpine model of prolonged seizures. Chapter 6 is split into three parts. The first part details an attempt to use molecular imaging to monitor an anti-inflammatory therapy - dexamethasone given after status epilepticus. The second part is concerned with using imaging to assess whether or not dexamethasone is neuroprotective. The last part is concerned with a different anti-inflammatory drug - ethyl pyruvate. Chapter 7 describes the use of functional MRI to observe network alterations following status epilepticus and finally Chapter 8 summarises the conclusions that can be drawn from this work and outlines potential future work.

Publications arising from this thesis

1. **Duffy B. A.**, M. Choy, J. Riegler, J. A. Wells, D. C. Anthony, R. C. Scott & M. F. Lythgoe (2012). Imaging seizure-induced inflammation using an antibody targeted iron oxide contrast agent. *Neuroimage,* 60**,** 1149-1155.
2. **Duffy B. A.**, K. P. Chun, D. Ma, M. F. Lythgoe & R. C. Scott (2014). Dexamethasone exacerbates cerebral edema and brain injury following lithium-pilocarpine induced status epilepticus. *Neurobiology of Disease*, 63, 229-236.

Awards

Japan Society for the Promotion of Science: Summer Programme Fellow 2013

Chapter 1 Epilepsy

1.1 Classification

Epilepsy is a family of neurological disorders characterised by recurrent or the potential for recurrent epileptic seizures. Typical definitions include three elements(1): History of at least one seizure, enduring alteration of the brain that increases the likelihood of future seizures and associated neurobiologic, cognitive, psychological and social disturbances. Epileptic conditions are classified according to seizure type and cause. Seizures can be classified as either partial or generalised(2), where the former relates to epileptic activity that is localised in the brain e.g. one cerebral hemisphere, and the latter refers to seizures in which activity involves both cerebral hemispheres. Further classification of seizures includes the degree to which consciousness is impaired. The term ‘simple’ refers to the case in which there is no or little impairment and ‘complex’ refers to the situation in which consciousness is perceptibly impaired.

1.2 Temporal Lobe Epilepsy

Temporal lobe epilepsy (TLE) is the most common type of epilepsy. Mesial temporal lobe epilepsy (mTLE) involves the amygdala, hippocampus, parahippocampal gyrus, piriform cortex, entorhinal cortex, perirhinal cortex and to a lesser extent the cerebral cortex and thalamus(3). The most common structural abnormality in mTLE is hippocampal sclerosis (HS), which involves neuronal loss and gliosis of the hippocampus. It is unknown whether HS is a cause or a consequence of seizures and longitudinal imaging studies have yielded conflicting results regarding a possible causal link between seizures and progressive hippocampal atrophy(4-6). It is true that surgical resection of the amygdala and hippocampus often leads to seizure control(7), which indicates that these regions are frequently required for seizure initiation and/or propagation.

1.3 Aetiology

TLE often begins after an identifiable cerebral insult such as febrile seizures, prolonged seizures, hypoxia-ischemia or head injury. Febrile seizures are thought to

be linked to the development of temporal lobe epilepsy. These are seizures that are associated with fever in the absence of other precipitating events, such as central nervous system infection or electrolytic imbalance(8). Febrile seizures are extremely common with a prevalence between 3% and 8% in children up to 7 years of age(9). It is currently unknown whether febrile seizures cause epilepsy, however some evidence exists to suggest that prolonged seizures (status epilepticus) could initiate a cascade of events which may lead to the development of TLE. Even in cases of prolonged febrile convulsions or repeated seizures within the same day, the risk of developing spontaneous seizures may be as low as 6%(10), suggesting that a 'second hit' may be necessary to trigger epilepsy development(11).

1.4 Status Epilepticus

Status epilepticus (SE) is the most common medical neurological emergency in children and is defined as a seizure persisting for longer than 30 minutes(12). Uninterrupted convulsive status epilepticus (CSE) is thought to cause brain injury or even lead to chronic epilepsy(13). For example, patients with (nonfebrile) acute symptomatic (provoked) SE carry a higher risk of subsequent unprovoked seizures over patients who experienced brief acute symptomatic seizures(14). The risk of an unprovoked seizure is 3.3 fold higher (41%) after CSE than after a single brief seizure (13%). Although, this does not necessarily imply that CSE causes epilepsy because a prolonged seizure may be an indication of considerable brain injury already present at the time of the initial seizure. This causal relationship holds true in animal models, for instance, one episode of chemically-induced SE can cause epilepsy but terminating SE at 30 minutes using anti-convulsant drugs prevents the development of spontaneous recurrent seizures (SRS)(15). This relationship also exists in animal models of febrile seizures(16). Currently, prospective cohort studies such as the North London Convulsive Status Epilepticus in Childhood Surveillance Study (NLSTEPSS)(17) and the Consequences of Prolonged Febrile Seizures in Childhood (FEBSTAT) study(18) aim to determine the relationship between childhood status epilepticus, acute hippocampal injury and the later development of mesial temporal sclerosis, TLE and cognitive impairment.

Children with (both febrile and nonfebrile) CSE have been found to perform worse than controls on neurodevelopmental measures(19). It is not known the extent to which the seizure causes neuronal injury and the reorganisation of neuronal networks or whether the factors that predispose children to CSE also are responsible for cognitive impairment. Cognitive impairment could be considered to be the most common disability associated with epilepsy(20). In cases of TLE where seizures are not fully controlled (approximately 30% of patients(21)), cognitive decline is particularly severe(22). Anti-epileptic drugs (AEDs) that are used to control seizures are also likely to lead to cognitive and behavioural deficits(23). There is therefore a need for experimental epilepsy research directed at understanding the processes behind the development of epilepsy and its comorbidities.

1.5 Animal Models of Epilepsy

The necessity for animal models in epilepsy research cannot be disputed. Only through animal experimentation is it possible to elucidate the biological mechanisms behind seizures, epileptogenesis and cognitive dysfunction. Additionally, controlled experiments enable studies to be performed in animal models with the same aetiology without the confounding effects of anti-epileptic drugs. Experimental models have been used in the past for the discovery of new anti-epileptic drugs(24) and are now being used as an experimental platform for identifying new anti-epileptogenic drugs that could be used to reduce or prevent the development of SRS. This topic will be discussed in more detail in section 1.8.

Animal Models of chronic epilepsy (i.e. animals that exhibit unprovoked seizures), can typically be divided into those which are models of acquired epilepsy and those which are genetic epilepsies. Only models of acquired epilepsy will be discussed here. Models of acquired epilepsy can be divided into main two groups: electrically-induced or chemically-induced epilepsy. SRS can also be induced through the use of hyperthermia in immature rodents(25) or fluid percussion injury(26). However, these models have not been as widely studied, possibly because they are not as severe as the other models in that only a small subset of the affected rats go on to develop epilepsy. Arguably, these models are more akin to the human situation than the models based on chemical or electrical stimulation. Nevertheless, all of these models

can reproduce to some extent the pathophysiological alterations that are present in patients with acquired epilepsy.

In the models discussed here (with the exception of kindling), spontaneous recurrent seizures start to develop after self-sustaining status epilepticus (SSSE). There appears to be a (seizure-free) asymptomatic latency period of several weeks before the onset of epilepsy, which will be discussed further in section 1.6. The chemoconvulsant models of epilepsy are those in which chemicals are used to induce status epilepticus. Chemicals that act on excitatory glutamatergic or cholinergic receptors are either administered focally (to the brain) or systemically, which subsequently leads to the induction of SE. One of the main problems with systemic models is the high mortality rate. In order to reduce mortality, seizures are typically interrupted by using diazepam 60-120 min after the induction of SE(24). Systemic chemoconvulsant models are more variable than focal models and have the obvious disadvantage that large quantities of chemicals introduced into the blood supply have many systemic effects which may introduce confounding factors. These need to be taken into consideration in the design of experiments. A major advantage of systemic models is that they are less labour intensive than focal models. The following three sections will focus on the systemic chemoconvulsant models and will be followed by a brief consideration of the electrical models.

1.5.1 Pilocarpine

Pilocarpine is an agonist for muscarinic acetylcholine receptors and is currently one of the most widely used models of chronic epilepsy. Large doses (300-400 mg/kg of body weight) of pilocarpine induce electrographic activity in cortical and limbic regions with concomitant behavioural manifestations which include akinesia and facial automatisms and the progression to self-sustaining SE. There is known to be a strong positive correlation between age and mortality in the pilocarpine model of SE(27), which to some extent emulates the human condition(28). In both animal models and humans, the developing brain is more susceptible to seizures but much more resistant to neuronal injury(29). Practically, this means that young adult rats are most often used to study the effects of SE on brain injury. SSSE primarily causes injury to the piriform and entorhinal cortices, amygdala, CA1 and CA3 subregions of the hippocampus as well as to the hypothalamus and subregions of the thalamus(30).

1.5.2 Lithium-Pilocarpine

Pre-treatment with lithium, within 24 h prior to pilocarpine administration, significantly reduces the dosage needed to induce status epilepticus in rats by approximately ten-fold. The lithium-pilocarpine model is very similar in most aspects to the pilocarpine model. For example, there is a similar pattern of electrographic activity and neuronal damage(31). Pre-treating rats with lithium generally results in a higher proportion of animals exhibiting SE, coupled with a lower mortality rate(32). The underlying mechanisms by which lithium exerts its effects are largely unknown. Curiously, the situation is different for mice as lithium does not appear to reduce the dose of pilocarpine required to induce SE(33). Given that both chemicals also have wide-ranging peripheral effects(34), the mouse pilocarpine, rat pilocarpine and rat lithium-pilocarpine models should not be considered as one and the same.

1.5.3 Kainate

Kainic acid (KA) is an agonist for the kainate or KA subtype of glutamate receptor, which is present at its highest concentrations in the CA3 subregion of the hippocampus(35). It is widely used in animal models of SE as KA causes epileptiform activity in the hippocampus as well as a pattern of cell loss which mimics TLE. In 1987 there was an outbreak of illness in which domoic acid, which is structurally similar to KA was ingested via contaminated seafood(36). Several of these patients experienced temporal lobe seizures. Another patient developed complex partial status epilepticus after domoic acid intoxication and was seizure-free until one year later when he developed complex partial seizures accompanied by severe bilateral hippocampal atrophy(37). This event parallels the kainate model of epilepsy and therefore provides support for its use as a model of the human condition.

1.5.4 Electroconvulsant

Stimulation of the amygdala, hippocampus, entorhinal or piriform cortices using implanted electrodes can lead to self-sustaining status epilepticus. Similar to the chemoconvulsant models, seizure severity gradually increases from stage 3 to 5 on the Racine scale (section 1.5.6). Electrically induced SE leads to bilateral injury to the limbic regions, thalamus and neocortex(38).

1.5.5 Kindling

Kindling is unique in that chronic epilepsy is not caused by a single precipitating event but rather repeated application of (subthreshold) electrical stimuli to the limbic regions of the brain. These short occurrences of synchronous neuronal firing lead to a gradual increase in seizure susceptibility over time which is accompanied by progressive neuronal loss in the CA1 and CA3 subregions of the hippocampus and hilus of the dentate gyrus(39). It is currently unknown whether kindling can occur in humans as there is no direct human correlate(11).

1.5.6 Behavioural assessment of seizure severity

Without implantation of electroencephalography (EEG) electrodes, seizure severity in rodents can be gauged using behavioural scoring. The accepted method of scoring limbic seizures is the Racine scale(40), which was originally based on electrical stimulation of the amygdala. The Racine scale consists of 5 stages: (1) Mouth and facial automatisms, (2) head nodding, (3) unilateral/bilateral forelimb clonus, (4) forelimb clonus with rearing, (5) rearing and falling. Stages 1 and 2 are sometimes considered to be partial (or non-convulsant) seizures and 3-5 as generalised(41). The onset of self-sustaining status epilepticus is often defined as stage 3 on the Racine scale(42-44) as this is the point at which the seizure becomes generalised and unmistakeably manifests as forelimb clonus.

1.6 Epileptogenesis

Epileptogenesis typically refers to the process by which a normal brain becomes epileptic. As noted in section 1.2, in humans, there is an asymptomatic ‘latent period’, between brain injury and the development of epilepsy. Animal models suggest that epileptogenesis might be a continuous process and therefore the term ‘latent period’ could be misleading as seizure probability following a precipitating insult appears to be a continuous function of time rather than a step function(45). For this reason it has been argued that the term epileptogenesis is poorly defined as it could also include the possible progression of epilepsy i.e. worsening of seizure frequency(46). The possible existence of a latent period implies that slowly developing secondary

processes are responsible for epileptogenesis and also that there exists an extended therapeutic window during which anti-epileptogenic strategies can be tested(47).

1.7 Processes involved in Brain Injury and Epileptogenesis

The processes involved in epileptogenesis are currently poorly understood. Studies that have attempted to identify differences between epileptic and control subjects have identified a large variety of differences. It is not yet known which pathophysiological alterations are the important contributors in epileptogenesis. Glutamate excitotoxicity is widely accepted to be the primary underlying mechanism behind acute seizure-induced brain injury(48), yet it is not capable of explaining the slow progression of brain injury or the processes involved in epileptogenesis. The following sections will highlight the key research on the pathophysiological alterations that occur following status epilepticus.

1.7.1 Glutamate Excitotoxicity and Ischemia

Excitotoxicity is a common mechanism for neuronal injury across many pathological conditions e.g. status epilepticus, ischemia, traumatic brain injury, alcohol withdrawal etc. It occurs in situations where there is an excessive concentration of the excitatory amino acid glutamate. Glutamate acts on NMDA (N-methyl-D-aspartate) receptors, where it causes an influx of calcium ions. Excessive concentrations of Ca^{2+}, directly leads to activation of different enzymes such as protein kinase C, phospholipase A and nitric oxide synthase(49). These enzymes, if overactivated, generate a number of neurotoxic compounds and free radicals which can then rapidly lead to cell death via a positive feedback mechanism(50). Although excitotoxicity is the primary mechanism underlying seizure-induced brain injury, as SE progresses, lactic acidosis may cause the blood pressure to fall and an insufficient blood supply may result in ischemia(50, 51) i.e. a shortage in oxygen and glucose. Evidence from chemoconvulsant models indicates that both excitotoxic and ischemic mechanisms contribute to brain injury(52, 53) but these models may involve longer and more severe seizures than typical cases of SE in humans(54).

1.7.2 Neuronal Loss

Epileptogenic insults are usually associated with cell death. The extent to which this contributes to a lowering of seizure thresholds or ictogenesis (seizure generation) is not known. It has been argued that cell death is not necessary for epileptogenesis as it often does not appear to be detectable in the febrile seizures model(55). In epilepsy patients as well as animal models, hippocampal sclerosis is normally associated with the loss of CA1 and CA3 pyramidal cells, hilar mossy cells and hilar peptide-containing interneurons(56). The selective damage to the CA1 and CA3 subregions of the hippocampus reflects both the intrinsic circuitry(57) as well as the distribution of glutamate receptors(58).

Mossy cells in the dentate gyrus form a positive feedback circuit with dentate granule cells, and for this reason they are thought to be selectively vulnerable to excitotoxicity during seizures. There are three hypotheses concerning their possible role in epilepsy(59). The first of these is that loss of mossy cells leads to mossy fibre sprouting, which will be discussed in the following section. The second is the 'dormant basket cell' hypothesis which attempts to explain hyperexcitability in the hippocampus as the result of loss in mossy cells that synapse with inhibitory basket cells in the dentate gyrus(60). This particular hypothesis was generated by the need to explain the observation of decreased inhibition in light of the concomitant preservation of inhibitory gamma-aminobutyric acid (GABA) containing neurons(61). At the current time, the plausibility and experimental evidence for this hypothesis is a matter of debate(62). The third hypothesis is that surviving mossy cells undergo persistent changes that lead to hyperexcitability.

1.7.3 Progression of Brain Injury

Longitudinal MRI studies in rodents have confirmed that cell loss continues to occur during the weeks and months that follow SE(44, 63). These changes have been observed up to 2 months after the initial seizure(64). Crucially, neuronal degeneration appears to be associated with the initial brain injury and not with the ensuing seizures. These findings have not been confirmed in humans. Scott et al. observed increased hippocampal volume asymmetry in children imaged firstly between 48 h and 5 days of a prolonged febrile convulsion and who had a follow-up

scan between 4 and 8 months. This indicates a possible causal link between SE and HS in humans(65), but there is also the possibility that pre-existing asymmetry might have been obscured by the hippocampal oedema associated with the seizure.

1.7.4 Mossy Fibre sprouting

Mossy Fibre sprouting (MFS) refers to the situation in which axons of dentate granule cells (mossy fibres) grow into the inner third of the molecular layer of the dentate gyrus. MFS has been extensively studied and there is much debate about whether this phenomenon contributes to hyperexcitability through the formation of aberrant excitatory networks. Arguments against this hypothesis arise from studies that have shown that cycloheximide can be used to reduce MFS without having any effect on spontaneous seizures(66, 67).

1.7.5 Inflammation and Blood-brain Barrier Permeability

Epileptogenic insults (e.g. TBI, stroke, status epilepticus etc.) are well known to lead to microglial activation and recruitment of leukocytes. Furthermore, resected tissue from temporal lobe epilepsy patients displays elevated levels of several inflammatory markers(68-70). It is currently unknown whether these observations are merely an epiphenomenon or whether they play a role in the etiopathogenesis of seizures or epilepsy. There is emerging evidence to suggest the latter is true and sections 1.8.5-1.8.8 will discuss experimental studies that have used pharmacological modulation of inflammation in attempts to disrupt inflammatory processes following SE. The rest of this section will address the hypothesised mechanisms that link inflammation with network hyperexcitability and brain injury.

The pro-inflammatory cytokine, Interleukin-1 beta (Il-1β) is thought to enhance ictogenesis and seizure propagation. Il-1β inhibits GABA receptor function in cultured hippocampal neurons(71, 72). It also enhances NMDA receptor mediated transmission by both inhibiting outward currents(73) and by enhancing calcium influx(74). Together, both of these mechanisms will serve to increase excitability of the hippocampus. *In vivo* application of lipopolysaccharide (a toll-like receptor 4 agonist) to the cortex can result in epileptiform discharges(75), which can be blocked by pre-application of an interleukin-1 receptor antagonist. This demonstrates that Il-1β can induce ictogenesis *in vivo* and also that other inflammatory cytokines which

act on toll-like receptor 4 e.g. high mobility group box protein 1 (HMGB1), will enhance hyperexcitability via Il-1β dependent mechanisms. Seizure activity directly leads to HMGB1 release(69) as well as to the release of Il-1β(76, 77). These inflammatory cytokines will directly lead to recruitment of peripheral immune cells and increases in blood-brain barrier (BBB) permeability(78).

Enhanced blood-brain barrier (BBB) permeability has been observed in epilepsy patients that have recently undergone seizures(79) or status epilepticus(80). Van Vliet et al.(80) identified dramatic alterations in BBB permeability that present following electrically induced SE. This pivotal study revealed that seizure frequency correlates with BBB permeability and that opening of the BBB can increase seizure frequency. These data signify that BBB permeability might be a key factor in progression of temporal lobe epilepsy or epileptogenesis in rodents. The mechanisms for this are thought to occur via the astrocytic uptake of extravasated serum albumin leading to impaired potassium buffering(81). The mechanisms that are involved in epileptogenesis can further be elucidated by observing the effects of early pharmacological manipulation on later brain injury and SRS.

1.8 Therapies for Neuroprotection and the Prevention of Epileptogenesis

According to the International League Against Epilepsy (ILAE), preventing the development of epilepsy following brain trauma is one of the most relevant and urgent priorities for researchers(20). Only in the last few years, following the publication of several high profile research articles, has this been seen to be an achievable and worthwhile goal. For this reason, there have been several recent reviews on this subject(82-92). Almost all of these reviews highlight the need for biomarkers, e.g. biochemical, electrophysiological or imaging measurements that can be used to track disease progression and monitor the effect of treatments. Imaging biomarkers, most notably MRI markers have been deemed to be some of the most promising candidates because they provide exceptional spatial information that other methods lack. This section will provide an overview of therapies that have been tested for the purpose of preventing epileptogenesis or neuronal injury and will then go on to discuss potential biomarkers.

1.8.1 Neurotrophic Factors

Following cerebral insults, neurotrophic factors (NTFs) are produced in order to promote stem cell proliferation and differentiation(93). It is possible that expression of NTFs is insufficient in order to repair the neuronal damage caused by excitotoxic events. This hypothesis has been tested by using viral vectors to supplement fibroblast growth factor-2 and brain-derived neurotrophic factor. This combination therapy reduces neuronal injury as well as the frequency and severity of SRS without affecting ictogenesis(94).

1.8.2 NMDA Antagonists

Administration of NMDA antagonists following status epilepticus does not confer protection against the development of epilepsy but does significantly reduce the degree of neuronal injury in the kainate model(95), presumably due to the amelioration of excitotoxic effects (section 1.7.1). NMDA antagonists have been found to have adverse effects in clinical trials for patients with acute stroke(96-98), indicating that these drugs will not be tested in clinic as a therapy for preventing SE induced injury.

1.8.3 Anti-Epileptic Drugs

Anti-Epileptic drugs have not proven to be particularly efficacious for the prevention of epileptogenesis in preclinical studies. Evidence from the clinic also suggests that AEDs do not have any significant anti-epileptogenic effect(99). Levetiracetam has been suspected to have anti-epileptogenic properties. Interestingly, it acts in a mechanism distinct from other AEDs as it binds to synaptic vesicle protein SV2A(100). In the pilocarpine model, 21 day treatment with levetiracetam had a dose-dependent effect on hippocampal hyperexcitability in the dentate gyrus as measured by population spike amplitude(101). This conflicts with a previous study that found no significant effect in seizure frequency in a kindling model(102). Carisbamate is an AED that has not yet been approved by the United States Food and Drug Administration. Compared to diazepam, it might have anti-epileptogenic properties in the lithium-pilocarpine model(103), but the degree to which this effect was due to the alleviation of SE severity is unknown.

1.8.4 Rapamycin

The mammalian target of rapamycin (mTOR) is a serine/threonine protein kinase with a wide range of functions including synaptic plasticity(104). Administration of rapamycin following kainic acid induced SE, dramatically reduces SRS(105). In the rat pilocarpine model, rapamycin treatment in the chronic epilepsy phase confers suppression of seizure activity, which begins to return on cessation of treatment(106), suggesting that rapamycin may suppress ictogenesis. Although its mechanism of action is largely unknown, administration following SE reduces the biphasic activation of the mTOR pathway(105) and has been found to reduce MFS in 2 different models of epilepsy(105, 107). Interestingly, it has also been associated with a reduction in BBB permeability compared to controls(108), therefore it is possible that its anti-epileptogenic effects might occur via this mechanism. Rapamycin has no effect on epileptogenesis in the mouse pilocarpine model(109).

1.8.5 Anti-inflammatory therapies

Many studies have shown various anti-inflammatory drugs to be neuroprotective or anti-epileptogenic following status epilepticus. For this reason and because there are many already clinically approved compounds, they are the most promising candidates for translation into clinic. The following sections will review the key research on this topic.

1.8.6 Non-steroidal anti-inflammatory drugs

Non-steroidal anti-inflammatory drugs have wide-ranging effects depending on the animal model used and schedule of administration after SE. Following electrically induced SE(110), Holtman et al. observed no effect of SC58236, a selective cyclooxygenase-2 (COX-2) inhibitor, on cell death or microglial activation in the hippocampus. In contrast to this study, Parecoxib, another selective COX-2 inhibitor administered for 18 days following lithium-pilocarpine induced SE was shown to be neuroprotective but not anti-epileptogenic(111). Celecoxib reduces neuronal injury and microglia activation when administered one day after lithium-pilocarpine induced status epilepticus(112). Conditional ablation of COX-2 in forebrain neurons reduces hippocampal injury in the CA1 subregion of the hippocampus at 4 days post

pilocarpine induced status epilepticus, however there is some evidence to suggest that COX-2 is neuroprotective at 24 h following the insult(113).

1.8.7 Corticosteroids

Corticosteroids such as dexamethasone (DEX) act on the glucocorticoid receptor and are highly effective in reducing BBB permeability. DEX does not readily cross the BBB(114) and the mechanisms by which these corticosteroids are BBB protective are numerous. Three known mechanisms involve the induction of annexin I, induction of mitogen-activated protein kinase phosphatase I and the blocking of nuclear factor kappa B (NF-κB)(115). The glucocorticoid receptor is expressed ubiquitously and *in vitro* studies suggest that dexamethasone exerts an effect directly on endothelial cells(116). DEX reduces infarct volume when administered following cerebral ischemia in rats(117), supporting the view that DEX may also alleviate brain injury following status epilepticus. Two recent studies have found that dexamethasone is neuroprotective when administered prior to pilocarpine or lithium-pilocarpine induced status epilepticus(118, 119). The mechanisms of this are thought to occur via the alleviation of vasogenic oedema and subsequently less severe status epilepticus. However, the clinical relevance of these studies is debatable as administration of dexamethasone preceded the insult.

1.8.8 Other Anti-Inflammatory Therapies

Interleukin-1 beta is an early pro-inflammatory cytokine that is released from astrocytes following brain injury and which is known to be a key mediator of BBB permeability(120). VX-765 is a drug that inhibits Interleukin Converting Enzyme (ICE) and hence IL-1β production. VX-765 interrupts the development of kindling in rats, whilst having no effect on seizures in fully kindled rats(121). Combined VX-765 and interleukin-1 receptor antagonists given shortly after electrically induced SE confers significant neuroprotection across most affected brain regions(122). Interestingly, the effect on neuronal injury is much more limited in the lithium-pilocarpine model and the treatment had no effect on SRS in either model. In the mouse pilocarpine model, Fabene et al. showed that blocking leukocyte-endothelial interactions following SE (via administration of α4 integrin specific antibodies), reduces the occurrence of SRS(123). This finding was also associated with a

reduction in BBB permeability in the acute phase after SE. The same study found elevated numbers of leukocytes in cortical tissue from epilepsy patients compared to controls highlighting a possible drug target in the human condition.

1.9 Biomarkers of Epileptogenesis and Neuronal Injury

The term biomarker can be defined as: 'a laboratory measurement that reflects the activity of a disease process(124).' Useful biomarkers of epileptogenesis could include: measurements that enable a definitive prediction of epilepsy development and also those that enable the assessment of anti-epileptogenic therapies(125). Animal models will be crucial for the identification of new biomarkers. Roch et al. used the lithium-pilocarpine model in immature rats to test whether T_2 weighted MRI could predict the development of SRS(126). They found that early (24 h after SE) T_2 abnormalities in the piriform cortex predicted the development of epilepsy. Using the adult rat lithium-pilocarpine model, Choy et al. used principal component analysis to show that a combination of T_2, cerebral blood flow and T_1 was predictive of neuronal injury(44). Another imaging study in the pilocarpine mouse model found that much later (7 days after SE) alterations in diffusion MRI images in the hippocampus predicted interictal (between seizure) spike frequency in the chronic epilepsy phase(63). Finally, a study based on implanted electrodes in the dentate gyrus found that the time between SE and high-frequency oscillations on EEG predicted the duration of the latent period between SE and SRS in the focal kainate model(127).

1.10 Summary

This chapter has highlighted the need and interest for therapies that can prevent brain injury and epileptogenesis following cerebral insults. Several problems persist in this area, for example most outcomes appear to depend on the animal model used and the time course of drug administration. Another issue is the current need to identify biomarkers for epileptogenesis and therapy monitoring. The following chapters will aim to demonstrate that *in vivo* magnetic resonance imaging is a powerful tool that may aid in our understanding of the processes that follow status epilepticus, and that it can provide a platform for testing new and existing therapies.

Chapter 2 Magnetic Resonance Imaging

In 1922 Otto Stern and Walther Gerlach demonstrated, in what is now known as the Stern-Gerlach experiment, that atoms possess quantised angular momentum. Their experiment involved passing silver atoms from a hot oven through an inhomogeneous magnetic field. Classical physics would predict that if these silver atoms possessed a distribution of angular momentum, then they would be deflected in this inhomogeneous field to produce a distribution in space. What they found was instead of a distribution in space, the atoms were deflected to either one of two paths. This illustrates two important points that are necessary for an explanation of nuclear magnetic resonance or MRI. First, a magnetic moment with intrinsic angular momentum (such as the nucleus of an atom) precesses in a magnetic field, which is a classical phenomenon. Second, this experiment illustrated the quantum mechanical phenomenon of quantisation of angular momentum. This means that the angular momentum can only have certain values. Based on quantum mechanics, the angular momentum is only allowed to take on $(2I+1)$ possible values, where I is the nuclear spin quantum number. For protons, which are the source of signal in MRI, $I=1/2$, meaning that there are only 2 allowed values for angular momentum. The component of the angular momentum projected along the z axis (direction of the field) is given by m_I, can therefore only take on 2 values, $m_I=\pm 1/2$ ('parallel' or 'anti-parallel' to the magnetic field). The energy (E) of these states can be found from the Schrödinger equation:

$$E = -m_I B \gamma \hbar \qquad \mathbf{1}$$

where γ is the gyromagnetic ratio (the ratio of the magnetic moment to the intrinsic angular momentum), $\hbar$ is Planck's constant divided by 2π and $\boldsymbol{B}$ is the applied magnetic field. The difference in energy (ΔE) between the two states ($m_I=\pm 1/2$) depends on the applied field $\boldsymbol{B}$ and can easily be found from equation **1** to be equal to:

$$\Delta E = \hbar\omega = -\boldsymbol{B}\gamma\hbar \qquad \mathbf{2}$$

ΔE is the energy of electromagnetic radiation needed to excite a proton from the $m_I=-1/2$ state to the $m_I=+1/2$ state. Classically, it is also the frequency (ω) at which the

magnetic moment ($\boldsymbol{u_I}$) precesses around the magnetic field. According to classical physics, an external magnetic field exerts a torque ($\boldsymbol{\tau}$) on a magnetic moment which is equal to(128):

$$\boldsymbol{\tau} = \hbar \frac{d\boldsymbol{L}}{dt} = \boldsymbol{u_I} \times \boldsymbol{B} \qquad \mathbf{3}$$

where $\boldsymbol{L}$ is the angular momentum. As $\boldsymbol{u_I} = \boldsymbol{L}\gamma\hbar$, the change in the magnetic moment over time is given by(128):

$$\frac{d\boldsymbol{u_I}}{dt} = \boldsymbol{u_I} \times \gamma \boldsymbol{B} \qquad \mathbf{4}$$

and from equation **4**, it can be deduced that the change in magnetic moment over time is perpendicular to the plane defined by $\boldsymbol{B}$ and $\boldsymbol{u_I}$, hence there is a precession of $\boldsymbol{u_I}$ around $\boldsymbol{B}$. As already noted, the frequency of precession, or Larmor frequency, is also equal to the quantum mechanical transition energy ΔE from equation **2**. The ratio of the number of nuclei in each energy state (N_{m_I}) can be estimated from the Boltzmann factor:

$$\frac{N_{m_{I=-1/2}}}{N_{m_{I=+1/2}}} = \exp\left(-\frac{\omega\hbar}{kT}\right) \qquad \mathbf{5}$$

where k is Boltzmann's constant. This difference in populations can be used to explain the net magnetic moment in the z direction of an ensemble of nuclei.

If a radiofrequency (RF) pulse is applied perpendicular to the magnetic field at the frequency ω, this causes nuclei to transition between parallel and anti-parallel states which alters the populations of the spin states. This can be visualised through the use of a coordinate system rotating around the z axis at the Larmor frequency.

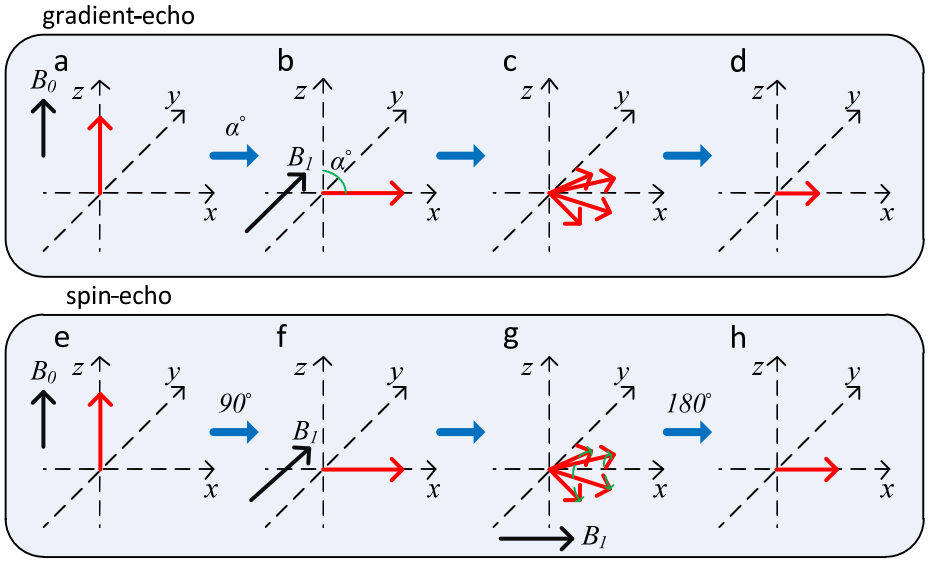

Figure 1: Magnetisation in a rotating coordinate system in the spin-echo and gradient-echo pulse sequences. (a)-(d): gradient echo sequence. (e)-(h): spin-echo sequence. (a) Initial magnetisation in a magnetic field aligned with the *z* axis. (b) Magnetisation following an RF pulse (***B₁***) of flip angle α applied parallel to the *y* axis. (c) Application of a dephasing gradient causes spins to precess out of phase. (d) Dephased spins are then focussed to form an echo aligned with the *x* axis using a readout gradient of opposite polarity. (e) Initial magnetisation. (f) Following application of a 90º RF pulse (***B₁***). (g) After prephasing, a 180º pulse is applied, which causes spins to rotate 180º around the *x* axis. (h) Focussing is achieved using a readout gradient with the same polarity as the prephasing pulse.

At equilibrium, the net magnetisation is aligned with the main field (***B₀***) (Figure 1a). Following the application of a magnetic field (***B₁***) oscillating at the Larmor frequency, the net magnetisation is rotated towards the *xy* plane by an angle α (Figure 1b). This angle is known as the flip angle (FA) and depends on the strength and duration of the applied field ***B₁***. Following application of the RF pulse, the magnetic moments of a small proportion of the nuclei in the system begin to precess around the ***B₀*** field in-phase, which is what leads to the presence of net magnetisation in the *xy* plane.

The decay back to the equilibrium state is what is usually measured in the nuclear magnetic resonance (NMR) experiment and the measured signal is called the free-induction decay. The decay process of the *z* component of magnetisation (M_z) is known as spin-lattice relaxation. M_z decays as described by equation **6** and the decay constant is denoted by T_1 (Figure 2a). In the *xy* plane, it is known as spin-spin

relaxation and the decay constant is T_2 or T_2* (Figure 2b). T_2 is used if an RF pulse is used for refocusing of the decaying magnetisation (as is the case in the spin-echo experiment discussed in the next section), and T_2* is used if this is not the case. The decay of magnetisation in the *xy* plane (M_{xy}) is described by equation **7**. We have not yet considered how images can be formed in MRI and so this will be the topic of the next section.

$$M_z(t) = M_z(0)(1 - \exp(-t/T_1)) \quad \textbf{6}$$

$$M_{xy}(t) = M_{xy}(0)\exp(-t/T_2) \quad \textbf{7}$$

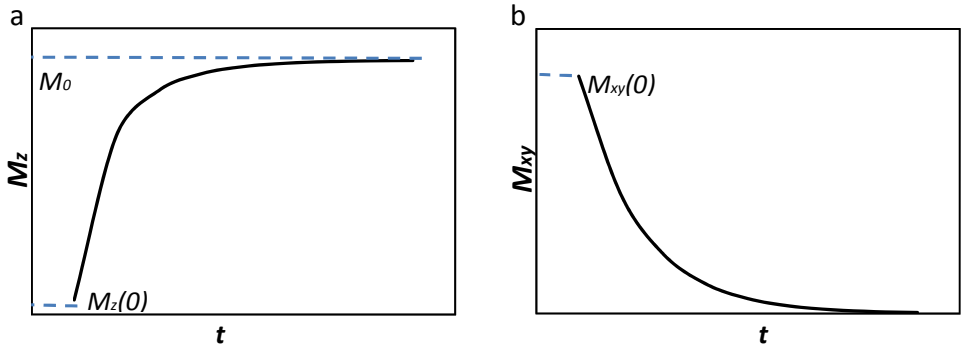

Figure 2: Exponential decay of net magnetisation back to equilibrium following application of an RF pulse. (a) Longitudinal (*z)* component of magnetisation. (b) Transverse magnetisation (magnetisation projected onto the *xy* plane).

2.1 Basic Imaging Sequences

Spatial information is encoded in the MRI signal through the use of temporary magnetic field gradients and RF pulses. Firstly, (in a two-dimensional (2D) multi-slice sequence) the signal from one slice of the imaging volume can be localised by selective excitation of this region. This is achieved by simultaneously applying a temporary magnetic field (slice-select gradient-Gss) and a RF excitation pulse with the correct frequency and bandwidth (Figure 3a,b). Within this plane, spatial information is encoded in one direction using a temporary gradient applied during the acquisition (readout gradient-Gro) in a technique known as frequency encoding.

The localisation in the final direction is achieved using a different temporary gradient (phase-encoding gradient-Gpe) orthogonal to the frequency encoding gradient. This leads to a different phase-shifted signal at each location and hence this is known as phase-encoding. The strength of the phase encoding gradient is systematically altered in order that each location experiences a range of phase shifts. In the plane defined by the frequency and phase-encoding axes, the acquired signal is organised in frequency space (*k*-space), with the frequency and phase-encoding directions arranged orthogonally. *k*-space can be Fourier transformed to generate the MRI image.

Two most fundamental imaging pulse sequences in MRI are the gradient-echo sequence and the spin-echo sequence. In the gradient-echo sequence, firstly an RF pulse is applied with a flip angle α (Figure 3a) and the subsequent acquisition is performed at a time known as the echo time (TE) after the initial excitation pulse. Prior to the readout at time TE, a dephasing (or prephasing) gradient is applied. This has the effect of dispersing the spins (Figure 1c). Applying a readout gradient with reversed polarity enables the creation of a measureable echo at time=TE (Figure 1d).

The spin-echo sequence consists of excitation with a 90º excitation pulse, followed by application of a prephasing readout gradient (Figure 3b). A 180º pulse is then applied which has the effect of rotating the spins 180º about the *x* axis (Figure 1g). This 180º pulse has the effect of reversing phase accumulation due to off resonance effects, e.g. slight variations in the static B_0 magnetic field. Finally, an echo is generated by applying a readout gradient with the same polarity (Figure 1h).

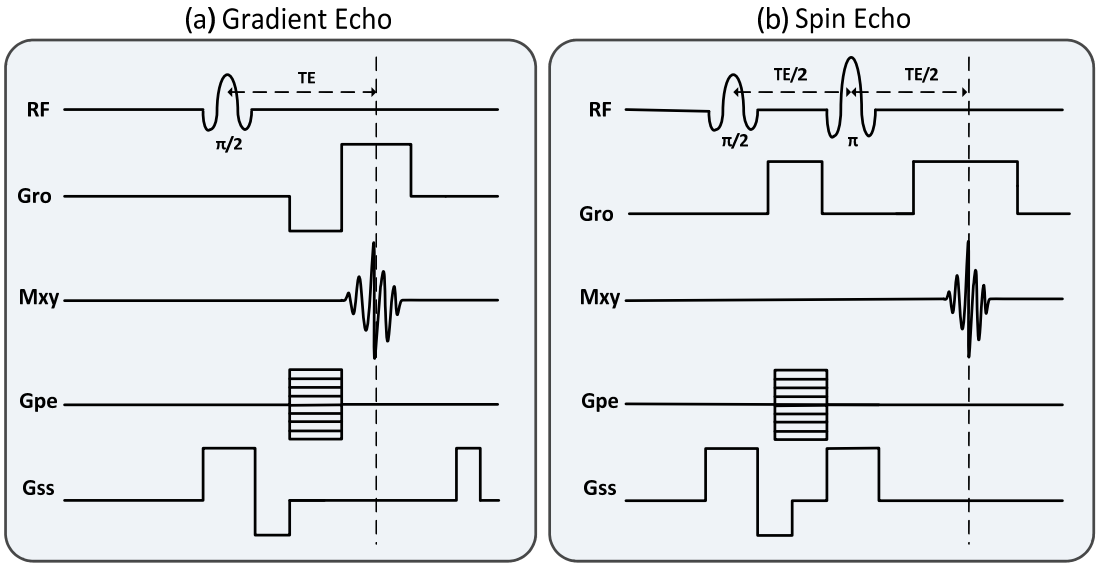

Figure 3: Basic MRI pulse sequences. (a) Gradient echo. (b) Spin echo. RF=radio frequency, Gro=readout gradient, Mxy=transverse magnetisation, Gpe=phase encoding gradient, Gss =slice select gradient.

2.2 T_1 and T_2 Weighted Imaging

The signal intensity (S) in a spin-echo experiment is given by:

$$S = k\rho(1 - \exp(-TR/T_1))\exp(-TE/T_2) \qquad \mathbf{8}$$

where k is a hardware dependent parameter and ρ is the spin density. If the TR is long (compared to T_1) and the TE is long (compared to T_2), then S depends strongly on the T_2 of the tissue and the sequence is then said to be 'T_2 weighted'. If the TR is short and TE is short, then S is more strongly dependent on the T_1 of the tissue. Endogenous tissue contrast in MRI is derived from inherent differences in the decay constants T_1, T_2 and T_2* for different tissues. This illustrates how the pulse sequence parameters can be tuned to afford optimum contrast between different tissues. The signal intensity of a gradient-echo experiment will be discussed in the following chapter. More specialised pulse sequences can generate contrast that is sensitive to water diffusion, magnetisation transfer (between protons in macromolecules and free water) or tissue perfusion.

2.3 T_2 Relaxometry

The measurement of the transverse magnetisation relaxation time constant (T_2) provides a quantitative and more objective measure than T_2 weighted imaging. Reasonable estimates of T_2 can be found using multi-echo spin-echo sequences at long repetition times (Figure 4). Multi-echo sequences involve using multiple refocussing pulses to sample the transverse magnetisation at different points along the decay curve (Figure 2b, equation **7**) and then fitting a monoexponential decay function to the data.

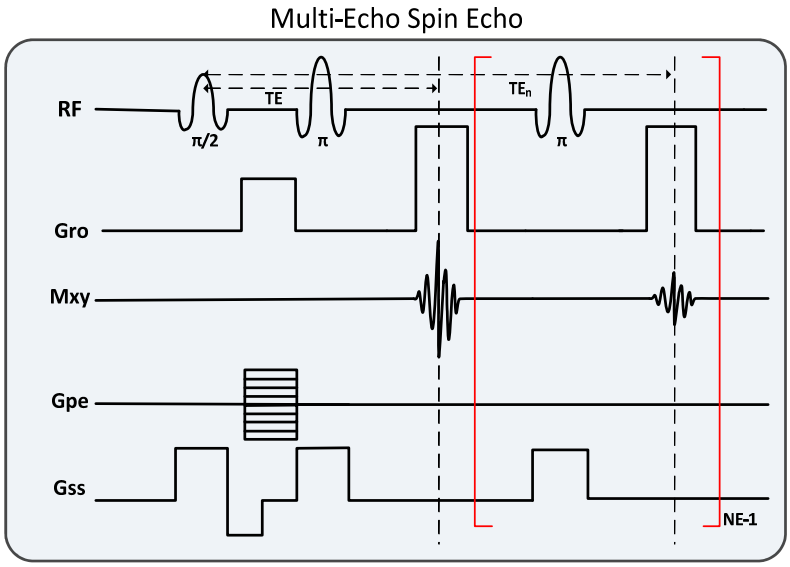

Figure 4: Multi-echo spin-echo pulse sequence for quantitative T_2 measurements. NE = number of echoes, TE_n = echo time of the nth echo.

2.4 Fast Spin-Echo

Standard spin-echo sequences have generally been superseded by more time-efficient sequences. In experimental studies, fast spin-echo (FSE) sequences, (otherwise known as rapid acquisition with refocused echoes (RARE)) are much more frequently used. This sequence is very similar to the multi-echo sequence shown in Figure 4, the only difference being that in multi-echo sequences, the same line of *k*-space is acquired, whereas in FSE, subsequent echoes are phase encoded in order to fill *k*-space (Figure 5). This leads to an improvement in acquisition time. The improvement factor is equal to the number of acquired echoes, otherwise known as the echo train length (ETL). The effective echo time (TE_{eff}) is the time after the

excitation pulse at which the centre of *k*-space (which contains the most signal) is traversed.

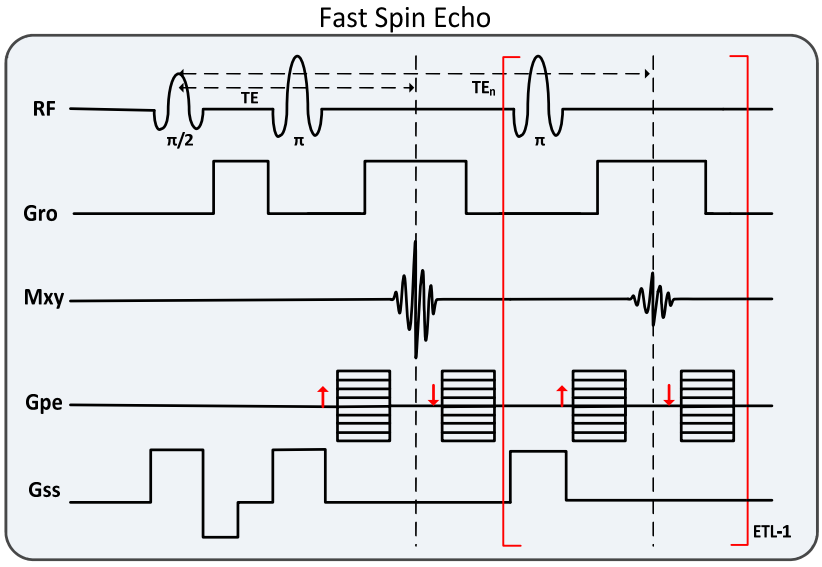

Figure 5: Fast spin-echo pulse sequence. ETL = echo train length, TE_n = echo time of the n^{th} echo.

2.5 Echo-Planar Imaging

Ultrafast MRI imaging can be achieved using echo-planar imaging (EPI). In single-shot EPI, an entire stack of images is acquired within a single TR. This sequence is typically used in functional MRI for observing brain activity as it affords time resolution that is on the order of seconds, which is fast enough to observe changes in blood flow that are associated with neuronal activity (section 7.3). In the EPI sequence (Figure 6), transverse magnetisation is continually rephased by the readout gradient and the phase-encoding gradient is applied prior to each echo. In single-shot EPI, this means the entirety of *k*-space can be traversed within one excitation.

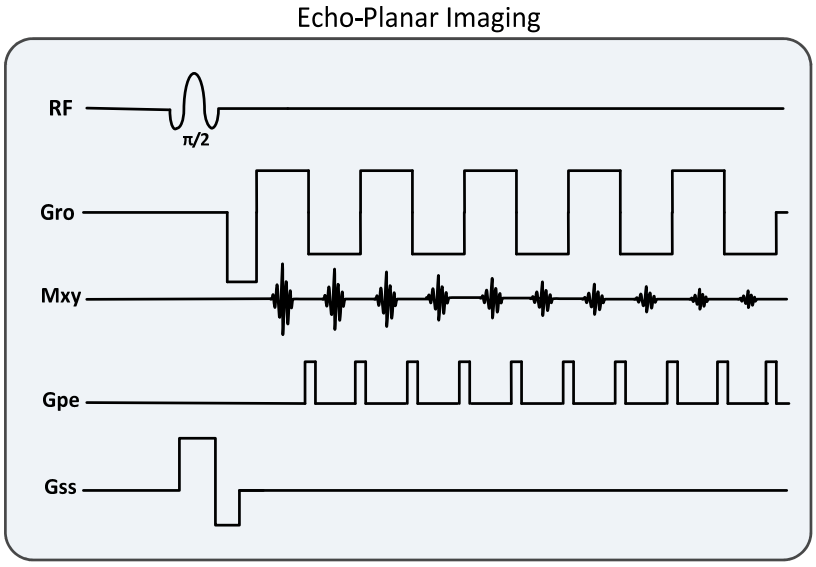

Figure 6: Gradient-echo echo-planar imaging pulse sequence.

2.6 2D *vs.* 3D sequences

In 2D multi-slice pulse sequences, data from several slices are acquired during one TR. This is achieved by exciting one slice at a time using a slice selective gradient and a shaped RF pulse. In three-dimensional (3D) sequences, an entire set of slices (a slab) is excited simultaneously. Position is then encoded in the slice direction by introducing another phase encoding direction. 3D acquisitions are advantageous in that they are able to acquire much thinner slices than is possible with multi-slice sequences. 3D acquisitions can also be more efficient in terms of signal-to-noise ratio (SNR) per unit time(129), however the total acquisition time tends to be much longer. For 3D pulse sequences with rectilinear sampling, the total acquisition time (T_{tot3D}) is given by equation **9**:

$$T_{tot3D} = NEX \times N_{pe} \times N_{pe2} \times TR \qquad \mathbf{9}$$

where N_{pe} is the number of phase encoding steps, N_{pe2} is the number of phase encoding steps in the second phase encoding direction and NEX is the number of excitations (number of averages). The total acquisition time for multi-slice sequences (T_{tot2D}) is given by:

$$T_{tot2D} = NEX \times N_{pe} \times TR \qquad \mathbf{10}$$

This means that in general, the TR needs to be shorter in 3D sequences compared with multi-slice sequences in order for the acquisition time to be of a practical length.

2.7 Summary

This chapter has introduced many basic concepts in MRI, such as imaging pulse sequences and sequence parameters that will be needed for a comprehensive understanding of the work presented in the subsequent chapters.

Chapter 3 Development of Experimental Protocols and Image Analysis Methods

The aim of this project is to develop MRI imaging methods that can be used to non-invasively monitor the effects of status epilepticus. This thesis focusses on 4 techniques: molecular imaging using iron oxide particles, quantitative measurements of T_2, volumetric MRI and functional MRI. The motive for using iron oxide for molecular imaging stems from several recent publications demonstrating its enormous potential for monitoring expression of inflammatory markers *in vivo*. Further discussion on this topic is included in the next chapter. The reasons for using T_2 relaxometry and volumetric imaging is that these are generally accepted measures of oedema and hippocampal sclerosis(130).

The first part of this chapter will focus on the design of experimental protocols, starting with the development of a protocol for the lithium-pilocarpine model of epilepsy. Following from this, the use of iron oxide contrast agents will be discussed. The final topic of the chapter will be the design of imaging protocols and image analysis methods.

In all of the work presented in this chapter as well as Chapters 4, 5 and 6 (part I and II), an Agilent Technologies 9.4T MRI scanner was used, which is located at the Centre for Advanced Biomedical Imaging at UCL. In Chapter 6 part III and Chapter 7, a 7T Bruker PharmaScan system was used, which is located at the Institute of Development, Aging and Cancer at Tohoku University. Unless otherwise stated, all chemicals were obtained from Sigma Aldrich, UK.

3.1 Animal Model of Epilepsy

In this project, I have opted to use the rat lithium-pilocarpine model to study the effects of status epilepticus on the brain. The reasons for this are firstly because the lithium-pilocarpine model is one of the most studied models of status epilepticus and secondly because previous studies in the department have used this model and therefore there is available expertise. The lithium-pilocarpine model (section 1.5.2) and the kainate (section 1.5.3) model are similar in many respects. Both have a mortality rate of around 20-40% and result in chronic epilepsy after a period of

weeks or months(131). It should be noted that the chemoconvulsant models may not be the most appropriate models of epileptogenesis in humans. Models in which only small subgroups of rodents develop epilepsy are much more akin to the human condition, but are more impractical for discovering biomarkers for epilepsy. Preliminary experiments using the lithium-pilocarpine model were conducted using adult male Sprague-Dawley rats (weighing between 170-200 g, supplied by Charles River UK Ltd, Margate UK) and the protocol outlined below:

- Intraperitoneal administration of lithium chloride (3 mEq/kg), approximately 12 h prior to pilocarpine.
- Intraperitoneal injection of methylscopolamine nitrate (5 mg/kg) 20 min prior to pilocarpine. Methylscopolamine does not cross the BBB and is used to reduce the peripheral effects of pilocarpine.
- Intraperitoneal injection of pilocarpine hydrochloride (30 mg/kg).
- Behavioural assessment of seizure severity using the Racine scale (section 1.5.6).
- Intraperitoneal injection of diazepam (10 mg/kg, Hameln Pharmaceuticals, Gloucester) after 90 min of SE to terminate the seizure.

Using the standard protocol outlined above, it was found that only 2 of 3 rats underwent status epilepticus. Chaudhary et al. reported that shortening the time between lithium and pilocarpine administration has the effect of increasing the number of rats that undergo SE(132). By adopting a new modified protocol in which lithium chloride was administered 2 h prior to pilocarpine, it was found that 12 out of 12 (100%) of rats progressed to SE. 1 animal in this experiment died during SE, therefore the mortality rate (8%) in this pilot study was low compared to the typical rates reported in the literature(31).

This section has focussed on the development of a protocol for the lithium-pilocarpine model. The next section will focus on how iron oxide can be used as a contrast agent for MRI and the following 2 sections will address imaging protocols that will be used to investigate this animal model.

3.2 Superparamagnetic Iron Oxide Nanoparticles as MRI Contrast Agents

Iron oxide is normally a mixture of magnetite (Fe_3O_4) and maghemite (Fe_2O_3). These compounds are usually ferrimagnetic meaning that if placed within a magnetic field they become magnetised into permanent magnets and exhibit a net magnetisation below what is known as the Curie temperature. Above this temperature, these materials become paramagnetic which refers to the situation where the magnetisation is a linear function of the applied magnetic field and removed from the field, all residual magnetisation is lost. Iron oxide particles of a single magnetic domain, existing below a certain diameter (normally several hundred nanometres) act as paramagnets. They are said to exhibit 'superparamagnetism' as they behave as paramagnets with a large magnetic moment.

Compounds which are ferrimagnetic will be drawn together due to the attractive force between two magnetic dipoles, leading to particle aggregation. Superparamagnetism is an extremely useful property for biomedical applications, the reason being that outside of a magnetic field, superparamagnetic particles retain no net magnetisation, therefore magnetic interactions are not a significant driving force for the formation of aggregates. However, when placed within a field, particles exhibit a large magnetic moment which is useful for MRI applications as they cause a magnetic field distortion which is detectable using MRI. Furthermore, iron oxide is non-toxic and biodegradable, rendering it safe for biomedical application. The magnetic field offset (*f*) surrounding a dipole depends on the angle to the main field and the radial distance to the dipole (*r*) (equation **11**)(133):

$$f \propto \frac{\gamma}{4\pi r^3}(3\cos^2\varphi - 1) \qquad \textbf{11}$$

where γ is the gyromagnetic ratio and φ is the angle between the position vector and the external magnetic field. Iron oxide particles therefore cause alterations in the applied magnetic field which falls off with the cube of the distance from the particle.

3.3 Imaging of Iron Oxide Particles

Magnetic field distortions caused by magnetic nanoparticles can be visualised on MRI images as local variations in the magnetic field leads to faster dephasing of

magnetisation. Gradient-echo is one of the most sensitive pulse sequences for iron oxide detection as it is more sensitive to local field distortions than spin-echo sequences with refocusing RF pulses (section 2.1).

The signal intensity in a gradient-echo experiment is given by:

$$I \propto M_0\sqrt{NEX}e^{-\frac{TE}{T2*}}(1-e^{-\frac{TR}{T_1}})\sin(\alpha)/1-e^{-TR/T_1}\cos(\alpha) \qquad \textbf{12}$$

where M_0 is the initial transverse magnetisation. From equation **12** it can be shown that the flip angle (α) which maximises the signal intensity at a given TR and T_1 is given by the Ernst angle (α_E) (Figure 7):

$$\alpha_E = \cos^{-1}(e^{(-TR/T_1)}) \qquad \textbf{13}$$

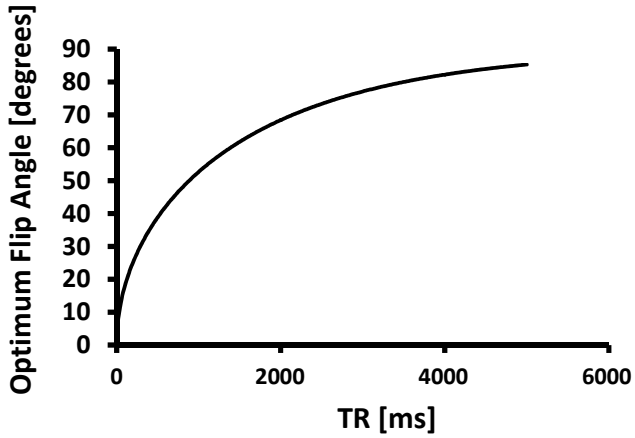

Figure 7: Repetition time *vs.* optimum flip angle (Ernst angle) for spoiled gradient-echo imaging. T_1 = 1 s

For the detection of iron oxide, we wish to maximise the contrast between two regions rather than the overall signal intensity. Iron oxide causes a decrease in T_2* and T_1, but for larger particles e.g. micron-sized particles, T_2* effects dominate and therefore T_1 effects can generally be ignored. The contrast-to-noise ratio (CNR) can be written as the signal difference between two regions divided by their mean noise. Let these two regions be denoted as A and B, where region A contains the contrast agent (CA) and region B which does not(134). The CNR is then equal to:

$$CNR = \sqrt{NEX}\frac{k}{N}\sin(\alpha)\left[\frac{\left(1-e^{-\frac{TR}{T_{1B}}}\right)}{1-e^{-\frac{TR}{T_{1B}}}\cos(\alpha)}e^{-\frac{TE}{T^*_{2B}}} - \frac{\left(1-e^{-\frac{TR}{T_{1A}}}\right)}{1-e^{-\frac{TR}{T_{1A}}}\cos(\alpha)}e^{-\frac{TE}{T^*_{2A}}}\right] \quad \textbf{14}$$

where *k* is the proton density and *N* is the mean image noise. If the T_1 in both regions is assumed to be the same, the T_1 terms can be factored outside the brackets. The term outside the brackets is equal to the SNR and can be maximised using the Ernst angle (equation **13**). The term inside the brackets is the difference between 2 exponential decay functions and depends on the TE of the sequence. Based on this reasoning, the CNR increases with TE until it reaches a maximum and then tails off.

The above model does not provide a satisfactory model of any real *in vivo* situation, in which there exists a small number of iron oxide particles unequally distributed within a voxel. Moreover, particles which are close enough to each other in proximity will tend to form aggregates further highlighting the difficulties involved with estimating iron concentrations. Nevertheless, work reported in the literature(135) suggests that using iron oxide particles as MRI contrast agents may be extremely sensitive as a molecular imaging approach. The next chapter will attempt to demonstrate this sensitivity *in vivo* with a comparison to nuclear imaging whilst the remainder of this chapter will focus on the more routinely performed imaging techniques, relaxometry and volumetric imaging.

3.4 Relaxometry Protocol and Data Analysis

T_2 weighted imaging (section 2.1) is used extensively in clinic for detection of both oedema and hippocampal sclerosis. Acute increases in T_2 following cerebral insults such as hypoxia-ischemia or status epilepticus are thought to indicate cytotoxic oedema or vasogenic oedema(136). Cytotoxic oedema in the brain refers to the swelling of neurons and astrocytes due to water diffusion from the extra-cellular compartment to within cells. It is generally considered to be caused by energy failure and the failure of the sodium-potassium pump, which in turn can be caused by glutamate excitotoxicity. Cytotoxic oedema is responsible for early T_2 increases

following excitotoxic insults, whereas later (between 12-24 h) increases are thought to be primarily caused by vasogenic oedema(137-139). Vasogenic oedema describes the process by which the water content of parenchymal tissue increases due to an impaired BBB. T_2 changes have been shown to correlate reasonably well with tissue water content 24 h following hypoxic-ischemic insults, which demonstrates that T_2 is a reliable marker of vasogenic oedema(139). T_2 lengthening in the case of oedema is thought to be caused by a higher ratio of 'free' to 'bound' water(140). Free water is known to have a longer T_2 than bound or structured water. Reduced magnetisation exchange between the free and bound water protons is also thought to play a role(141). However, the fluid that leaks from blood vessels in the case of vasogenic oedema is protein rich, which further complicates the picture(142).

T_2 relaxometry refers to the situation where T_2 is estimated by acquiring images at a range of echo times. Relaxometry can be more sensitive(143) and is likely to be more comparable between subjects than conventional T_2 weighted imaging as signal intensity can vary between imaging sessions due to a variety of factors. T_2 relaxometry conducted on a voxel-wise basis is called T_2 mapping. As noted in section 2.3, this can be carried out within a realistic acquisition time by using a multi-echo spin-echo sequence.

In this project, the default multi-echo spin-echo sequence on the Agilent MRI scanner was used. Stimulated echoes are often a problem in sequences that involve refocusing RF pulses. If the 180º refocusing pulse is non-ideal, this tips some of the magnetisation into the *z* direction which can then create a stimulated echo using another non-ideal pulse. The result of this is that the first echo (which does not contain a stimulated echo component) has a lower signal intensity than the second echo which does. The remaining echoes display an approximate monoexponential decay with an artificially long T_2(144). This did not appear to be a significant problem in the pilot data (Figure 8) therefore no further optimisation of the sequence was carried out. In brain regions where there was low SNR, the signal decayed to below the noise level at the later echo times, causing a deviation from monoexponential decay (Figure 8).

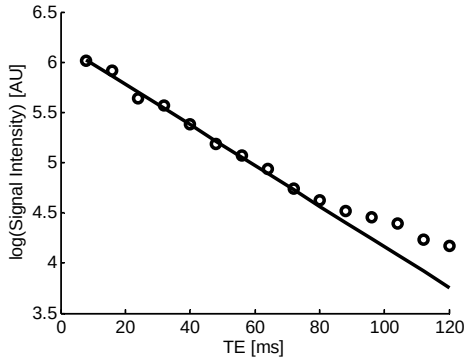

Figure 8: Example of non-monoexponential decay of signal intensity at later echo times. Echo time vs. log of the mean signal intensity from a region located in the striatum. Solid line shows a linear least-squares fit to the first 7 data points.

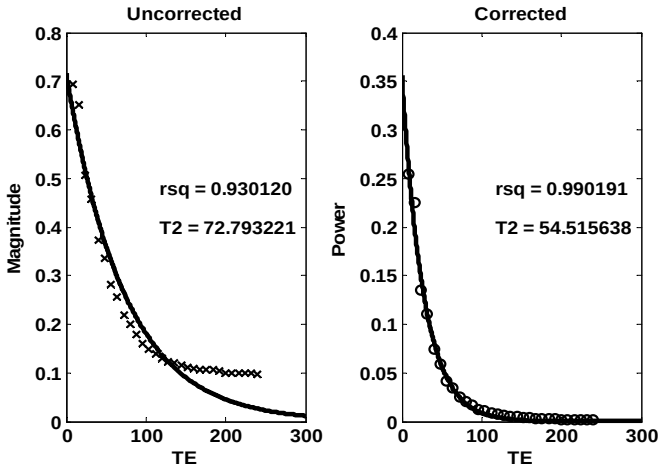

Figure 9: Use of power images for noise correction in T_2 Relaxometry.

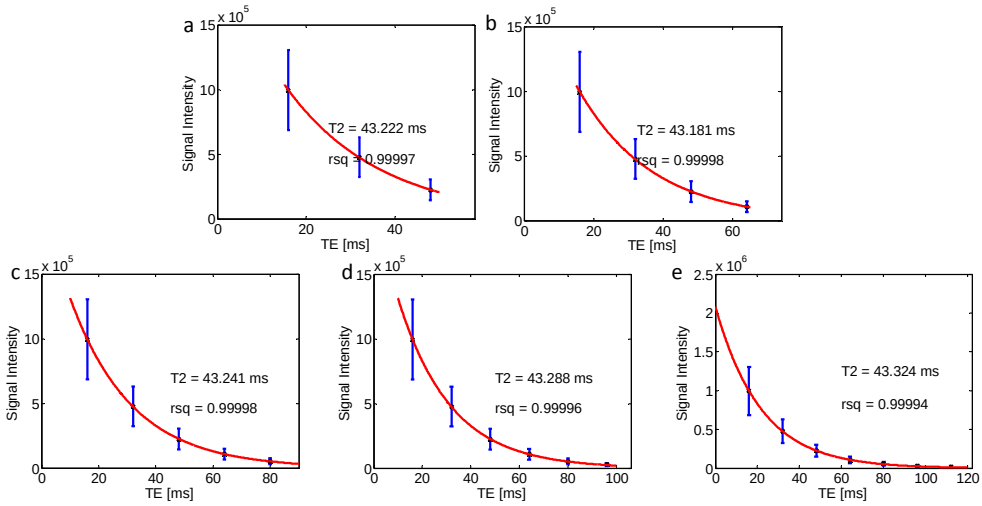

Figure 10: Effect on T_2 by fitting points from an increasing number of echo times. Effect of fitting points from 3-7 echo times: for (a)-(e) respectively. T_2=42.22, 43.18, 43.24, 43.29 and 43.43 ms for (a)-(e) respectively. Error bars represent the standard deviation of values within the region of interest.

In order to correct for this problem, Miller et al.(145) demonstrated that subtracting the squared background signal from the square of the magnitude of the image (otherwise known as the power of the signal) leads to a new noise-corrected image. The corrected T_2 decay constant is then equal to twice the decay constant from the power images (equation **15**). In the case of low SNR in later echoes, this method can drastically improve the curve fitting and thus T_2 estimation as confirmed in Figure 9. Figure 10 shows that after noise correction, fitting points from later echo times in which noise is a large component of the total signal, at most can be seen to cause a negligible lengthening of T_2 estimates.

$$S^2 = S_0^2 \exp\left(-\frac{2TE}{T_2}\right) \qquad \textbf{15}$$

3.5 Structural Imaging

An *in vivo* experiment (n=1) was conducted in order to determine suitable MRI sequence parameters for the structural imaging protocol. As noted in section 2.4, typically multi-echo sequences tend to be more efficient in terms of SNR per unit time than the standard spin-echo sequence. Therefore for structural imaging I have opted to use a fast-spin echo sequence. FSE is used often in structural MRI as it

offers a significant time advantage over single echo techniques. This SNR improvement derives from the fact that several lines of *k*-space are filled within a single TR. A scan with ETL=4 offers a 4 fold acceleration in acquisition time over a standard spin-echo sequence. Figure 11a shows a 3D FSE image with ETL=8, TE_{eff}=41.8 ms and acquisition time=48 min. If the TR is doubled, an ETL of 16 can be used to produce a sequence with the same acquisition time and at the same time offer a 64% improvement in SNR (Figure 11b). As a result of this increase in SNR, it was possible to increase the spatial resolution to have an isotropic voxel-size of 150 μm, whilst retaining sufficient SNR (Figure 11d).

There needs to be a compromise as increasing the ETL means that the lines of *k*-space that are filled at later echo times have lower signal, meaning that the edge of *k*-space, which encodes higher spatial frequencies, records less signal and results in blurring of the image. There are methods to alleviate this problem, for instance by using variable refocusing flip angles, but implementing this is beyond the scope of this project. A visual comparison of Figure 11a and Figure 11b suggested that this did not appear to be a significant problem in the pilot data. The default parameters for the 3D FSE sequence on the Agilent MRI scanner produces images that contained streaking artifacts (Figure 11a,b) which is likely to have occurred as a result of unwanted stimulated echoes. Increasing the amplitude of the crusher gradient, (which nulls transverse magnetisation) was able to remove this artifact as can be seen in Figure 11c. Gibbs ringing artifacts were also present at the interface between the brain and the surrounding tissue (Figure 11d). These were alleviated at the expense of spatial resolution by applying a Tukey filter in *k*-space to smooth the images (Figure 11e).

Several datasets were not able to be used due to signal dropout in the posterior regions of the brain (Figure 12a). This artifact was identified to be due to the frequency pre-scan incorrectly identifying the excitation frequency offset which in turn led to a failure to excite the first 100 slices in the imaging volume as shown by the signal intensity profile in Figure 12b. These datasets were irrecoverable and had to be discarded. The first part of this chapter has been concerned with the development of imaging protocols whilst the remainder focusses on deriving quantitative information from the acquired images.

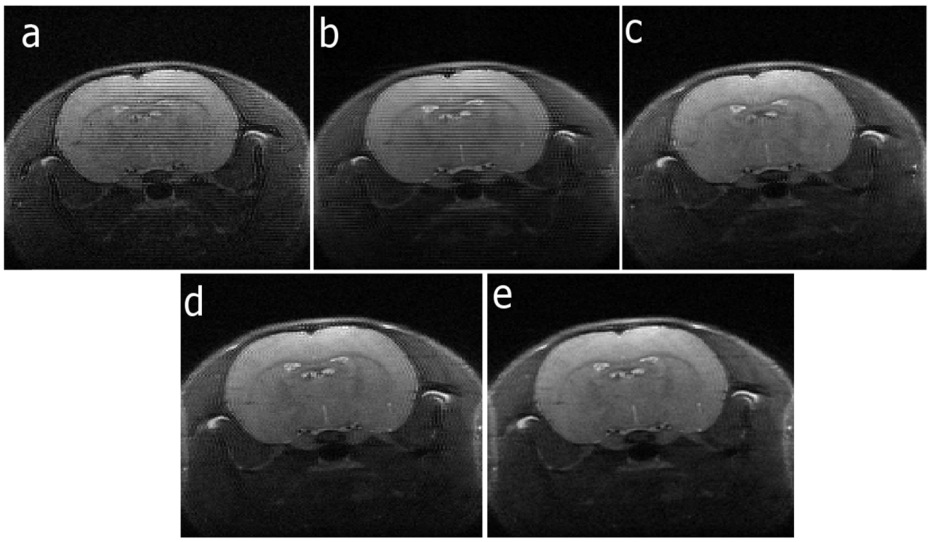

Figure 11: Optimisation of the structural imaging sequence. Images show coronal FSE MRI images at approximately 1.5 mm posterior to the Bregma using the sequence parameters: (a) TR=800 ms, ETL=8, 156 μm isotropic, crusher gradient strength=5 G/cm, SNR=28. (b)TR=1800, ETL=16, 156 μm isotropic, crusher gradient strength =5 G/cm, SNR=46. (c) TR=1800, ETL=16, 156 μm isotropic, crushers=15 G/cm, SNR=44 (d) TR=1800, ETL=16, 150 μm isotropic, crusher gradient strength =12 G/cm, SNR=38. (e) Same as (d) but in addition Tukey filtered in *k*-space to reduce Gibbs ringing.

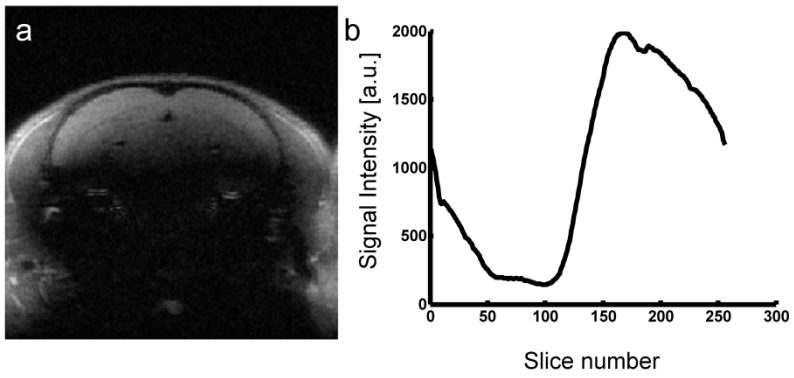

Figure 12:Artifact due to excitation frequency offset. (a) Image from slice number=120. (b) Profile of signal intensity from a region of interest located in the centre of the brain.

3.6 Image Segmentation and Spatial Normalisation

The term image segmentation can be defined as the classification of pixels within an image. In order to derive meaningful information from imaging datasets, image

segmentation is essential. Segmentation problems are subjective by nature and therefore in most situations the ground-truth can be considered to be manual segmentation. Manual segmentation is a hugely laborious task, particularly when dealing with neuroimaging data, in which we are interested in several brain regions or even several hundred brain regions, therefore automated methods are highly desirable. There are numerous approaches to solving this problem that are applicable in different situations but one of the most important issues is how much prior information is used and how it can be incorporated.

Atlas-based segmentations are incredibly useful in neuroimaging and rely on registering (transforming) an atlas (i.e. a pre-segmented image) to the target image (image to be segmented) or vice versa. Recently, multi-atlas approaches have been found to be superior to single-atlas approaches and are starting to be applied to neuroimaging datasets(146).

3.7 Single-Atlas Based Segmentation

Manual region drawing can be incredibly laborious work, for example a typical study in with 3 time-points, 40 subjects and 10 regions of interest (ROIs) per dataset would require 1200 regions to be drawn, which is clearly undesirable and expensive if trained operators are recruited to perform this task. In order to reduce the labour intensiveness of manual region drawing, automated methods can be applied. One of the simplest automated approaches involves registration to a parcellated MRI template (atlas). Prior to the registration, it is often necessary to perform image preprocessing. Three preprocessing steps that can dramatically improve the quality of the image registration are: inhomogeneity correction, intensity normalisation and brain masking. These will be discussed in turn in the following sections.

3.8 Inhomogeneity Correction

Image inhomogeneity or bias fields are smooth variations in signal intensity across images that occur as a result of imaging hardware. It occurs primarily due to the spatially varying sensitivity of receiver coils but can also be caused by non-uniform excitation. Correcting for these inhomogeneities is normally necessary prior to coregistration. By far the most popular algorithm used for bias field correction is the

N3 method(147). Inhomogeneity due to receiver coils can be modelled as a multiplication of the unbiased image as described by equation **16**:

$$v(x) = u(x)f(x) + n(x) \qquad \textbf{16}$$

where v is the acquired image, u is the uncorrupted image, f is the bias field and n is the noise. Two bias field correction methods were tested in this work. The first is based on minimising the entropy of the image histogram which is implemented in SPM 8 and is a modified version of the SPM99 version(148). The second is N4ITK(149), which is a modified version of the well-established N3 algorithm(147) and is contained within the Convert3D image processing companion tool for ITK-SNAP(150). N3 or N4ITK attempt to find the smooth multiplicative field *f(x)* that maximises the high frequency content of the intensity distribution and these methods have been shown to consistently outperform most other available algorithms(151). For this reason N3 has been adopted as the de facto standard. Of the two algorithms tested here, visually, N4ITK (Figure 13c) performs better than the SPM algorithm with default parameters (Figure 13b), in correcting for non-uniformity. Signal inhomogeneity can largely be seen to be caused by the variable sensitivity of the receiver coil as it manifests as a gradual signal drop-off between the dorsal and ventral surface of the brain as well as a decrease in signal intensity from the lateral to medial regions (Figure 13a).

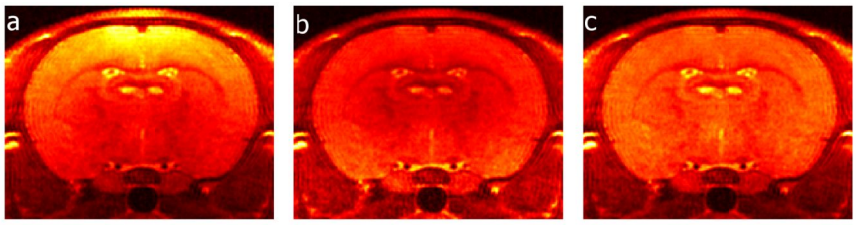

Figure 13: Evaluation of bias field correction methods. (a) Uncorrected image. (b) Bias field corrected using SPM 8. (c) Bias field corrected using N4ITK.

3.9 Intensity Normalisation

MRI signal intensity can vary dramatically in images acquired with the same sequence parameters across different sessions. It is possible that intensity variation to this degree might cause problems for image registration and therefore some degree of

intensity normalisation is sometimes desirable. The simplest type of normalisation can be achieved by linearly scaling intensity values to a new intensity range using equation **17**:

$$I_N = (I - Min)\frac{newMax - newMin}{Max - Min} + newMin \qquad \textbf{17}$$

where I_N is the new image intensity, I is the original intensity, *Min* and *Max* are the original minimum and maximum intensities of the image respectively and *newMin* and *newMax* are the desired minimum and maximum intensities respectively. Whilst a simple method such as the one used above, can ensure that the range of intensities is the same for all images, more complicated methods based on histogram landmarks can offer significant gains in similarity between intensity histograms.

Small numbers of voxels with vastly different intensity values are common in MR datasets. For instance, DC offset artifacts or blood vessels often present as hyperintensities and will skew analyses of histogram parameters such as the maximum, mean and standard deviation (SD). It can therefore be appropriate to remove such outliers before performing intensity scaling. The values that fall within this range can be said to be within the intensity range of interest.

The method that we utilise here for intensity normalisation is an implementation of the work described by Nyúl et al.(152), which is based on firstly, linearly scaling all intensities between the 1st and 99th percentile to a standard intensity range. After this, multiple standard landmarks are then calculated. In this case, the deciles of the intensity values are averaged over all of the training datasets in order to find these standard landmarks. Once these are found, the landmarks of each individual MRI dataset are linearly mapped to the standard landmarks using equation **17**. This algorithm was implemented in MATLAB (MathWorks, Natick, MA) by Nicholas Powell from the Centre for Advanced Biomedical Imaging at UCL.

3.10 Brain Masking and Measurement of Total Brain Volume

Brain masking or brain extraction is essential for many MRI analyses in small animal studies because it improves image registration and also because segmentation of the brain is needed as a measurement of the total brain volume. There has been much

attention focussed on the problem of brain extraction of human MRI datasets and as a consequence there is much freely available software for this purpose. However, the problem of rodent brain extraction has relatively been neglected and software that is designed for human brain extraction performs poorly on rodent brain datasets. Recently, three different methods have been proposed for rodent brain extraction based on deformable surfaces(153), constraint level sets(154) and 2D and 3D pulse-coupled neural networks(155-157).

One of the most successful and widely applied approaches is the Brain Extraction Tool (BET)(158) in FSL (www.fmrib.ox.ac.uk/fsl), which is based on deformable models. In most situations, BET performs adequately, however in this project it was found that an atlas-based approach, which can incorporate a large amount of prior information, was vastly superior to techniques primarily based on morphology and signal intensities. There are two disadvantages to using an atlas-based approach. First, it is less generalizable, therefore will not be as accurate on datasets acquired with different imaging parameters or on subjects with brain morphology that is too dissimilar to that of the atlases and second because it requires the generation of high quality atlases (i.e. a number of datasets that have been segmented to a high degree of accuracy). As generalisation is not a major problem in this work (i.e. we are using the same imaging parameters and adult rodents of the same species and a similar age), an atlas based approach is ideal as it will be highly insensitive to image noise. Furthermore, for the estimation of brain volume, this robustness offers substantial benefits.

In the work presented here, an atlas-based approach was employed, which involved affine coregistration of the pre-segmented MRI templates (atlases) to the target image. Individual registration of multiple templates is known as multi-atlas segmentation, which is a topic that will be discussed in greater detail in the following section. After the registration step, the brain masks (labels) for the atlases were transformed to the target image space. These labels then need to be combined in a process known as label fusion (see section 3.12). Two methods were tested for label fusion: STAPLE(159) and majority voting. The majority voting method was visually better, possibly due to the small number of atlases used in this work. The advantages of using affine coregistration over non-rigid registration are that the high-degree of

regularisation renders the affine method robust to noise (Figure 14) and also affine coregistration is typically fast and can be achieved with computational time of approximately 1 min per atlas on 3D volumes with a 256×256×256 matrix size using the freely available NiftyReg software package (http://cmic.cs.ucl.ac.uk/home/software/)(160). The brain masking algorithm described above was implemented in MATLAB.

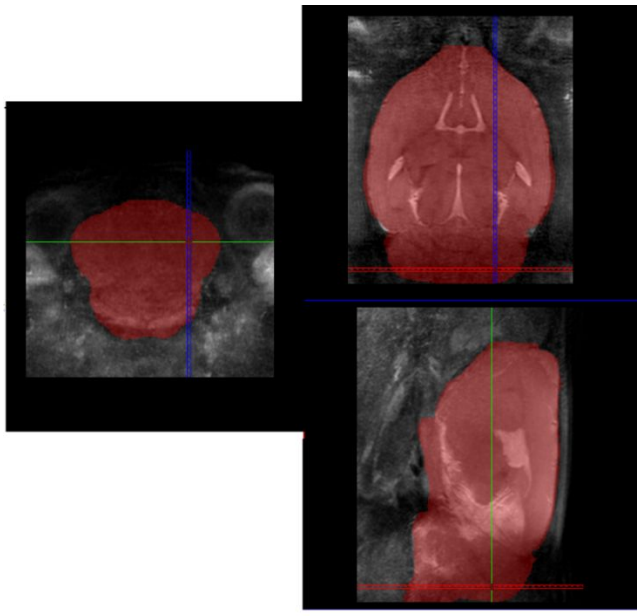

Figure 14: Example of brain masking based on affine registration. This algorithm can be used to estimate brain volumes even when imaging artifacts lead to regions low signal to noise ratio (shown in the cerebellum).

3.11 Multi-Atlas Segmentation

In this project, I am interested in using volumetric MRI as an objective measure of brain injury. There are several advantages of using MRI over histology for this purpose. For instance, MRI can acquire data across the whole brain in 3D, whereas unbiased stereological procedures are needed in histology to extrapolate from multiple tissue sections(161). Furthermore, MRI can be carried out *in vivo*, allowing access to longitudinal data. In order for these methods to be achievable, automated methods of analysis are needed as manual segmentation on high-resolution 3D datasets is hugely laborious. In this section it is shown that highly accurate automatic segmentation of the rat hippocampus can be achieved using a number of already manually segmented datasets. This method is called multi-atlas segmentation and is

currently one of the most accurate techniques available for image segmentation(162-164). Multi-atlas segmentation is an extension of the single-atlas method (in which a single parcellated template is registered to the target image). Another method might be to use a probabilistic framework to incorporate many delineated images into the segmentation. However, in order to gain full advantage of the a priori information that is available, registration to the target image should be performed separately for each of the individual templates in what is known as multi-atlas segmentation.

3.12 Cross-Validation of Automated Hippocampal Volume Measurements

Once the registration has been performed, each atlas has assigned a label to the target image. The combination of these labels is known as label fusion and several different solutions to this problem have been proposed. The simplest of these is the majority voting algorithm, which simply accepts the label that has the largest number of votes. Another popular method of label fusion is the Simultaneous Truth And Performance Level Estimation (STAPLE) algorithm(159). Algorithms that perform the best are those which use global and/or local similarity measures to compare the templates and the target image. For this reason, we have chosen to use the Similarity and Truth Estimation for Propagated Segmentations (STEPS) method, which has been shown to outperform most other freely available label fusion methods for segmentation of the human hippocampus(165) and is freely available in the NiftySeg software package (http://cmic.cs.ucl.ac.uk/home/software/). STEPS is based on using local cross-correlation as a similarity measure for locally selecting the templates which most closely correspond to the target image.

In order to evaluate the accuracy of this method and at the same time optimise the two label-fusion parameters (width of the Gaussian kernel size (k) for cross-correlation and number of atlases), cross-validation was performed using leave-one-out cross validation (LOOCV). LOOCV involves testing the automated algorithm on one MRI volume, whilst using the rest of the dataset as training data (atlases). This is repeated on each observation sequentially in order that each observation is used once for validation and the result from each validation step is averaged.

Preliminary imaging experiments were conducted as part of the pilot experiment outlined in section 3.1. 24 3D FSE datasets were used for LOOCV. These datasets

were from rats imaged prior to SE (n=16) and rats imaged 3 weeks after SE (n=8). The imaging parameters were the same as those shown in Figure 15d. Manual segmentation was used for delineation of the hippocampus and was used as the ground truth for calculation of Dice scores. Dice scores are used here as a measure of segmentation accuracy and were calculated using equation **18**:

$$D = \frac{2|A \cap M|}{|A| + |M|} \qquad \textbf{18}$$

where $|A|$ and $|M|$ are the number of pixels assigned as hippocampus for the automatic and manual segmentations respectively and $|A \cap M|$ is the number of pixels assigned as hippocampus by both automatic and manual methods.

The 3D FSE images were first brain extracted using the method described in section 3.10 and then intensity normalisation was carried out using the method described in section 3.9. After this, every template was registered to every other, firstly by affine registration and followed by non-rigid registration based on free-form deformation using B-splines(166). This was procedure was conducted using the NiftyReg software package. LOOCV and label fusion optimisation was then implemented using a range of label fusion parameters. This was done by adapting a shell-script written by Ma Da from the Centre for Advanced Biomedical Imaging at UCL. The results from this cross-validation can be seen in Figure 15, which crucially demonstrates that both the atrophied (Figure 15c) and healthy (Figure 15b) hippocampus can be segmented with a high degree of accuracy. Using the optimum label fusion parameters for the post-SE rat brain, which were: number of atlases=7 and k=4, the mean Dice score (±standard error of the mean (SEM)) was 0.89±0.0002 for controls and 0.88±0.006 for post-SE rats with hippocampal injury.

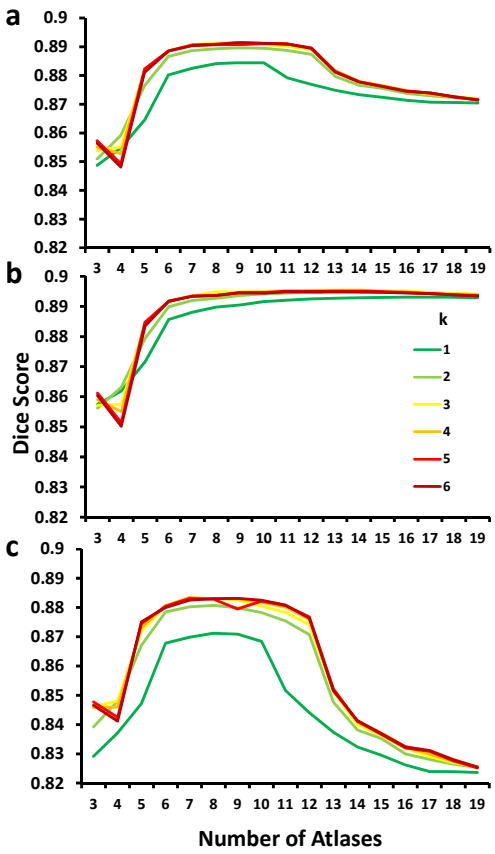

Figure 15: Leave-one-out parameter optimisation for label fusion algorithm. Number of atlases *vs.* Dice Score plotted for different Gaussian kernel size (*k*). Dice scores were calculated between manual segmentation and the proposed method. (a) Including all test datasets (n=24). (b) Including only healthy controls (n=16). (c) Including only post-status epilepticus rats (n=8).

3.13 Spatial Normalisation and Statistical Parametric Mapping

The use of ROIs for measurement of image intensities or other parameters is convenient as it can be used to provide anatomical labels. However, the use of ROIs may also sacrifice sensitivity due to partial volume effects. The risk of this is particularly high in the case where the effect of interest is much smaller than the ROI, e.g. within cell layers of the hippocampus. Using smaller ROIs may circumvent this problem to some extent, but accurate methods of parcellation are necessary in order for these regions to be positioned. One method around this approach is to use spatial normalisation. Spatial normalisation can be performed by coregistration of all images to an atlas, or by performing group-wise registration to create a population-specific template. One of the issues with creating a population specific template is the risk that the group-wise registration can be biased to one of the subjects or groups in the

analysis. This problem can be addressed by continually repeating the registration to the population mean. The initial template image also needs to be selected and can introduce some bias into the final template.

After spatial normalisation has been performed, statistical analysis can be performed on a voxel-wise basis. If parametric statistics are used, this method is called statistical parametric mapping. One of the major issues with this approach is that testing each voxel independently leads to an increased risk of Type I errors (false positives). On the other hand, voxels are likely to be highly correlated and therefore adjusting the significance level using the Bonferroni correction is normally too conservative and leads to Type II errors. Application of this approach to T_2 mapping has been termed voxel-based relaxometry(167).

The most common method for spatial normalisation is the approach implemented in SPM (http://www.fil.ion.ucl.ac.uk/spm/). This involves firstly, segmenting images into three (or more) different tissue classes: grey matter, white matter and cerebrospinal fluid (CSF). Segmentation in SPM is performed using a unified approach(168) that incorporates both bias-field correction and prior information on tissue classes. In order for tissue class segmentation to perform well, the tissue priors should be study-specific. Each voxel is modelled using a mixture of Gaussians and an iterative Expectation Maximisation algorithm is used to optimise the mixture parameters, bias field and deformation of the tissue class probability maps. Following segmentation, tissue classes can then be non-linearly registered to the evolving group-wise average tissue class probability map using DARTEL (Diffeomorphic Anatomical Registration using Exponentiated Lie algebra)(169). This approach to spatial normalisation is the same as that which is implemented in the most recent voxel-based morphometry (VBM) methods. VBM is a highly sensitive technique used to compare local concentrations or volumes of grey matter(148).

3.14 Summary

This chapter has outlined the development of experimental and image analysis protocols. Firstly, preliminary experiments were conducted in the lithium-pilocarpine

model. These experiments indicated that administration of lithium nearer to pilocarpine injections ensures a higher proportion of animals reach SE.

Experimental work was presented that outlined the development of a structural imaging protocol and these datasets were used to optimise automated methods of whole brain and hippocampal volume measurements.

The theory behind using gradient-echo imaging for the detection of iron oxide contrast agents was provided. The next chapter is concerned with *in vivo* imaging of cerebral inflammation using iron oxide contrast agents.

Chapter 4 Molecular Imaging of Inflammation

4.1 Aims

The previous chapter described how superparamagnetic iron oxide particles can be used as a contrast agent for MRI. It was also discussed how the gradient-echo pulse sequence is suited to detection of iron oxide as it is sensitive to magnetic field inhomogeneities. The aim of the current chapter is to determine the feasibility of using iron oxide particles for imaging cerebral inflammation. A secondary aim will be to characterise this imaging agent by determining the optimum dose for *in vivo* imaging and investigating its blood clearance rate and biodistribution.

4.2 Molecular Imaging of Cerebral Inflammation

Cerebral inflammation occurs in various neurological conditions such as stroke, epilepsy, traumatic brain injury, brain tumours and Alzheimer's disease. In these conditions it is known that some inflammatory processes are beneficial and promote repair, whilst others are detrimental. The inducible cell adhesion molecules are key mediators of diapedesis (migration of blood cells through blood vessel walls) and could therefore be used as biomarkers for monitoring anti-inflammatory therapies following brain injury. Recently, imaging vascular cell adhesion molecule-1 (VCAM-1) expression using micron-sized particles of iron oxide (MPIO) coupled with MRI has shown to be an extremely sensitive and highly specific method of detecting and locating inflammation(170-176). The low constitutive expression of VCAM-1 renders it an ideal target for molecular imaging. It is expressed on the surface of endothelial cells within blood vessels, and therefore can be used to monitor pathology or therapies in the brain without the need for contrast agents to cross the blood brain barrier. VCAM-1 mediates the rolling and extravasation of leukocytes across the vascular endothelium(177). Furthermore, it is thought to play a key role in several pathological conditions and may therefore provide a meaningful biomarker of disease progression. For example, it has been suggested that VCAM-1 is used by tumour cells to aid adhesion to the vascular endothelium(178) and section 1.8.8 describes how its expression may exacerbate ictogenesis or the development of epilepsy (epileptogenesis).

4.3 Experimental Design

This study will attempt to synthesise and characterise a VCAM-1 targeting imaging agent. For this study we have chosen to use p-toluenesulfonyl (tosyl) activated MyOne™ Dynabeads® due to their large binding capacity (0.04-0.06mmol/g) and the ease by which they can be conjugated to amine groups on antibodies with high yields. This is the same compound as reported in several *in vivo* VCAM-1 targeting studies reported in the literature(170-172, 176, 178), which suggests that their physicochemical properties are suitable for *in vivo* studies. The manufacturer's specifications state that these are polystyrene beads coated with a polyurethane layer and that 14-19 µg of immunoglobulin G (IgG) subtype of antibody can be conjugated per mg of particles. In the best case scenario, this corresponds to approximately 126 pmol per mg (or 75,900 antibodies per particle) suggesting that binding of antibodies is not limited by the number of tosyl functional groups but by other factors such as steric hindrance or hydrolysis of the tosyl starting material. Furthermore, according to the manufacturer's specifications, these particles are superparamagnetic (Figure 16). As noted in section 3.2, this property reduces the ease with which aggregates are formed.

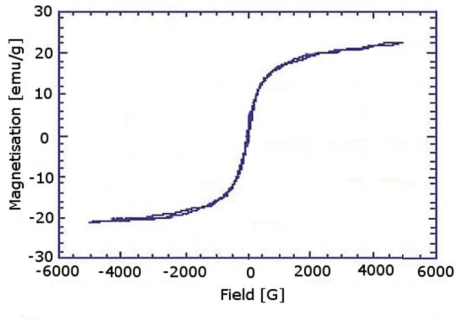

Figure 16: Hysteresis curve for Dynabeads® MyOne™. The magnetisation curves overlap when the magnetic field is increased and then decreased, demonstrating that the iron oxide particles are superparamagnetic. (Adapted from http://www.lifetechnologies.com)

In this study, the VCAM-1 targeting contrast agent is firstly tested *in vitro* for its ability to bind to VCAM-1. This was performed by stimulating rat brain endothelial cells to express VCAM-1 using the inflammatory cytokine tumour necrosis factor alpha (TNF-α). The contrast agent was then labelled using radioactive iodide to enable further *in vivo* characterisation such as the determination of blood clearance

rates and biodistribution. *In vivo* assessment of contrast agent binding was achieved using a model of cerebral inflammation in which TNF-α was administered to one cerebral hemisphere of the brain. This experiment also enabled us to find the approximate concentration of CA required for imaging. Both MRI and single-photon emission computed tomography (SPECT) were then conducted in order to assess the capacity of each of these imaging methods to detect presence of the contrast agent *in vivo*.

4.4 Materials and Methods

4.4.1 Contrast Agent Synthesis

Monoclonal antibodies specific to rat VCAM-1 (MR106) (ebioscience, San Diego, CA) were conjugated to micron-sized (1 μm diameter) iron oxide particles (MPIO, Invitrogen, Life Technologies, U.K.) via the tosyl coupling reaction (Figure 17) using the method described in the manufacturer's specifications. The final product was anti-VCAM-1 antibodies bound to MPIO and henceforth will be referred to as VCAM-MPIO for consistency with the literature. To control for non-specific binding, non-specific IgG antibodies (Southern Biotech, Birmingham, AL) were used in place of anti-VCAM-1 antibodies to generate the IgG-MPIO control CA.

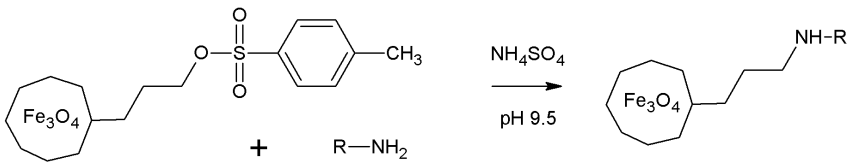

Figure 17: Tosyl conjugation of micron-sized iron oxide particles to free primary amine groups on antibodies.

4.4.2 *In vitro* experiment

The immortalised rat brain endothelial cell line (GPNT) was generously provided by Prof. John Greenwood, Institute of Ophthalmology, University College London. GPNT cells were cultured until confluent in 35 mm diameter well dishes. Cells were treated with 10 ng/ml human recombinant TNF-α (Invitrogen, UK) (n=3) or saline (n=3) in controls and incubated at 37°C for 20 h. VCAM-MPIO was added at a concentration of 0.06 mg/ml media and cells were incubated for 2 h at 37°C then

washed several times with PBS (pH 7.4). Quantitation of contrast agent binding was performed on grayscale images by thresholding at an arbitrary value. Data is displayed as mean±SD.

4.4.3 Radiolabelling

For the *in vivo* characterisation of the MRI contrast agent, the CA was radiolabelled using ^{125}I. VCAM-MPIO was re-suspended in heparinised phosphate-buffered saline (PBS) (100 µl) and radiolabelled using 30-150 MBq of [^{125}I]NaI (PerkinElmer, Billerica, MA). This radiolabelling was carried out by Niral Patel from the Centre for Advanced Biomedical Imaging, UCL, using pre-coated 1,3,4,6-tetrachloro-3α,6α-diphenylglucoluril (Iodogen) tubes (Thermo Fisher Scientific, Rockford, IL), at room temperature for 30 minutes. After this time, the radioactive mixture was purified by magnetic separation to remove any unbound ^{125}I. The washing and purification step was repeated five times. This method incorporates iodine onto the tyrosine groups on the antibody. It is plausible that it also reduces the binding affinity of the iron oxide particles to the target antigen.

4.4.4 *In vivo* experiment

All animal procedures were carried out in accordance with the UK Animals (Scientific Procedures) 1986 Act and institutional ethics regulations. Adult male Sprague-Dawley rats weighing 170-200 g were anaesthetised using a combination of isoflurane (1% in oxygen) and urethane (1.5 g/kg) as the latter can provide stable, long-lasting anaesthesia(179). 300 ng tumour necrosis factor alpha (TNF-α) in 5 µl saline was injected into the right striatum using a Hamilton syringe attached to a 31G needle. Saline was administered in control subjects. Radiolabelled VCAM-MPIO or IgG-MPIO was administered 7 h following TNF-α or saline administration via a cannula inserted into the right external jugular vein.

4.4.5 SPECT/CT

In vivo SPECT/CT (computed tomography) was performed under isoflurane (1% in oxygen) and urethane using a nanoSPECT system (Bioscan Inc., Washington D.C.) approximately 20 min post contrast administration. A physiological monitoring system (SA Instruments, Stony Brook, NY) was used to monitor respiration rate and

rectal temperature. Temperature was maintained at 37±0.5°C using an air warming system. A CT scan was conducted with the following parameters: radial field of view (FOV)=40.5 mm^2, axial field of view=40.9 mm, exposure time per projection=1 s, 360 projections and 55 KvP tube voltage, which resulted in an acquisiton time of 6 minutes. The same FOV was used for helical SPECT, using 2.5 mm pinhole apertures, an exposure time of 15 s per projection and 20 projections resulting in an acquisition time of 5 min.

4.4.6 Magnetic resonance imaging

In vivo MRI was performed using a 9.4 Tesla DirectDrive VNMRS horizontal bore system with a shielded gradient system (Agilent technologies, Palo Alto, CA) and a 4-channel rat head phased-array coil (Rapid Biomedical GmbH, Würzburg, Germany). A physiological monitoring system (SA Instruments, Stony Brook, NY) was used to monitor respiration rate and rectal temperature. Temperature was maintained at 37±0.5°C using an air and water tubing warming system. MRI was performed approximately 1 h following contrast agent administration. Iron oxide was detected using a 3D gradient echo sequence (TR=100 ms, TE=11 ms, matrix=192×192×160, FOV=24×24×26 mm^3, acquisition time≈51 min).

4.4.7 Blood clearance

Blood samples (n=3) were collected from the jugular vein cannula at different time points following tracer administration. After each collection, the cannula was flushed with saline to remove traces of radioactivity. The radioactivity present in the blood samples collected was subsequently measured in a Wizard 2470 Automatic gamma counter (PerkinElmer). Results are expressed as a percentage of injected dose per gram.

4.4.8 *Ex vivo* biodistribution

Adult male Sprague-Dawley rats weighing approximately 200 g (n=3) were anesthetised using isoflurane (4% in oxygen). Radiolabelled contrast agent (5 mg/kg, 8-10 MBq) was administered via the lateral tail vein 10 min after CA administration. Blood was sampled via cardiac puncture before sacrificing the animals. The organs

of interest were removed, and measured using a gamma counter. Results are expressed as a percentage of injected dose per gram ± standard error of the mean.

4.4.9 SPECT Reconstruction

SPECT images were reconstructed using the HiSPECT software package (Bioscan, Washington, USA) using the following parameters: smoothing=45%, resolution=67%, iterations=10. CT reconstruction was performed using InVivoScope (InviCRO, Boston, MA).

4.4.10 MRI Quantification of Contrast Agent Binding

Brain extraction was performed using the Brain Extraction Tool (BET) in FSL(158). Hypointensities caused by the presence of iron oxide were segmented using adaptive thresholding in order to take into account local variations in signal intensity. This was achieved by subtracting the MRI volume from the volume convolved with a 3-dimensional Gaussian kernel of size 15×15×15 voxels, followed by thresholding with the same empirically determined threshold used across all datasets. Regions of interest were defined as the entire (left or right) cerebral hemisphere across 30 consecutive slices anterior and 30 slices posterior to the injection site, thus excluding the cerebellum. CA binding was expressed as the percentage of total ROI volume.

4.4.11 SPECT Quantification of Contrast Agent Binding

Brain extracted MRI images were coregistered to the CT images and ROIs were propagated into CT native space using the same transformation. In this way, identical ROIs were used for both the MRI and SPECT analysis. Background signal intensity was defined as the mean signal intensity across all non-brain tissue and CA binding was expressed as the target-to-background ratio to account for the large range of radioactivity used.

4.4.12 Coregistration

Rigid coregistration of MRI and CT images was performed in AMIRA® (Visualization Sciences Group, Burlington, MA) on the gradient-echo images of the brain extracted MRI magnitude data and the CT intensity images using normalised correlation as the cost function. SPECT images were realigned to CT images using

rigid registration with normalised mutual information as the cost function in the InVivoScope software package.

4.4.13 Statistical Analysis

Statistical analysis was performed using one-way ANOVA and unpaired two-tailed t-tests. Statistical significance was assigned at $p<0.05$.

4.5 Results

4.5.1 *In vitro* experiment

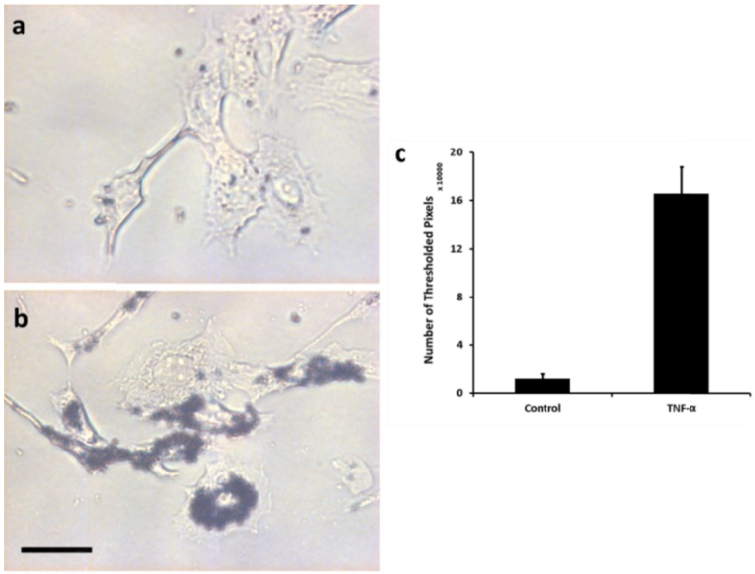

Figure 18: *In vitro* binding of VCAM-MPIO to TNF-α stimulated rat brain endothelial cells. (a) and (b): Bright-field microscopy of rat brain endothelial cell line. 1 µm diameter iron oxide particles can be visualised as dark circular regions on bright field light microscopy.(a) GPNT cells without TNF-α treatment, incubated with VCAM-MPIO for 1 h and washed several times (n=3). Very few particles could be observed binding to untreated cells. (b) GPNT cells treated with TNF-α for 20 h in order to induce VCAM-1 expression, labelled and washed in the same manner as panel a (n=3) (magnification ×400, scale bar=10 µm). (c) Quantitation of iron oxide binding using thresholding.

The rat brain endothelial cell line (GPNT) is known to express VCAM-1 when treated with TNF-α(180). After being treated with TNF-α, GPNT cells showed strong VCAM-MPIO binding (Figure 18b,c). Very little binding was observed in untreated cells (Figure 18a,c) demonstrating the binding of the contrast agent to VCAM-1 in vitro (number of thresholded pixels=166,000±21,900 *vs.* 11,900±3800, p=0.02).

4.5.2 Blood clearance and Biodistribution

Ex vivo biodistribution studies in healthy rats showed significant uptake of the radiolabelled probe in the lungs (4.8±0.9% ID (injected dose)/g), spleen (3.4±1.7% ID/g) and liver (1.5±0.3% ID/g), (Figure 19b). A similar distribution was observed from whole body *in vivo* SPECT images (Figure 19c). Remarkably, the radiolabelled probe was almost completely cleared from the blood within 2 minutes of administration (Figure 19a). This extremely rapid clearance rate precluded a quantitative estimation of the clearance rate due to experimental limitations. Approximately 0.2% injected dose/g of tracer remained in the blood pool even after 10 min.

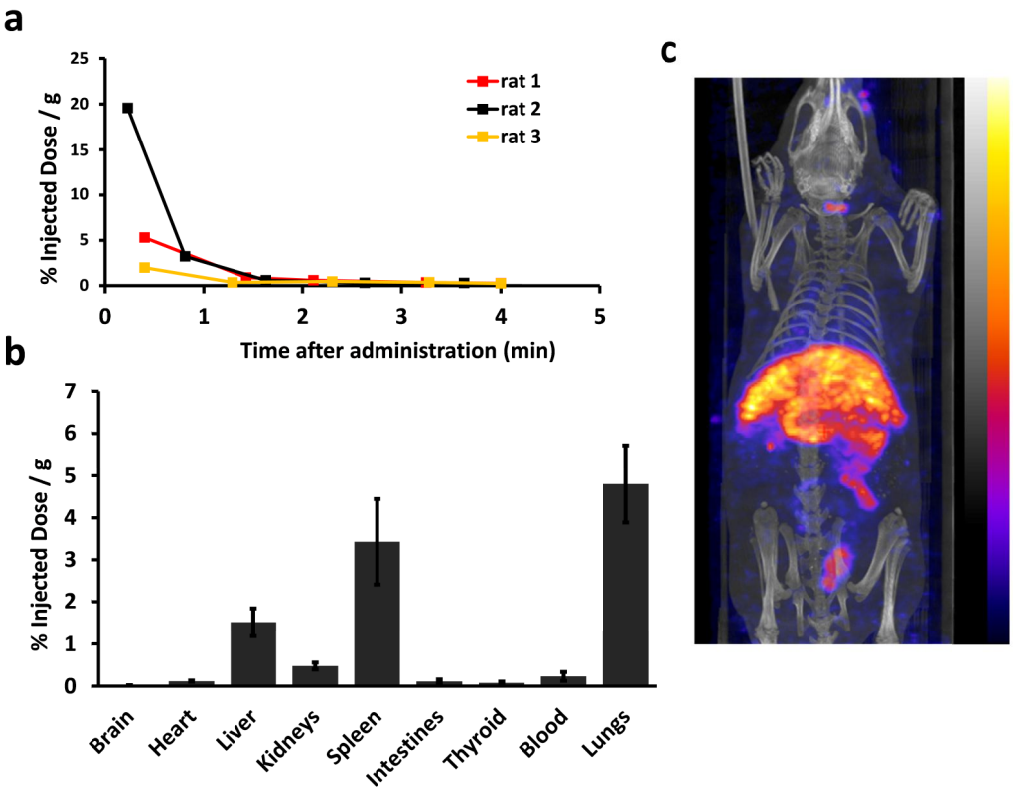

Figure 19: *Ex vivo* biodistribution and blood clearance of MPIO. (a) Blood clearance of ^{125}I labelled micron-sized iron oxide particles (n=3). (b) *Ex vivo* biodistribution at 10 min post administration (n=3). (c) Whole body *in vivo* SPECT/CT maximum intensity projection.

4.5.3 *In vivo* experiment

The contrast present on MRI images depends on the dose of MPIO used. Very little hypointensity can be observed with a 2 mg Fe/kg dose (Figure 20c), whereas marked

contrast is exhibited at 5 and 6 mg Fe/kg (Figure 20d,e). Noticeably more CA binding was observed in TNF-α treated animals (Figure 20d) compared to controls (Figure 20a,b), which could be demonstrated using *in vivo* quantitation using MRI (Figure 21 a) and SPECT (Figure 21b). Local thresholding performs well for the segmentation of hypointense regions (Figure 20f,g,h) There was a significant difference between the group means in the affected hemisphere as assessed by MRI ($p<0.0002$) but this did not reach the significance level for the SPECT quantitation ($p=0.1$). CA was localised predominantly to the affected (right) cerebral hemisphere in TNF-α treated animals (Figure 20h) and contrast volume in the right hemisphere was significantly different from the left cerebral hemisphere based on the *in vivo* MRI quantitation ($p<0.02$) (Figure 21a). This distribution of CA binding can be seen in the 3D reconstruction (Figure 23b).

Coregistration of CT and MRI using cross-correlation performed particularly well when the MRI (brain extracted) gradient images were used (Figure 22c,g), for the reason that the majority of contrast from CT images is between the skull and soft tissue. Following coregistration, good colocalisation can clearly be observed between hypointensities on MRI images and hyperintensity on SPECT images (Figure 22h).

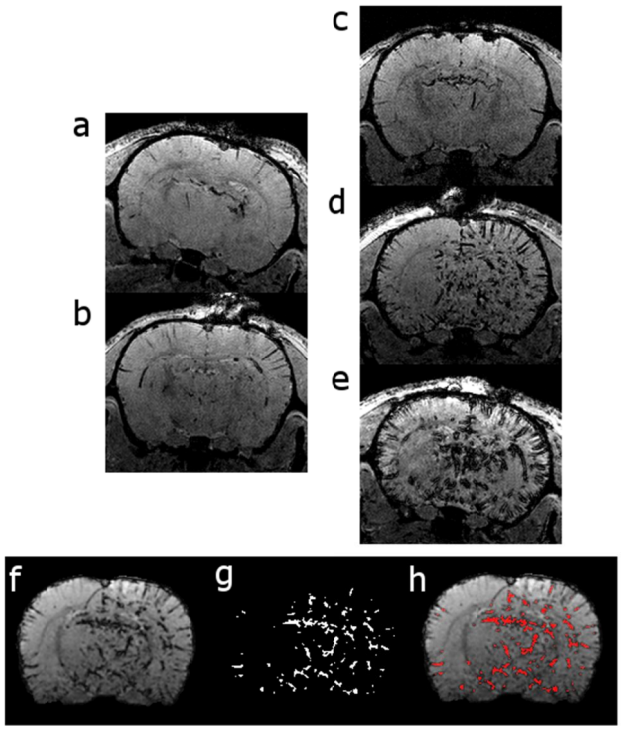

Figure 20: Binding of ^{125}I labelled VCAM-MPIO or control IgG-MPIO as visualised on 3D gradient echo MRI images. (a)-(e): Coronal MRI images at the level of the striatum, following administration of: (a)Intracerebral saline + VCAM-MPIO (5 mg/kg), (b) Intracerebral TNF-α + IgG-MPIO (5 mg/kg), (c) Intracerebral TNF-α + VCAM-MPIO (2 mg/kg), (d) Intracerebral TNF-α + VCAM-MPIO (5 mg/kg),(e) Intracerebral TNF-α + VCAM-MPIO (6 mg/kg). Illustration of quantitation procedure: (f) Brain masking achieved using BET, (g) hypointense regions are segmented using local thresholding. (h) Segmented regions overlaid in red upon the original MRI image.

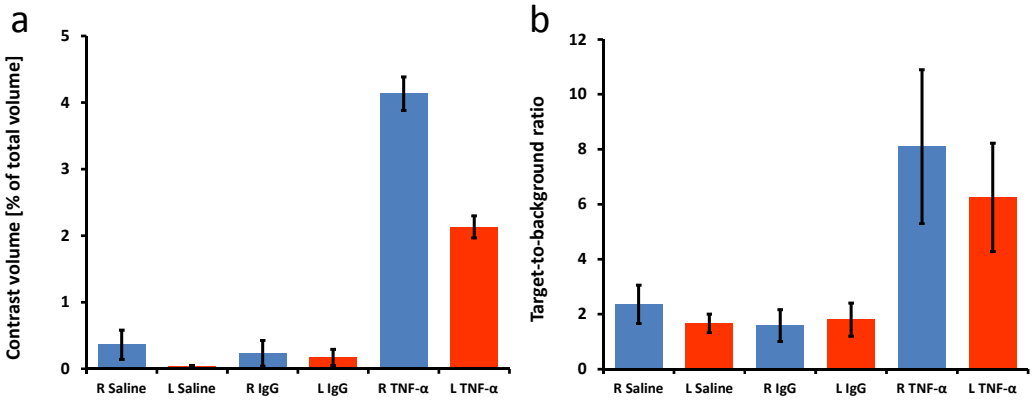

Figure 21: Quantitation of VCAM-MPIO binding using MRI and SPECT. (a) Contrast agent binding as assessed using *in vivo* MRI. (b) Contrast agent binding as assessed using *in* vivo SPECT.

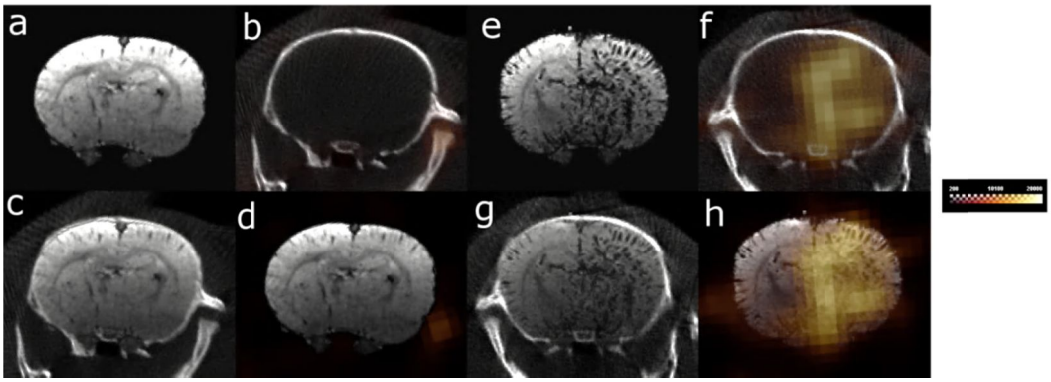

Figure 22: Bimodal *in vivo* imaging of VCAM-1 expression.
(a)-(d): Intracerebral Saline + VCAM-MPIO control. (e)-(h): Intracerebral TNF-α + VCAM-MPIO. (a),(e): Coronal MRI. (b),(f): Coronal SPECT/CT. (c),(g): Coregistration of MRI and CT images. (d),(h): SPECT overlaid on MRI images.

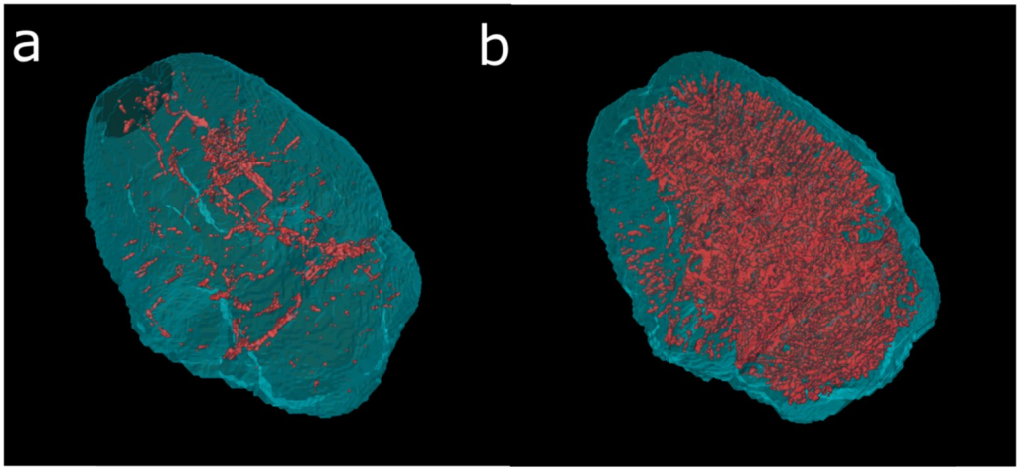

Figure 23: 3D reconstruction of VCAM-MPIO binding in TNF-α model of cerebral inflammation as assessed by *in vivo* MRI. Segmented hypointense regions are shown in red and are primarily caused by VCAM-MPIO contrast agent binding to VCAM-1 on endothelial cells, following intracerebral administration of: (a) Saline. (b) TNF-α.

4.6 Discussion

A bimodal imaging agent targeting VCAM-1 has successfully been synthesised and characterised. This study has demonstrated that bimodal imaging of VCAM-1 expression is feasible. The discrepancy in quantitation between the two techniques is likely to arise from the presence of a higher background signal in the nuclear imaging modality and could also be caused by skull and tissue attenuation of the low

energy gamma ray emitter used in this study. From the synthesis perspective, the presence of superparamagnetic iron oxide makes purification of the radiotracer fast and straightforward. Along with this, the short radiolabelling time (30 minutes) and high radiochemical yields (>80%) demonstrate how this synthetic method would be highly beneficial for radioisotopes with shorter half-lives. Iodine-125 was selected for this study as it offers straightforward and reliable labelling. Nevertheless, an isotope that can be chelated onto the iron oxide construct might render the probe more stable.

Ex vivo biodistribution studies showed uptake of the radiolabelled probe in organs known to be involved in clearance of iron oxide particles from the blood. The high accumulation in the lungs is likely to reflect obstruction of the pulmonary vasculature, whilst high liver and spleen uptake is due to clearance of particles by the reticuloendothelial system. A similar pattern of distribution was observed on *in vivo* images, however a high lung uptake was not detected. The discrepancy between these results is likely due to the fact that in the biodistribution study data is reported as a fraction of the tissue mass (percentage of injected dose/g) and SPECT imaging reflects activity per volume.

Radiolabelled VCAM-MPIO was almost completely cleared from the blood within 2 minutes. This rapid clearance demonstrates that in order to avoid signal from free MPIO in the blood, *in vivo* imaging can be performed soon after administration of the radiolabelled CA. Nanoparticles typically show clearance rates on the order of hours and so these results suggest that micron-sized particles could lead to higher signal-to-background ratios than nanoparticles because the bound contrast agent will also be cleared at a rate which is on the order of hours(170). The presence of 0.2% ID/g in the blood even after 10 min indicated the possibility that free iodide was present or that circulating macrophages took up some of the MPIO from the blood.

This study has shown that particulate-based contrast agents can be used to deliver large quantities of radiotracers to the vasculature of the brain. Using nano- or micron-sized constructs has numerous advantages over small molecular weight agents when it comes to targeting the vasculature. These include: fast blood clearance, reduced non-specific binding and high sensitivity. The presence of a nuclear imaging probe over and above the iron oxide contrast agent could be used in

the future to assess the kinetics of ligand dissociation and provide more accurate quantification of contrast agent binding.

MRI can be seen to offer some advantages over nuclear imaging in this technique, particularly with regard to partial volume effects and lower background signal. The comparison in sensitivity between the two modalities is naïve as relatively low doses of a low energy emitter are used in this work. ^{125}I decays by emission of gamma rays with a maximum energy of 35 keV. In contrast, the positron emission tomography (PET) tracer ^{18}F decays to form positrons, which release high energy (511 keV) gamma rays on annihilation. SPECT offers some advantages over MRI with paramagnetic iron contrast in that it confers positive contrast, is quantitative and also can be multiplexed i.e. radioisotopes with different photon emission energies can be used in a single experiment and distinguished from one another *in vivo*.

4.7 Conclusions

In conclusion, this study has demonstrated the feasibility of performing bimodal imaging of cerebral inflammation using SPECT and MRI and has enabled a comparison between the two techniques. Without further optimisation, detection of CA using MRI appears to be superior to SPECT in terms of sensitivity. This is surprising but could be owing to a number of factors, such as: the background signal in the blood reducing the sensitivity of the nuclear imaging, signal attenuation from tissue absorption of the low energy gamma rays and possibly also due to the more limited resolution of SPECT resulting in partial volume effects. The higher background signal might be due to instability of the nuclear imaging tracer and therefore improving this might lead to enhancements in sensitivity. This study has found that approximately 5 mg of iron per kg appears to be appropriate for *in vivo* imaging of cerebral inflammation in the rat based on the compound synthesised here and also that blood clearance of MPIO is extremely rapid so that imaging can be performed soon after injection to maximise contrast. This information will be helpful for the next chapter in which imaging of seizure-induced inflammation is attempted.

Chapter 5 Imaging Seizure-induced Inflammation

5.1 Aims

The previous chapter showed that using iron oxide particles coupled with MRI provides an extremely sensitive method of detecting cerebral inflammation. Cerebral inflammation was induced by direct intracerebral injection of a pro-inflammatory cytokine. In this chapter it is hypothesised that it is possible to detect the cerebral inflammation that occurs following status epilepticus. Parts of this chapter have been published(181) and are reproduced with permission from Elsevier (copyright 2012).

5.2 Introduction

As mentioned in section 1.7, there is mounting evidence to suggest that inflammation may be involved in ictogenesis and also the development of some partial epilepsies. Non-invasive imaging of inflammation would enable tracking of the temporal progression of inflammation following epileptogenic insults. The previous chapter discusses how VCAM-1 conjugated to micron-sized iron oxide particles is ideally suited as an imaging agent due to the low background expression of VCAM-1 in normal healthy tissue and the ability of these particles to deliver a large payload of iron. Section 4.2 noted that VCAM-1 plays a role in leukocyte adhesion. As leukocyte adhesion is correlated to BBB permeability(182), we hypothesise that VCAM-1 expression occurs prior to vasogenic oedema and the associated T_2 changes(44, 183). Imaging VCAM-1 expression could therefore provide an early and more sensitive marker of inflammation or subtle alterations in blood-brain barrier permeability that cannot be detected clinically using gadolinium based contrast agents(178) or T_2 weighted MRI(171). In this study, an attempt is made to image seizure-induced endothelial activation using micron-sized particles of iron oxide conjugated to anti-VCAM-1 antibodies (VCAM-MPIO) soon after termination of lithium-pilocarpine induced status epilepticus in rats.

5.3 Materials and Methods

5.3.1 Animal Model

All animal procedures were carried out in accordance with the UK Animals (Scientific Procedures) 1986 Act and institutional ethics regulations. Adult male Sprague-Dawley rats weighing 180-230 g (n=12) were obtained from the breeding colony of the University College London Animal Facility. All rats were housed in a controlled temperature and humidity environment with a 12 h light/dark cycle with food and water provided ad libitum. Animals were separated into three groups: Lithium-pilocarpine control group which did not undergo status epilepticus given VCAM-MPIO contrast ($Control_{VCAM}$) (n=4) (Figure 24a), lithium-pilocarpine induced status epilepticus with IgG-MPIO contrast agent to control for non-specific binding and leakage through the blood brain barrier (SE_{IgG}) (n=3) (Figure 24b) and lithium-pilocarpine induced status epilepticus with VCAM-MPIO contrast (SE_{VCAM}) (n=5) (Figure 24c).

It has been previously shown that lithium and pilocarpine may directly cause peripheral inflammation(184), and could conceivably also directly lead to central nervous system (CNS) inflammation. To control for this effect, the control group received diazepam (10 mg/kg, i.p.) injections prior to the injection of lithium and pilocarpine (Figure 24a). Injection of diazepam prior to the injection of pilocarpine has shown to completely prevent the development of SE(185).

In the SE_{VCAM} group (Figure 24c) and SE_{IgG} group (Figure 24b), animals were pretreated with lithium chloride (3 mEq/kg, i.p.) 2 h prior to methylscopolamine (5 mg/kg, i.p.) injection. Methylscopolamine was administered to reduce the peripheral effects of pilocarpine. This was followed 20 min later by administration of pilocarpine hydrochloride (30 mg/kg, i.p.) in order to induce status epilepticus. Animals were behaviourally assessed on using the Racine scale (section 1.5.6). Diazepam (10 mg/kg, i.p.) was administered 90 min after the onset of SE to terminate the seizure. Further injections of diazepam were administered as required. The $Control_{VCAM}$ group (Figure 24a) received a lithium chloride injection (3 mEq/kg, i.p.), a subsequent injection of diazepam (30 min prior to pilocarpine injection) to

prevent SE onset(185), followed by methylscopolamine (20 min prior to pilocarpine injection) and pilocarpine (30 mg/kg).

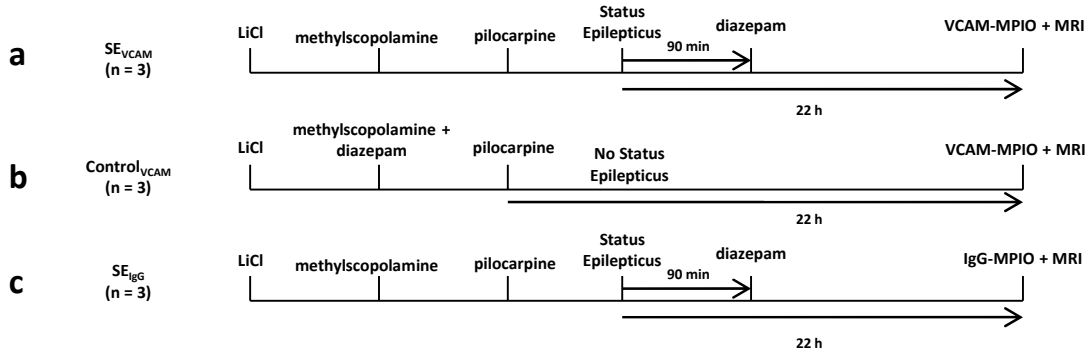

Figure 24: Study design showing the three treatment groups.
(a) Control$_{VCAM}$ group received a single diazepam injection in order to prevent SE and received VCAM-MPIO contrast agent. (b) SE$_{IgG}$ group underwent status epilepticus and received a control contrast agent IgG-MPIO. (c) SE$_{VCAM}$ group underwent status epilepticus and received VCAM-MPIO contrast agent.

5.3.2 *In vivo* MRI

MRI was performed using the system described in section 4.4.6 before and after injection of the contrast agent. Animals were anesthetised with 4% isoflurane and maintained at 1.5-1.6% isoflurane in pure oxygen (1 L/min) throughout the imaging protocol. A physiological monitoring system was used to monitor respiration rate and rectal temperature. Temperature was maintained at 37±0.5˚C using an air warming system. VCAM-MPIO (4 mg of iron/kg) was injected via a cannula inserted into the right external jugular vein 21.9±0.2 h post-SE onset or 22.1±0.2 h post-pilocarpine administration in control subjects. Animals were imaged 1 h post CA administration. The imaging parameters were as follows: 3D spoiled gradient-echo, TR=100 ms, TE=6.5 ms, FA=30º, matrix=192×192×128, FOV=22×22×20 mm^3, acquisition time=40 min. The images were zero filled to 256×256×256, giving a final voxel size of 86×86×78 µm^3. T_2 measurements were performed before injection of the contrast agent with a multislice multi-echo spin-echo sequence across 13 contiguous slices: TR = 2 s, TE=8, 16, 24, 32, 40, 48, 56, 64, 72, 80, 88, 96, 104, 112, 120 ms, matrix = 128×128, FOV=25×25 mm^2 slice thickness=1 mm, acquisition time=4 min.

5.3.3 *Ex vivo* MRI

Approximately 4 h after contrast agent injection, animals were perfused-fixed with 50 ml PBS (pH 7.4) followed by 50 ml paraformaldehyde (PFA) (4% in PBS, pH 7.4) via a cannula inserted into the left ventricle. The brains were removed and immersed in PFA (4%) overnight. The fixed-brains were immersed in Fomblin (type PFS-1, Solvay Solexis S.p.A., Bollate, Italy) for *ex vivo* MRI using a 26 mm diameter birdcage coil (Rapid Biomedical GmbH). The imaging parameters were as follows: 3D SPGR, TR=350 ms, TE=9.8 ms, FA=60º, matrix = 300×300×300, FOV=20×20×20 mm, total acquisition time=8 h 45 min. The images were zero-filled to 512×512×300 and then downsampled to 512×512×150 giving a final voxel size of $39\times39\times133\ \mu m^3$.

5.3.4 Segmentation of contrast volume and T_2 analysis

The brain was manually segmented on gradient-echo images on 40 contiguous slices. Regions were classified as hypointense using an automated segmentation algorithm implemented in MATLAB. This was similar to the approach described in section 4.4.10. Firstly, intensity scaling was conducted using equation **17** to transform intensity values to within the range 0 and 1. Hypointense regions were thresholded if they were less than the local median-C, where C is an empirically determined constant. The local median was calculated using a 3D median filter with a radius of 5 voxels. Nearest neighbour connectivity was then determined in 3 dimensions (objects were defined as connected if they shared at least one vertex) on the thresholded data and objects were discarded if the object size was below a threshold cluster size of 4 voxels as these were likely to be due to noise. Quantitative T_2 measurements were performed using the multi-slice multi-echo spin-echo sequence data by calculating power images (section 2.3) and fitting a single exponential decay to the mean signal across a ROI using the non-linear least squares function in MATLAB. The first two echo times were excluded from the analysis as this minimised errors resulting from stimulated echoes and produced a better fit to a mono-exponential function. For both datasets ROIs were drawn by an observer blinded to the animal groupings over 4 different brain regions including the dorsal hippocampus, cerebral cortex, thalamus and piriform cortex using a standard rat brain atlas(186).

5.3.5 3D reconstruction

3D reconstruction was conducted on separate *in vivo* datasets acquired 2 h post contrast administration. Hypointense regions were segmented using the same algorithm as above. The imaging parameters were as follows: 3D spoiled gradient-echo, TR=100 ms, TE=11 ms, FA=15º, matrix=192×192×128, FOV=25×25×20 mm^3. The images were zero filled to 256×256×192.

5.3.6 Statistical analysis

Unless otherwise stated, Differences between groups were compared using the non-parametric Kruskal–Wallis test and Wilcoxon rank-sum tests. Statistical significance was assigned at $p<0.05$. Data is displayed as mean±SEM.

5.4 Results

5.4.1 Animal Model

All animals in the SE_{VCAM} group and the SE_{IgG} group progressed to status epilepticus. All animals displayed akinesia and facial automatisms which progressed to tonic–clonic seizures and status epilepticus within 60 min of pilocarpine administration. None of the animals in the control group displayed any signs of behavioural seizures. Mean Racine seizure scores (n=3) following SE onset were: 0–30 min=3.2±0.2, 30-60 min=4.1±0.2, 60–90 min=4.7±0.4.

5.4.2 Magnetic Resonance Imaging

Hypointense regions caused by VCAM-MPIO binding are clearly present on the *in vivo* MRI images in the SE_{VCAM} group and appear to be maximal in the periventricular organs (Figure 25c). Additionally, hypointense regions also appear to be present predominantly in the hippocampus and the cerebral cortex on *in vivo* images. Hypointensities were not identified in these regions in the pre-injection images. A similar distribution was observed on high resolution *ex vivo* 3D gradient-echo images, corroborating that these hypointensities are caused by the VCAM contrast agent. The $Control_{VCAM}$ and SE_{IgG} groups showed very few hypointensities on MR images on both *in vivo* and *ex vivo* images, demonstrating that VCAM-1

expression was seizure induced and also that there is little non-specific binding or leakage across an impaired BBB (Figure 25a,b).

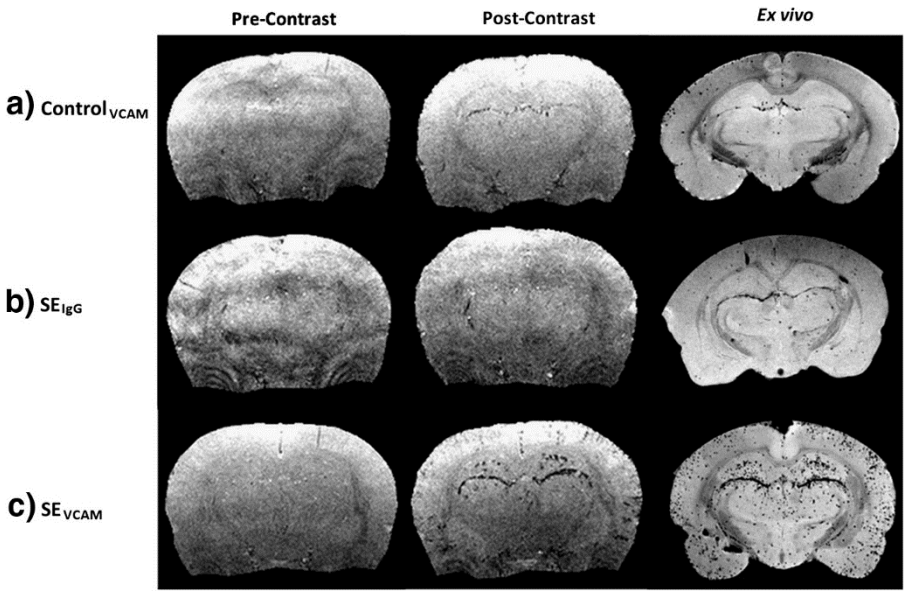

Figure 25: 3D gradient-echo images pre-contrast, post-contrast and *ex vivo*. Coronal MR image slices of 78 μm thickness at approximately 3.8 mm posterior from the bregma are shown for a representative animal from each group. Images were acquired 22 h after SE or pilocarpine administration, approximately 1 h after contrast agent administration and *ex vivo* images were acquired at the end of the study. (a) SE_{VCAM} group rat receiving 4 mg iron per kg VCAM-MPIO. Focal hypointense regions can be observed in the periventricular organs, hippocampus and cerebral cortex both in vivo and ex vivo following contrast agent administration. (b) $Control_{VCAM}$ group which did not undergo status epilepticus injected as in panel a, demonstrating an absence of contrast agent binding. (c) SE_{IgG} group administered with a control contrast agent IgG-MPIO as in panel a. An absence of contrast agent demonstrates that there was little non-specific binding or leakage through the impaired blood brain barrier.

5.4.3 Quantitation of the inflammatory response

Significantly more hypointense volume was observed in the hippocampus SE_{VCAM} group compared to the $Control_{VCAM}$ group and the SE_{IgG} control (Figure 26b) (7.0±2.2% *vs.* 0.5±0.3% and 0.5±0.2%) (p=0.02). The volume of hypointensity measured in the cerebral cortex was also significantly greater in the SE_{VCAM} group compared to control groups (10.5±4.6% *vs.* 1.1±0.6% and 1.2±0.5%) (p=0.02). Hypointense volumes in the thalamus were much less marked than in the cerebral cortex or the hippocampus (2.9±1.6% *vs.* 0.2±0.09% and 0.5%±0.2%) (p=0.02). Three-dimensional reconstructions display this distribution of contrast agent binding (Figure 27). Small amounts of hypointensity can be observed in the SE_{IgG} group in the

regions surrounding the ventricles and in larger blood vessels (Figure 27), this is likely to reflect the limitations in distinguishing between the presence of contrast agent and the differences in magnetic susceptibility in the normal brain (particularly at high field strength), which usually present at air-tissue, tissue-cerebrospinal fluid interfaces and large blood vessels. T_2 measurements were not significantly elevated in the SE group compared to the control group in the hippocampus, cerebral cortex, or the thalamus (Figure 26a). T_2 values were higher in the piriform cortex of the SE_{VCAM} group compared to the $Control_{VCAM}$ group (81±6.2 ms *vs*. 55±0.41 ms) (p=0.02).

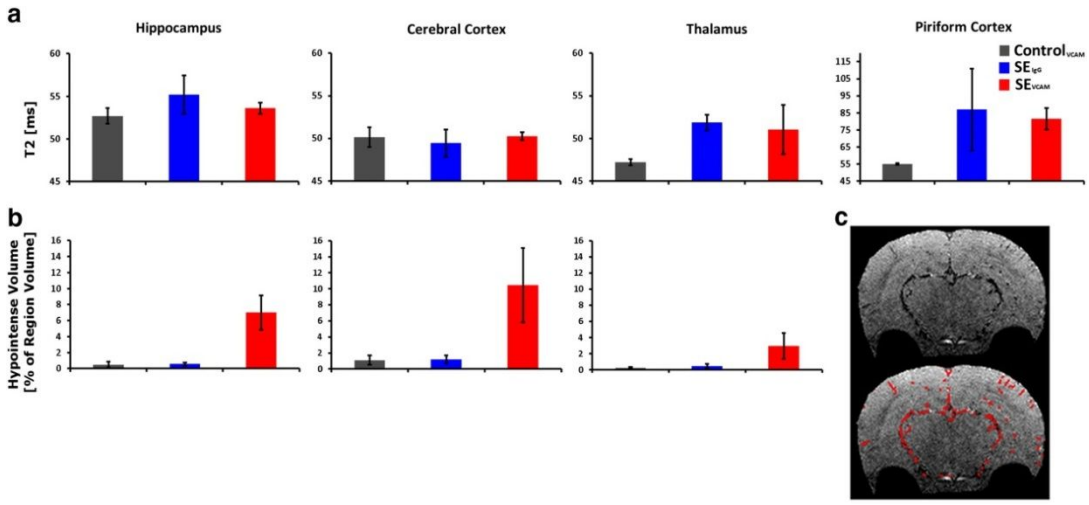

Figure 26: *In vivo* T_2 measurements and quantitation of iron oxide binding. T_2 measurements in the hippocampus, cerebral cortex, thalamus and piriform cortex immediately prior to injection of VCAM-MPIO contrast agent for three different groups: $Control_{VCAM}$ (n=4), SE_{IgG} (n=3), SE_{VCAM} (n=5). (b) Hypointense volume as a percentage of total region volume following injection of VCAM-MPIO or control IgG-MPIO in the hippocampus, cerebral cortex and thalamus. (c) Example segmentation of hypointense regions for coronal MRI image approximately 5 mm posterior to the bregma. Lower image: segmented regions overlaid in red.

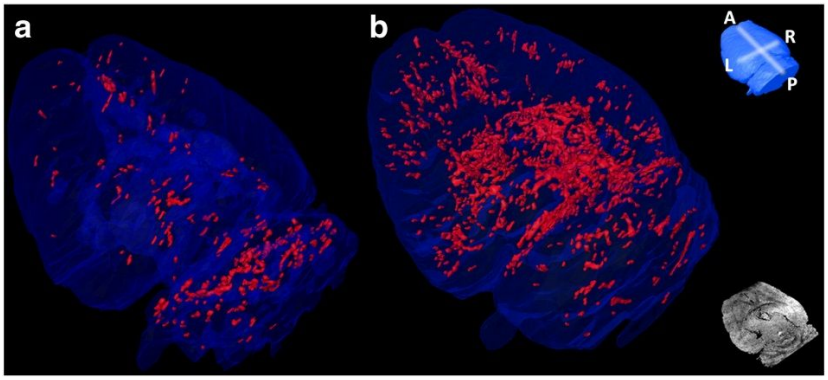

Figure 27: Imaging VCAM-1: three-dimensional reconstruction showing hypointense regions. Segmented hypointense regions are shown in red. Hypointensities were automatically segmented using a local thresholding approach. (a) $Control_{VCAM}$ rat following administration of VCAM-1 targeted contrast agent. (b) SE_{VCAM} rat which underwent status epilepticus approximately 22 h prior to contrast administration. Upper inset: surface rendered brain with orientation planes: A-anterior, P-posterior, L-left, R-right. Lower inset: axial slice for anatomical reference.

5.5 Discussion

In this study we have used antibody targeted superparamagnetic iron oxide particles to track the distribution of VCAM-1 expression *in vivo*. This is the first study to identify regions of inflammation following seizure induced inflammation using *in vivo* MRI detection of VCAM-1. We have also demonstrated that binding of the contrast agent occurred prior to the more commonly used MRI biomarkers (T_2 measurements) of seizure induced brain injury. Our results suggest that there is regional expression of VCAM-1 leading to focal hypointensities on MR images following administration of a VCAM specific contrast agent. We observed maximal contrast at the periventricular organs. This perhaps is to be expected as the periventricular organs, which are incompletely protected by the blood brain barrier, are thought to provide points of entry for proinflammatory cytokines into the brain(187-189). Furthermore, hypointense regions are also clearly present in the regions which are widely associated with neuronal damage following seizures, in particular the hippocampus and the cerebral cortex appeared to be the most significantly affected regions and to a lesser extent the thalamus. This distribution of iron oxide could be readily verified from *ex vivo* MRI images demonstrating that this is not confounded by partial volume effects.

Our data suggest that seizure induced expression of VCAM-1 occurs primarily in the regions which are most affected following status epilepticus. Synchronous neuronal firing in the lithium-pilocarpine model appears to originate in the ventral forebrain or limbic regions(185, 190, 191). Following this, spiking activity spreads to cortical regions(185). Hypermetabolism and alterations in blood flow during SE in the lithium-pilocarpine adult rat model occur primarily in the regions that suffer the most significant neuronal damage (the cortex, anterior olfactory nuclei, all amygdaloid and hippocampal regions, lateral septum, thalamic nuclei and substantia nigra)(44, 192-194). Previously, increased VCAM-1 expression has been observed with immunohistochemistry at 24 h following pilocarpine induced SE and remained upregulated at 30 d(123). This is consistent with our data which demonstrate that there is significant upregulation of VCAM-1 at 22 h post SE.

Evidence for regional expression of VCAM-1 is supported by *in vitro* studies which have shown that seizure activity alone can cause increased expression of adhesion molecules without the need for systemic effects(195). It has been previously shown in the pilocarpine model that COX-2 is upregulated primarily in the hippocampus and piriform cortex whilst expression of other mediators such as Toll-like receptor 2 (TLR2) and TNF-α have been found to be more global(196). In the focal kainate model, inflammatory markers such as upregulation of ICAM-1, microglia activation and BBB disruption occur primarily in the ipsilateral (kainic acid injected) hippocampus(197) This suggests that, seizure activity leads to the regional expression of inflammatory markers. The cause of this regional expression is likely to be complex and several factors might be involved, including seizure induced release of high-mobility group box protein 1(69), necrosis, apoptosis and/or ischemia.

MRI T_2 changes have been observed as early as 6 h following SE in the severely affected piriform and entorhinal cortices(198). Hyperintensities in the hippocampus are generally observed at a slightly later time point, with T_2 measurements peaking at about 48 h following SE in rodents(44, 183) and within 48 h in humans(199). It has also been shown that T_2 is predictive of neuronal injury following SE(200). However in the current study we observed no significant increase in T_2 in the hippocampus at 22 h following SE, yet marked binding of the targeted contrast agent. This suggests that imaging inflammation using targeted iron oxide contrast agents could provide an

early and more sensitive marker of brain injury. There is currently no validated biomarker that predicts the development of epilepsy(201) and a molecular imaging approach, such as reported here, could be used for this purpose.

The intra-vascular nature of the contrast agent used in this study may mean that iron oxide induced contrast is dependent on the blood vessel density within voxels, which is a possible limitation. Furthermore, distinguishing between hypointensities caused by tissue interfaces and those caused by iron oxide based contrast agents is problematic based on automated segmentation algorithms.

Recently it has been hypothesised that the post-seizure inflammatory processes in these regions could contribute to both cell death and hyperexcitability(202). Studies in epilepsy patients have indicated increased numbers of leukocytes in the brain parenchyma compared to controls(123). However current therapeutic strategies are only targeted towards treating neuronal excitability using anti-epileptic drugs that do not treat the possible detrimental effects of the inflammatory component of the condition, which could lead to both seizure activity and neuronal degeneration. Imaging inflammation in epilepsy patients using targeted iron oxide contrast agents could therefore help determine which subtypes of patients might benefit from anti-inflammatory therapies.

5.6 Conclusions

The precise role of neuroinflammation in the progression of SE associated injury is unknown. There is therefore a need for more specific imaging markers of inflammation. In this study we have demonstrated *in vivo* imaging of acute inflammation following lithium-pilocarpine induced status epilepticus. Imaging markers of inflammation in models of epilepsy could enable pharmacological modulation and may therefore be used to determine the role of inflammation in epileptogenesis and neuronal injury. Furthermore, imaging of inflammation in clinic could help determine which patients might benefit from anti-inflammatory therapy.

Chapter 6 Anti-Inflammatory Therapies for Neuroprotection following Status Epilepticus

6.1 Aims

The previous two chapters have outlined the development of a molecular imaging technique that will enable the monitoring of inflammation following status epilepticus. In this chapter, it is hypothesised that the aforementioned method could be used as a biomarker for monitoring anti-inflammatory therapies. The potential for these drugs to offer neuroprotection following SE is also assessed. The primary hypotheses for the work outlined in this chapter are:

- The corticosteroid – dexamethasone is able to modulate VCAM-1 expression and this can be monitored by using the molecular imaging approach described in Chapter 5 (part I).
- Dexamethasone administered following prolonged seizures alleviates the progressive brain injury caused by SE and this can be measured by using volumetric MRI (part II).
- Voxel-based analysis methods, such as statistical parametric mapping and voxel-based morphometry can be used alongside the region-based methods for monitoring anti-inflammatory therapies (part III).

6.2 Dexamethasone

Dexamethasone was chosen for its broad-spectrum anti-inflammatory effects, because it is inexpensive compared to antibody-based therapies and is widely used in clinic for alleviating vasogenic oedema. It is frequently used for patients with primary and secondary brain tumours as well as to treat allergic reactions. For this reason it is more clinically translatable than experimental therapies that are not yet approved by the regulatory authorities. Its mechanisms of action were described in section 1.8.7. Briefly, DEX supresses NF-κB transcription and therefore has the capacity to reduce the expression of cell adhesion molecules such as VCAM-1.

6.3 Part I: Modulation of the VCAM-1 Biomarker

The aims of this pilot study were to test whether dexamethasone can be used to modulate VCAM-1 expression following SE and to determine whether the previously characterised MRI contrast agent can monitor these changes in expression.

6.3.1 Materials and Methods

Status epilepticus was induced in 4 adult male Sprague-Dawley rats as described in 5.3.1. 2 rats were included as control subjects and underwent the same injections as the $Control_{VCAM}$ group in Figure 24. Approximately 1 h following status epilepticus, 2 rats received injections of dexamethasone sodium phosphate (10 mg/kg) (SE-DEX). 24 hours later, MRI using the VCAM-MPIO contrast agent was performed as described in sections 4.4.6 and image analysis was implemented as described in section 4.4.10.

6.3.2 Results

Initially, attempts were made to quantify VCAM-1 expression using western blotting. However, western blotting failed under denaturing conditions (i.e. conditions that do not preserve the tertiary structure of the protein). Some banding was seen in western blots done under non-denaturing conditions (data not shown), suggesting the primary antibodies used in this application require the tertiary structure of the protein to be intact. However, this did not prove to be suitable for quantitation.

The aim of this pilot study were to test whether dexamethasone can be used to modulate VCAM-1 expression following SE. Although the number of subjects in the study was small, there was no suggestion that contrast agent binding was reduced in subjects treated with the drug. This can be seen in Figure 28b,c, in which it is evident that there are large amounts of iron oxide present in the hippocampus in rats treated with DEX and there does not look to be a significant reduction in VCAM-1 expression. The imaging in one of the SE subjects was started 1 hour later than the other imaging sessions due to issues relating to the acquisition software, which explains the reduction in CA binding in this subject (Figure 28b, lower panel). Nevertheless, the results conclusively show a significant amount of CA binding in hippocampus of SE-DEX rats. Quantitation across the whole brain is shown in

Figure 29, but does not appear to reflect well the degree of contrast agent binding within the cortex and hippocampus.

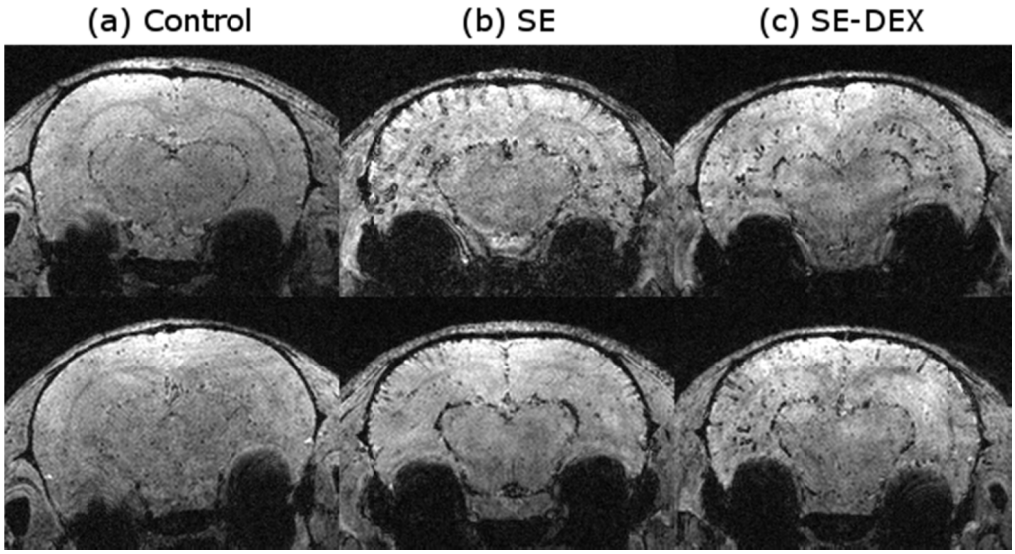

Figure 28: 3D gradient-echo images following administration of VCAM-MPIO. (a) Control subjects that did not undergo SE. (b) 24 h following SE. (c) Subjects treated with dexamethasone sodium phosphate (10 mg/kg) 1 h after SE. (n=2 per group).

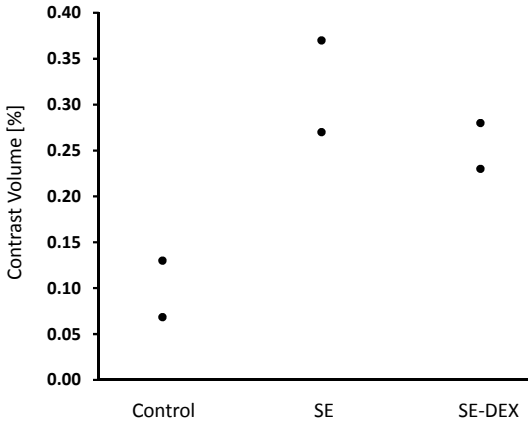

Figure 29: Contrast volume over the entire brain following administration of VCAM-MPIO in rats treated with dexamethasone compared to the SE and control groups. Rats treated with 10 mg/kg dexamethasone sodium phosphate (SE-DEX), compared to the untreated SE and Control groups. (n=2 per group).

6.4 Part II: Investigation into the Effects of Dexamethasone on Brain Injury

The result that DEX did not appear to reduce VCAM-1 expression was surprising. Experiments were therefore designed in order to utilise structural MRI and T_2

relaxometry to investigate whether DEX is neuroprotective when administered following SE. In this study, T_2 relaxometry was used as a marker of brain oedema. For T_2 measurements, rats were imaged at 2 and 4 days following SE. High resolution structural imaging was performed 3 weeks after SE in order to determine the effect of DEX on later brain injury. The primary hypothesis in this study is that dexamethasone reduces hippocampal injury as determined by volumetric imaging. The secondary hypothesis is that DEX is able to reduce the acute cerebral oedema that occurs at 2 days after SE as monitored by T_2 relaxometry.

6.5 Materials and Methods:

6.5.1 Animal Model:

All animal procedures were carried out in accordance with the UK Animals (Scientific Procedures) 1986 Act and institutional ethics regulations.

6.5.2 Experiment 1:

Unless otherwise stated, all chemicals were obtained from Sigma-Aldrich, UK. Male Sprague-Dawley rats (170-210 g) were obtained from Charles River Laboratories (Margate, UK) (n=42) and were kept under controlled environmental conditions including a 12 h light-dark cycle and the provision of with food and water ad libitum. SE was induced as described in section 5.3.1. Saline was administered in control animals in place of pilocarpine (n=4). Seizure severity was assessed every 10 min using the Racine scale (section 1.5.6). Diazepam (10 mg/kg, i.p.) was administered 90 min following SE onset in order to terminate the seizure. Additional diazepam (10 mg/kg) was administered 30-40 min later. Following status epilepticus, rats were randomly assigned to one of two groups: SE-DEX10 rats (n=13) received dexamethasone sodium phosphate (10 mg/kg, equivalent to 7.6 mg/kg dexamethasone) immediately following status epilepticus and at 24 h (10 mg/kg) following SE. This dose is comparable to doses that have shown or attempted to demonstrate efficacy in other rat models of brain oedema(117, 203-206). SE rats (n=15) received saline injections in place of dexamethasone. Dexamethasone is known to have a diuretic effect(207), therefore SE-DEX10 and SE animals received subcutaneous saline and saline/glucose solution for the first few days following SE.

6.5.3 Experiment 2:

As a high mortality rate was observed in the SE-DEX10 group, the experiment was repeated using the same protocol except a single dose of dexamethasone sodium phosphate (2 mg/kg) was administered i.p. at 1 h following SE (n=16). Following SE rats were randomly assigned to one of two groups: SE (n=6) and SE-DEX2 (n=6).

6.5.4 Magnetic Resonance Imaging

MRI relaxometry was performed at 48 h and 96 h following SE. A subset of animals in experiment 1 were scanned prior to SE induction (n=17) and all of these rats were included in the analysis. High resolution structural imaging was conducted between 18 and 20 d following SE. All imaging was carried out using the 9.4T MRI setup described in section 4.4.6. Animals were anesthetised with 4% isoflurane and maintained at 1.5-2% isoflurane in pure oxygen (1 L/min) throughout the imaging session. Temperature was maintained at 37±0.5°C using an air and water tubing warming system. T_2 measurements were performed across 15 contiguous slices using a 2D multi-echo spin-echo sequence using the following parameters: TR=2.5 s, FOV=25×25 mm, slice thickness=1 mm, matrix=128 x 128 and TE=8, 16, 24, 32, 40, 48, 56, 64, 72, 80, 88, 96, 104, 112, 120 ms. T_2-weighted high resolution structural imaging was done using a 3-dimensional fast spin-echo (FSE) sequence at 150 µm isotropic resolution (TR=1.8 s, FOV=24×24×24 mm, matrix=160×160×160, TE_{eff}=41.8 ms, ETL=16, acquisition time=48 min).

6.6 Data Analysis

6.6.1 Quantitative T_2

Regions of interest were identified by coregistration of the multi-echo images to a rat brain MRI template(208). This was performed in SPM 8 (UCL Wellcome Trust Centre for Neuroimaging, http://www.fil.ion.ucl.ac.uk/spm) using a 12 parameter affine registration with normalized mutual information as the cost function**.** Following coregistration, the transformation matrix was used to transform the regions of interest (ROIs) to the image space. Regions of interest included right and left somatosensory cortices, anterior dorsal hippocampus, caudate putamen, cingulate cortices, piriform cortices and the thalamus. Automated segmentation of the rat brain

was achieved by rigid coregistration to a rat brain template. The accuracy of the segmentation was verified visually and is shown in Figure 30. Quantitative T_2 measurements were performed by calculating power images (section 3.4). Odd echoes were omitted from the analysis in order to reduce errors caused by imperfect refocusing of magnetisation.

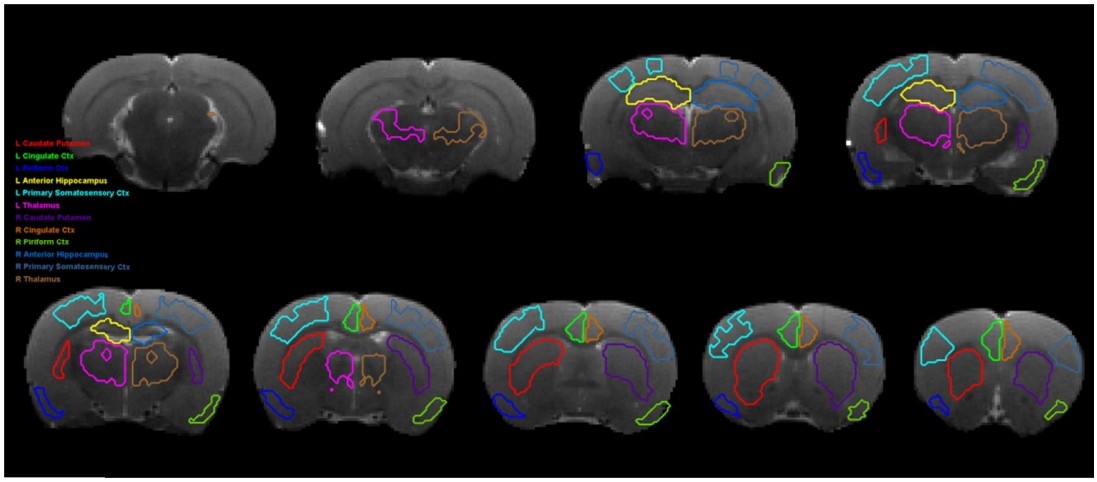

Figure 30: Example of automated segmentation of the multi-echo images used for quantitative T_2 measurements.

6.6.2 Volumetric measurements

The data was firstly zero filled to 256×256×256 and then Tukey filtered in k-space to reduce Gibbs ringing artifacts. Bias-field correction was conducted using N4ITK(149). Following this, intensity normalisation was performed as described in section 3.9. Whole brain and hippocampal volume measurements were both performed automatically using a multi-atlas approach. Whole-brain volume measurements were carried out using 6 previously acquired manually masked 3-dimensional FSE datasets as atlases. These were co-registered to the target images using a block-matching affine registration algorithm(160, 209, 210). Label fusion was achieved by majority voting, which involves assigning each voxel the label that the majority of the candidate segmentations agree on(164). Hippocampal volume measurements were performed using the multi-atlas approach with optimised label fusion parameters, as described in section 3.12. Relative hippocampal volume (rHCV) was calculated by dividing the hippocampal volume by the total brain volume.

6.6.3 Statistical Analysis

The statistical analysis in this study was performed by Dr Kwok Pan Chun of the School of Environment and Sustainability, University of Saskatchewan, Canada. Unless otherwise stated, statistical analysis between groups was performed using one-way ANOVA and unpaired t-tests with unequal variance in the R software package (http://www.r-project.org, version 3.1-109.). Mortality between groups was tested using the test of equal proportions in R. In order to account for correlation between variables, T_2 was compared across all regions by means of a linear-mixed effects model using the lme4 package in the R environment(211). For all linear-mixed effects models, rats were considered to be random effects, whereas treatment groups, weights, study date and mortality were considered to be possible fixed effects (i.e. explanatory variables). In a stepwise mixed effects model framework, an initial model starting with T_2 across all brain regions is used to identify significant regions as the explanatory variables for hippocampal volume. Box and whisker plots show the median, and first and third quartiles. The whiskers are drawn from the first and third quartiles to the most extreme point not considered outliers. Outliers are considered to be more than 1.5 interquartile ranges from either the first or third quartile and are marked with a plus sign. Averages are expressed as the mean±SEM. Statistical significance was assigned at $p<0.05$.

6.7 Results

The aims of experiment 1 were to test the effects of dexamethasone given following SE at a dose of 10 mg/kg on T_2 and hippocampal volume. Surprisingly, the results from experiment 1 suggested that dexamethasone at 10 mg/kg had a detrimental effect on both survival during the first week after SE and brain injury at 3 weeks. For this reason, experiment 1 was repeated using a lower dose of 2 mg/kg DEX.

6.7.1 Animal Model

All of the rats that were administered pilocarpine progressed to status epilepticus. None of the animals in the control group exhibited any behavioral change. 14 out of 54 (26%) animals died during or immediately after SE and were therefore excluded from the study. There was no difference between the three groups: SE, SE-DEX2 and

SE-DEX10 in regards to latency to SE onset (Figure 31a). Furthermore, there was no difference in seizure severity according to the behavioural scoring (Figure 31b). All rats were scored throughout each 10 minute time period. During the later stages of status epilepticus almost all rats reached stage 5 on the Racine scale, during which time seizure severity alternated between stages 3 and 5. Behavioural scoring after 80 minutes was 4.3, 4.8 and 4.3 for SE, SE-DEX2 and SE-DEX10 respectively. The two doses of diazepam were effective at terminating SE in all rats and no overt signs of sustained seizures could be observed within the following 24 h. Dexamethasone or saline was administered at 1 h following diazepam injection, at this time point, rats were lethargic but there were no signs of on-going seizure-like activity.

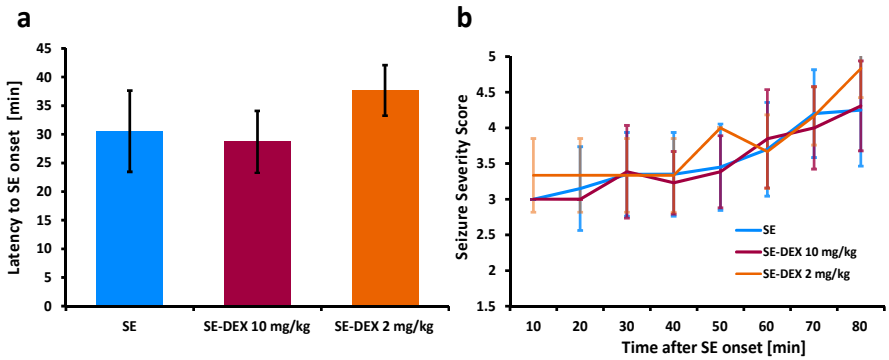

Figure 31: Behavioural assessment of status epilepticus in SE and SE-DEX rats. (a): Latency to onset of status epilepticus. (b): Behavioural assessment of seizure severity throughout status epilepticus. (a) and (b) SE (n=21), SE-DEX 10 mg/kg (n=13) SE-DEX 2 mg/kg (n=6). Data is displayed as mean±SD.

6.7.2 Mortality

Within the first week after SE, 3 of 21 subjects died in the SE group, 2 of 6 in the SE-DEX2 group and 6 of 13 in the SE-DEX10 group. The proportion of rats that died within the week following status epilepticus was therefore 0.14, 0.33 and 0.46 for SE, SE-DEX2 and SE-DEX10 respectively. The animals that died after the 2 and 4 day imaging time points were included in the analysis. Although these proportions were not significantly different ($p = 0.11$), these data indicate that dexamethasone may exacerbate mortality associated with status epilepticus.

6.7.3 Time Course of T_2 alterations

T_2 is elevated at 48 h in SE rats compared to CTL in the hippocampus (52.1 ms *vs.* 45.6 ms, p=0.008, Figure 32a) and piriform cortex (69.5 ms *vs.* 51.0 ms, $p=5x10^{-7}$, Figure 32b). These alterations began to normalize by 96 h. This marked bilateral hippocampal oedema is shown in Figure 33b. 4 animals in this study exhibited marked unilateral oedema in the neocortex (Figure 33b) that was not present in controls (Figure 33a). These can be seen as outliers in Figure 32e,f. MRI performed at 3 weeks following the initial insult (Figure 33d) exhibits significant atrophy of the hippocampus leading to enlargement of the lateral ventricles. Hypointense regions in the CA1, CA3 and dentate gyrus of the hippocampus are evident (Figure 33d). Hyperintense regions at the three week time point in the right neocortex (Figure 33d) correspond to the regions of hyperintensity that occurred at 48 h following SE (Figure 33b).

6.7.4 Effect of Dexamethasone on Acute Cerebral Oedema

One of the aims of this study was to test whether dexamethasone alleviates the regional T_2 caused by status epilepticus in the hippocampus and piriform cortex. The mean T_2 relaxation time at 2 days in the hippocampus was: 45.6 ms, 52.1 ms, 55.3 ms, 55.0 ms for CTL, SE, SE-DEX10 and SE-DEX2 respectively (Figure 32a). In the piriform cortex, T_2 at 2 days was: 51.0 ms, 69.5 ms, 74.3 ms and 75.2 ms for CTL, SE, SE-DEX10 and SE-DEX2 respectively (Figure 32b). The SE-DEX10 group had significantly higher T_2 in the piriform cortex than SE at 2 days and 4 days (p=0.01, p=0.04 respectively).

A linear mixed-effects model was also used to compare all 12 brain regions together in the treatment groups to the CTL group in order to account for other possible within-sample effects and repeated measures. SE-DEX10 was significantly different to CTL at day 2 and day 4 (p=0.004 and 0.03), DEX2 was significantly different to CTL on day 2 (p=0.01) but not day 4 and SE was not significantly different from the CTL group at either time point.

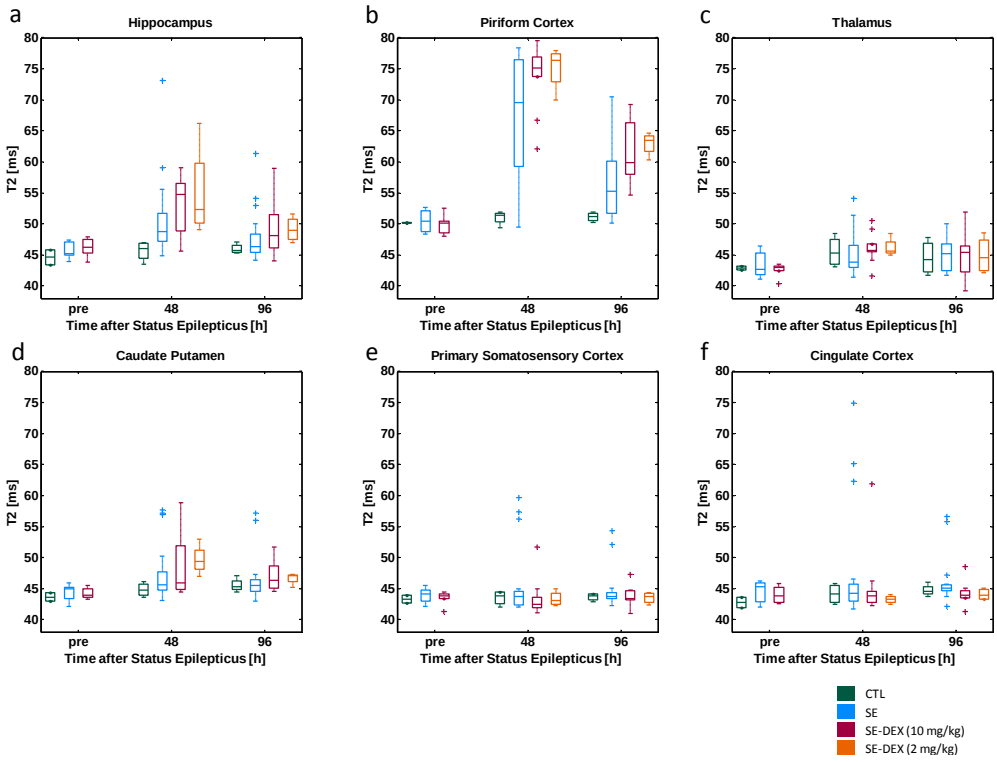

Figure 32: T_2 relaxation times measured pre, 48 h and 96 h following lithium-pilocarpine induced status epilepticus. (a) Hippocampus, (b) Piriform Cortex, (c) Thalamus, (d) Caudate Putamen, (e) Primary Somatosensory Cortex, (f) Cingulate Cortex. Treatment groups: CTL (n=4), SE (n=20), SE-DEX10 (n=10), SE-DEX2 (n=4).

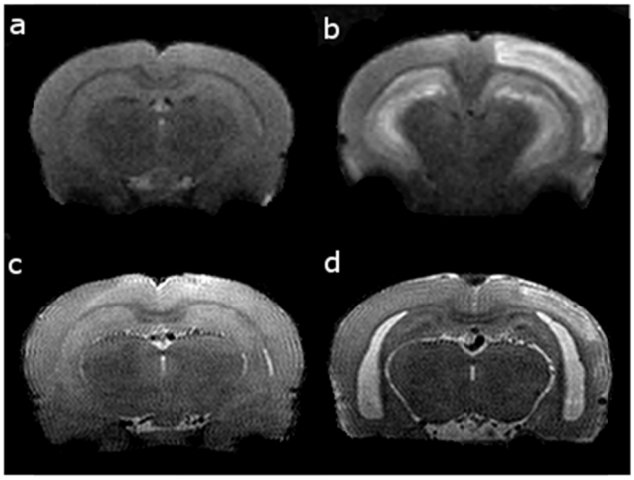

Figure 33: T_2 weighted MRI images in rats that have undergone status epilepticus compared to controls. The first column shows coronal MRI images from a CTL rat and the second is from a rat that underwent status epilepticus. (a) and (b): Low resolution images acquired at 48 h following administration of saline or pilocarpine respectively. (c) and (d): High resolution images acquired 3 weeks after pilocarpine or saline respectively. (b) Illustrates marked bilateral oedema in the hippocampus and unilateral oedema in the neocortex. (d) Shows significant atrophy of the hippocampus leading to enlargement of the lateral ventricles. Hypointense regions in the CA1,CA3 and dentate gyrus of the hippocampus are evident and hyperintense regions in the right neocortex correspond to the regions of hyperintensity that occurred at 2 days following SE.

6.7.5 Effect of Dexamethasone on Relative Hippocampal Volume and Total Brain Volume

Accurate segmentation of the hippocampus was achieved in MRI images of both controls and post-status epilepticus rats (Figure 34c,d) using a multi-atlas approach. At 3 weeks following status epilepticus, rHCV was significantly different among groups (Figure 34b, p=0.01). SE rats had significantly lower relative hippocampal volume compared to CTL (p=0.001). SE-DEX10 had significantly lower rHCV compared to SE (p=0.003). There was no significant difference between SE-DEX2 and SE. Total brain volumes were 2612.8±40.4 mm^3, 2565±12.3 mm^3, 2487.7±11.7 mm^3 and 2521.9±12.18 mm^3 for CTL, SE, SE-DEX10 and SE-DEX2 respectively (Figure 34a). DEX appeared to be detrimental to total brain volume, however brain volumes across all groups were not significantly different (p=0.09). There was no significant difference in weight change over three weeks between any of the groups (SE, SE-DEX10 and SE-DEX2) (p=0.25).

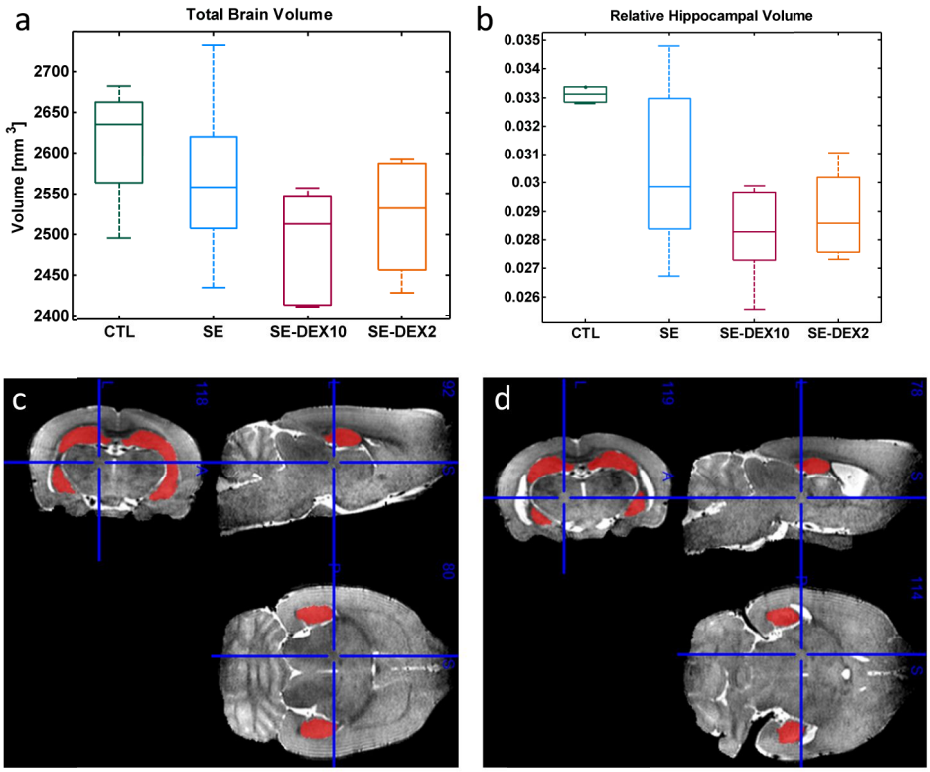

Figure 34: Total brain volume and relative hippocampal volume at 3 weeks after status epilepticus in rats treated with dexamethasone. (a) Total brain volume *vs.* treatment group. (b) Relative hippocampal volume *vs.* treatment group. (c) Example image showing automated segmentation of the hippocampus in a control rat. (d) Example image demonstrating automated segmentation of the hippocampus in a post-status epilepticus rat, 3 weeks after the initial insult. Treatment groups: CTL (n=4), SE (n=16), SE-DEX10 (n=5), SE-DEX2 (n=4).

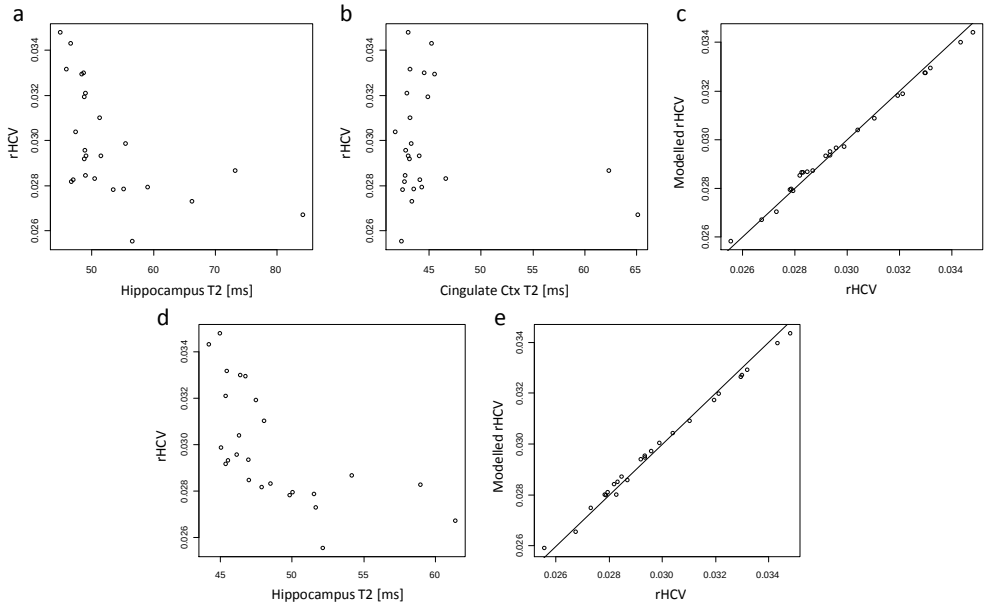

Figure 35: Scatter plots showing the relationship between early T_2 measurements and relative hippocampal volume measured 3 weeks after SE. (a) and (b): Hippocampus and cingulate cortex T_2 measured 2 days after SE *vs.* rHCV. (c) rHCV *vs.* rHCV modelled using a linear mixed-effects model for the data shown in (a) and (b). (d) Hippocampus T_2 measured 4 days after SE *vs.* rHCV. (e) rHCV *vs.* rHCV modelled using a linear mixed-effects model for the data shown in (d).

6.7.6 Relationship between T_2 and Hippocampal Volume

According to the linear mixed-effects model and considering all animals that underwent status epilepticus, T_2 in the hippocampus and the cingulate cortex at 2 d following status epilepticus is predictive of relative hippocampal volume at 3 weeks (Figure 35a,b) (β_1=-0.00030±0.00007, 0.00031±0.0001, p=0.0004 and p=0.01 respectively). T_2 at 4 d following status epilepticus in the hippocampus is predictive of relative hippocampal volume (Figure 35d) (β_1=-0.00035±0.00009, p=0.0007).

6.8 Discussion

The main findings from this study are that administering dexamethasone following lithium-pilocarpine induced status epilepticus regionally intensifies acute T_2 alterations at 2 days and 4 days following status epilepticus. Second, dexamethasone adversely affects the degree of hippocampal injury at 3 weeks following SE. Third, dexamethasone exacerbates the delayed mortality associated with status epilepticus.

These findings apply even at doses of dexamethasone sodium phosphate as low as 2 mg/kg. Importantly, T_2 relaxation times in the hippocampus were found to be predictive of later hippocampal injury. Lastly, this study demonstrates that quantitative T_2 measurements and volumetric measurements in the rat can be performed using automated methods that require no user intervention.

Previous studies have shown the T_2 alterations following status epilepticus in the rat peak at around 2 d following SE(44, 212), and this is confirmed in the current study. Our previous work demonstrates that although there are significant changes in T_2 in the piriform cortices at 1 d following SE, T_2 alterations in the hippocampus appear to not be evident until 2 d following SE. Alterations in T_2 occurring at this late time point after SE could suggest that vasogenic oedema rather than cytotoxic oedema is the primary cause of abnormalities throughout the hippocampus(213, 214). The finding that T_2 correlates with later hippocampal volume suggests that T_2 might be a useful biomarker for monitoring anti-inflammatory therapeutic interventions. The current study supports a previous study revealing that T_2 in the hippocampus at 2 days is predictive of later hippocampal volume(44).

This study has demonstrated that the acute T_2 alterations that occur following lithium-pilocarpine induced status epilepticus are exacerbated by DEX in the regions already affected by SE. The design of the current study did not enable us to determine whether these effects are due to side-effects of the drug such as dehydration, alterations in plasma osmolality or blood pressure effects. No relationship was found between treatment groups and the differences in body weight between pre-SE and any of the subsequent days, suggesting that dehydration was not the cause of the observed outcomes. It is also worth noting that the diuretic effect of DEX in conjunction with its anti-inflammatory effect should help to alleviate vasogenic oedema(207).

Unpredictably, a trend towards increased delayed mortality rate was observed in rats treated with dexamethasone. The mechanisms behind delayed mortality following status epilepticus are unknown. It has been speculated that it could be caused by recurrent seizures(215). Vasogenic oedema is well known to contribute to death in neurological disorders, therefore the increase in mortality in DEX treated rats compared to the SE group could be attributable to increased brain oedema.

Several possible explanations exist for the results observed. First, these data could suggest that some early inflammatory processes may provide a protective effect, which is not inconceivable given that there is an extremely fine balance between the beneficial and detrimental effects of neuroinflammation(113, 216). Also notable is that pre-treatment with COX-2 inhibitors has been observed to lead to increased mortality both in electrically induced status epilepticus and in the kainate model(217, 218). This effect was likely due to aggravation of seizure activity, which is unlikely to be the case in the current study given that previous data indicates that dexamethasone suppresses pilocarpine induced SE(118). Further supporting the hypothesis that early inflammation is protective, is a study which showed that Interleukin-6 knockout mice exhibit reduced astrogliosis compared to wildtypes following kainate induced seizures and this was accompanied by dramatically intensified neuronal degeneration in the hippocampus(219). It is also noteworthy that randomised controlled trials of anti-inflammatory therapies in patients with stroke or traumatic brain injury (TBI) have observed an increase in mortality rate in patients administered anti-inflammatory drugs compared to those given a placebo(220, 221). One possible explanation for the worse outcome in TBI patients treated with corticosteroids is that steroids have recently been shown to worsen cerebral oedema under acidotic conditions in the rat(206). It is also likely that certain aspects of the inflammatory process are protective whilst others are harmful. Further research is required to explore this hypothesis.

An alternative explanation is that DEX could elicit a pro-inflammatory response. It has been shown that glucocorticoids can exhibit pro-inflammatory effects under certain conditions, e.g. chronic stress(222). Furthermore, corticosterone treatment has been shown to exacerbate kainic acid induced neurotoxicity in the CA3 region of the hippocampus and concomitantly increase the number of immunoreactive cells(223). Given that the current study also reports a cerebral insult that is excitotoxic in nature, possible pro-inflammatory effects of DEX might contribute to exacerbated brain injury in DEX treated rats compared to saline treated rats.

Finally this study has demonstrated that automated methods of data analysis are effective tools that can be employed in epilepsy research to reduce the laboriousness of manual region drawing and therefore can be used in conjunction with

histopathology to test the neuroprotective efficacy of new experimental treatments. This is a noteworthy development as to our knowledge all other studies that have attempted to measure hippocampal volumes in disease models have employed manual segmentation.

6.9 Part III: Investigation into the Effects of Ethyl Pyruvate on Brain Injury using Statistical Parametric Mapping

The result that dexamethasone exacerbated brain injury was surprising. For this reason a different anti-inflammatory drug, ethyl pyruvate (EP) was tested. The justification for using this compound was based on a previous study that demonstrated EP to have noteworthy neuroprotective effects after kainic acid induced seizures in mice(224). These protective effects were accompanied by a reduction in microglial activation and remarkably they still occurred even when EP was administered as late as 12 h after the insult. Suppression of microglial activation and strong protective effects were also observed after ischemia-reperfusion injury and effects were evident when EP was administered up to 24 h after the ischemic insult(225). The reason for such late-acting effects is thought to be because EP prevents the release of HMGB1, which as a late pro-inflammatory cytokine is released only after a delay of around 12-18 h(226).

6.9.1 Aims

The design of this study is similar to the study design reported in the previous part. The only differences are that relaxometry was only conducted at 48 h after the insult and the later imaging time point was chosen to be approximately 2 weeks after SE. The primary aim of this study is to test whether or not EP is effective at reducing brain injury following SE. The secondary aim is to improve upon the imaging techniques that are reported in part II. The secondary hypotheses in this study are:

- Voxel-wise statistical analyses (statistical parametric mapping (section 3.13)) should be used alongside region-based analyses for quantitative T_2 measurements.
- Neuronal injury is not confined to the hippocampus after SE, therefore voxel-based morphometry can be used to detect these more widespread changes.

- Hippocampal volume measurements can also be achieved by the group-wise registration afforded by VBM.
- 2D pulse sequences might be preferable to 3D sequences due to the greater contrast that they afford (section 2.6).

6.10 Materials and Methods

6.10.1 Animal Model

All procedures and protocols were performed in agreement with the policies established by the "*Animal Care Committee*" at Tohoku University, Sendai, Japan. Status epilepticus was induced as described in section 5.3.1. 1 h after diazepam administration, rats were randomly assigned to 1 of 2 groups, SE-EP (n=6) or SE (n=6). Subjects in the EP group received 100 mg/kg ethyl pyruvate (28 mM) in a calcium containing balanced salt solution made up of 130 mM sodium chloride, 4 mM KCl and 2.7 mM $CaCl_2$ and the SE group received vehicle. The control group (n=4) received saline in place of pilocarpine.

6.10.2 *In vivo* MRI

MRI was performed using a 7 T Bruker PharmaScan system (Bruker Biospin, Ettlingen, Germany) and a 38 mm diameter bird-cage receive/transmit coil.

6.10.3 Relaxometry

T_2 relaxometry was performed at 2 days after SE. Rats were anaesthetised with 4% isoflurane in a 6:4 mixture of nitrogen and oxygen and were maintained on 1.5% isoflurane throughout the imaging protocol. A multi-echo spin-echo sequence was used with the imaging parameters: TR=3560 ms, TE=10.5, 21, 31.5, 42.1, 52.6, 63.1, 73.6, 84.2, 94.7, 105.2, 115.7, 126.3 ms, NEX=2, matrix=192×144, FOV=30×30 mm^2, slice thickness=1 mm, number of slices=25. T_2 maps were calculated using the same curve fitting method outlined in section 6.6.1.

6.10.4 Volumetric MRI

High resolution 2D FSE imaging was performed 2 weeks after SE using the following parameters: TR=4286 ms, TE_{eff}=30 ms, ETL=4, NEX=8, matrix=256×256,

FOV=32×32 mm^2, slice thickness=0.6 mm, number of slices=50). The experimental setup is described in section 7.9.2. Hippocampal volumes and total brain volumes were measured using the methods described in sections 3.12 and 6.6.2 respectively.

6.10.5 Statistical Parametric Mapping

As noted in section 3.13, spatial normalisation can be used instead of atlas-based segmentation. In this manner, statistics can be performed on a voxel-by-voxel basis without prior hypotheses regarding the affected regions. All statistical parametric mapping processing was done using SPM 8. First, (for the relaxometry data) a mean volume was calculated by averaging across all echo times and this was segmented into grey matter, white matter and CSF using probabilistic tissue priors (227), next these binary images were spatially normalised using DARTEL (see section 3.13). Following this, the T_2 maps were spatially normalised by applying the corresponding transformation matrix and deformation field. The normalised T_2 maps were then smoothed using a Gaussian filter with 0.5 mm FWHM prior to performing voxel-wise t-tests. Because of the low number of subjects in each group, images were displayed as $p<0.05$ (uncorrected for multiple comparisons) when comparing the CTL and SE groups and $p<0.01$ for comparisons between the SE-EP and SE groups.

6.10.6 Voxel-based Morphometry

In order to increase the statistical power in comparing between the SE and CTL group, an additional 4 CTL and 6 SE rats were imaged at the 2 week time point. VBM was performed by firstly interpolating the FSE images between slices to generate a final voxel size of 125×125×300 μm^3 and then by segmenting the images into grey matter, white matter and CSF using the SPM 8 Segment function and tissue priors generated from normal adult rats(227). After this, population specific tissue priors were generated using DARTEL. The images were then segmented again based on the new tissue priors and again coregistered using DARTEL. This approach, in which the segmentation procedure is performed using the population specific tissue priors, is referred to as ‘optimised VBM’(228) and was used as standard VBM failed to accurately segment the enlarged ventricles. Prior to statistical analysis, the spatially normalised grey matter probability maps were smoothed with a 0.5 mm FWHM Gaussian filter.

Hippocampal volumes were also measured by manually segmenting the population specific template. The deformation fields were inverted using DARTEL tools and the results were used to transform the label image to the space of the original images.

6.10.7 Statistical Analysis

Statistical Analysis was performed in MATLAB using one-way ANOVA and two-tailed t-tests assuming unequal variance. Statistical significance was assigned at $p<0.05$. Correlation was expressed using Pearson's product-moment correlation coefficient *r*. SPM 8 was used for voxel-wise t-tests. Voxel-wise false discovery rate (FDR) correction was used to control for multiple comparisons.

6.11 Results

6.11.1 Animal Model

All rats injected with pilocarpine progressed to status epilepticus. No rats died during status epilepticus. 2 rats in the SE-EP group and 1 rat in the SE group died during the first week after SE.

6.11.2 Relaxometry

In order to compare between the different groups, statistical parametric mapping was used. In this case, two sample t-tests were performed at each voxel in the brain to look for voxels which reached the significance level. The regions with significantly higher T_2 in SE subjects compared to controls can clearly be seen to be the piriform cortex, amygdala, entorhinal cortex, hippocampus as well as subregions of the thalamus and striatum (Figure 36). These regions agree well with those identified in the previous experiment (Figure 32). Using statistical parametric mapping in this case enables finer localisation of the affected regions. For instance, the CA1 region appears to be the most affected subregion of the hippocampus. One control subject was excluded from the analysis due to imaging artifacts. Unfortunately, this meant that the low numbers in this group led to low power in the statistical analysis. The mean T_2 in the cortex in the CTL group was 67.7±2.4 ms, which is considerably longer than T_2 values reported at 7T in the literature(229).

In order to determine the effects of EP on acute oedema, T_2 was tested on a voxel-wise basis between the SE-EP group and the SE group. No significantly different voxels were detected when testing the hypothesis that SE > SE-EP (Figure 37), signifying that there was no evidence that the drug reduced acute oedema. Significant voxels were detected when testing if SE-EP > SE (Figure 38), but these did not appear to be meaningful as they were not in the regions affected by SE and were likely to be due to errors in T_2 estimation, either because of the presence of stimulated-echoes or motion artifacts.

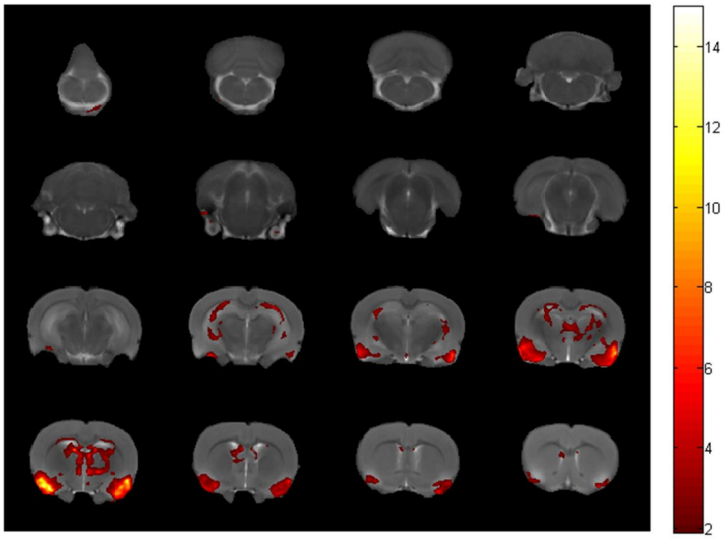

Figure 36: T-statistic maps of regions with higher T_2 in SE rats compared to controls. Controls (n=3), SE (n=6). P<0.05, uncorrected.

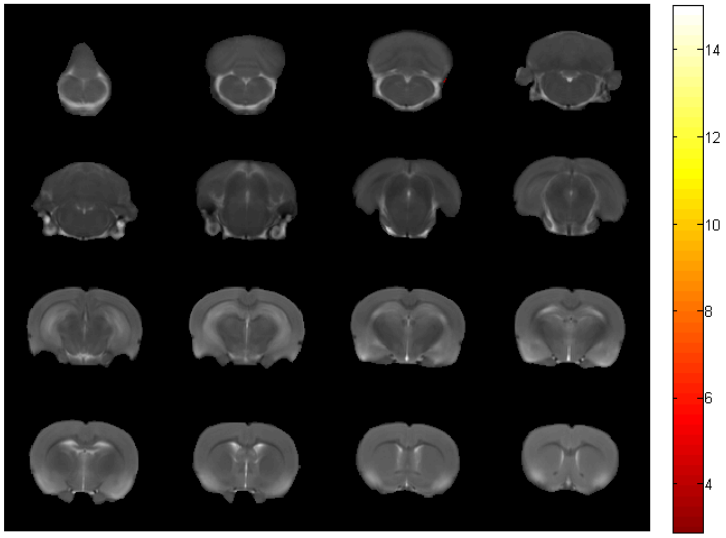

Figure 37: T-statistic maps of regions with higher T_2 in SE rats compared to SE-EP subjects. SE (n=6), SE-EP (n=6). P<0.01, uncorrected.

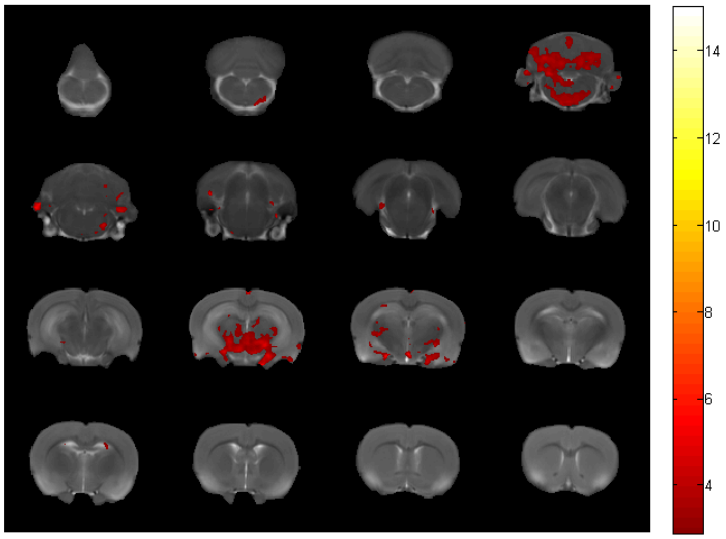

Figure 38: T-statistic maps of regions with higher T_2 in SE-EP rats compared to SE subjects. SE (n=6), SE-EP (n = 6). P<0.01, uncorrected.

6.11.3 Volumetric Measurements

There were no significant differences between the three groups in terms of body weight (p=0.77) or total brain volume (Figure 39a) (p=0.38). There was a significant difference in relative hippocampal volume between the groups (Figure 39b) (p=0.00009). SE and SE-EP groups were both different from controls (p=0.001 and

p=0.0001 respectively), but not significantly different to each other. Multi-atlas segmentation visually performed well on both controls (Figure 39c) and post-SE (Figure 39d) rats for delineation of the hippocampus.

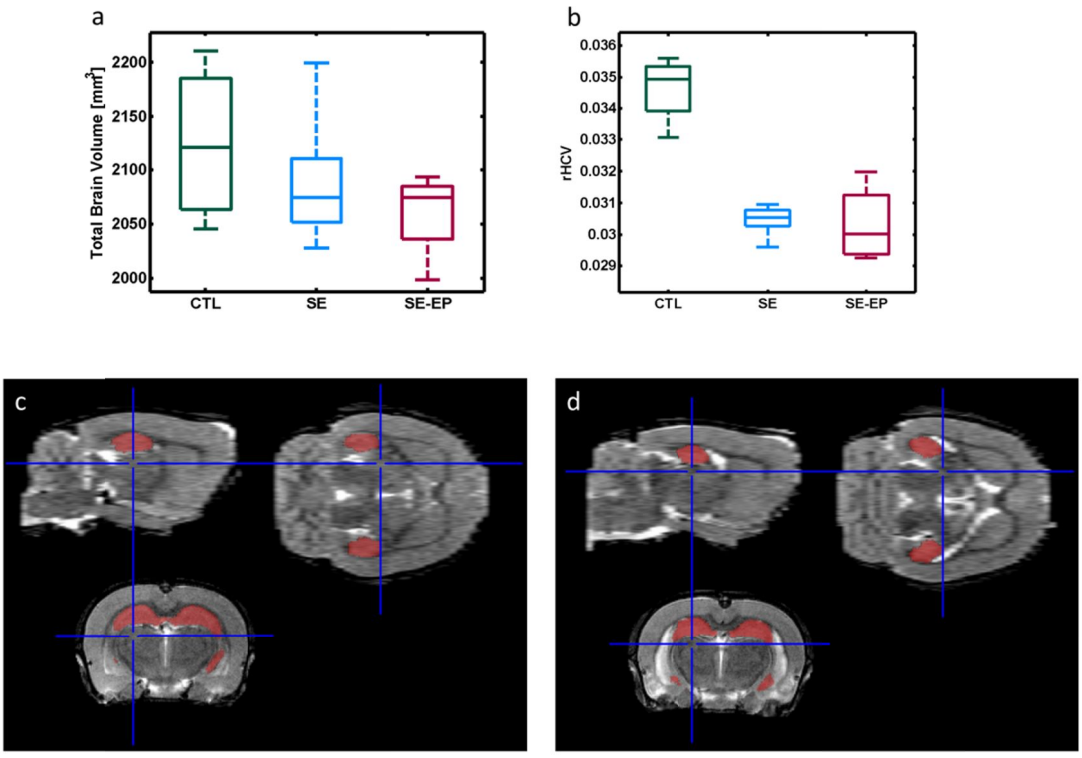

Figure 39: Total brain volume and relative hippocampal volume 2 weeks after status epilepticus in rats treated with ethyl pyruvate. (a) Treatment group *vs.* total brain volume. (b) Treatment group *vs.* relative hippocampal volume. (c) Example of automated segmentation of the hippocampus in a control subject. (d) Example of automated segmentation of the hippocampus in a rat that underwent status epilepticus. CTL (n=4), SE (n=5), SE-EP (n=4).

6.11.4 Voxel-based Morphometry

VBM is used to compare local differences in grey matter concentration (density) or grey matter volumes. In this study, the CTL and SE group sizes were extended to n=8 and n=11 respectively. VBM identified regional differences in grey matter density between the SE and CTL groups. The SE group had lower density across large regions of both the anterior and posterior hippocampus (Figure 40a). These were most obvious in the CA1 (light blue arrows) and CA3 (orange arrows) subregions. The piriform (white arrows) and entorhinal cortices (purple arrow) also

showed a significant loss in grey matter density. Small significant clusters were observed in the right somatomotor areas (grey arrow). Only small subregions of the thalamus displayed significant differences, for instance the ventral reuniens thalamic nucleus (yellow arrow). The ventral tenia tecta (dark blue arrow) and infralimbic cortex (dark green arrow) were affected as were the septum and regions surrounding the lateral ventricles (light green arrow). Figure 40b displays the t-statistic map thresholded with a value that corresponds to $p<0.01$, uncorrected for multiple comparisons and displays more widespread differences throughout the hippocampus, amygdala and neocortex.

Only two significant clusters survived FDR correction when comparing the hypothesis that the grey matter density for the SE-EP is greater than the SE group. These were in the hippocampus and neocortex but they only had a spatial extent of 3 and 4 voxels respectively. Because of their small cluster sizes and the low number of subjects in each treatment group, these results were unlikely to be meaningful.

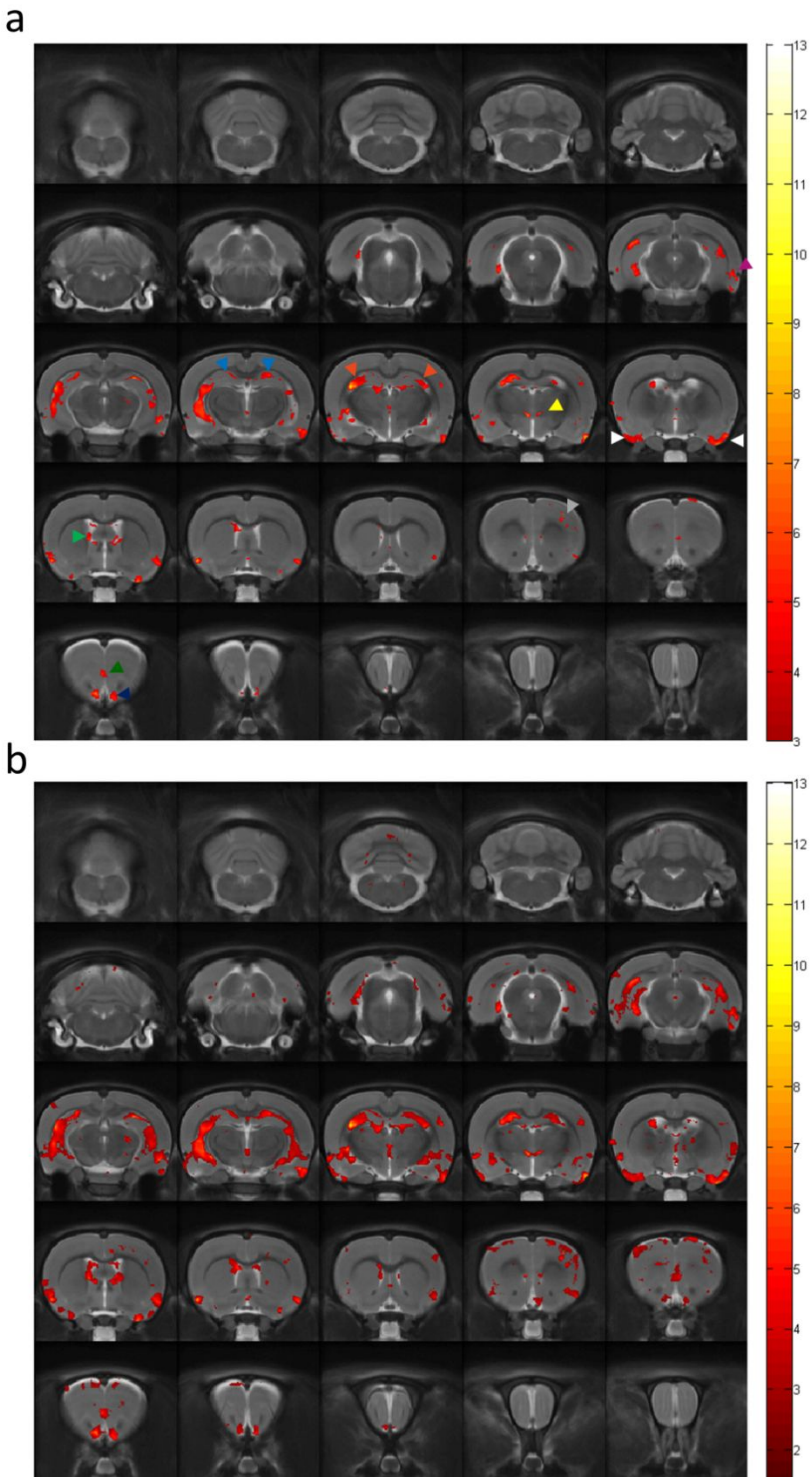

Figure 40: T-statistic map of significantly lower grey matter density in SE rats compared to controls, 2 weeks after SE. Arrow heads indicate anatomical locations: CA1 (light blue), CA3 (orange), entorhinal cortex (purple), piriform cortex (white), right somatomotor cortex (grey), ventral reuniens thalamic nucleus (yellow), ventral tenia tecta (dark blue), infralimbic cortex (dark green), septum (light green). T-statistic maps were overlaid on the normalised MRI template and were thresholded at (a) voxel-wise FDR <0.05 and extent cluster threshold>3 voxels and (b) p<0.01, uncorrected. CTL (n=8), SE (n=11).

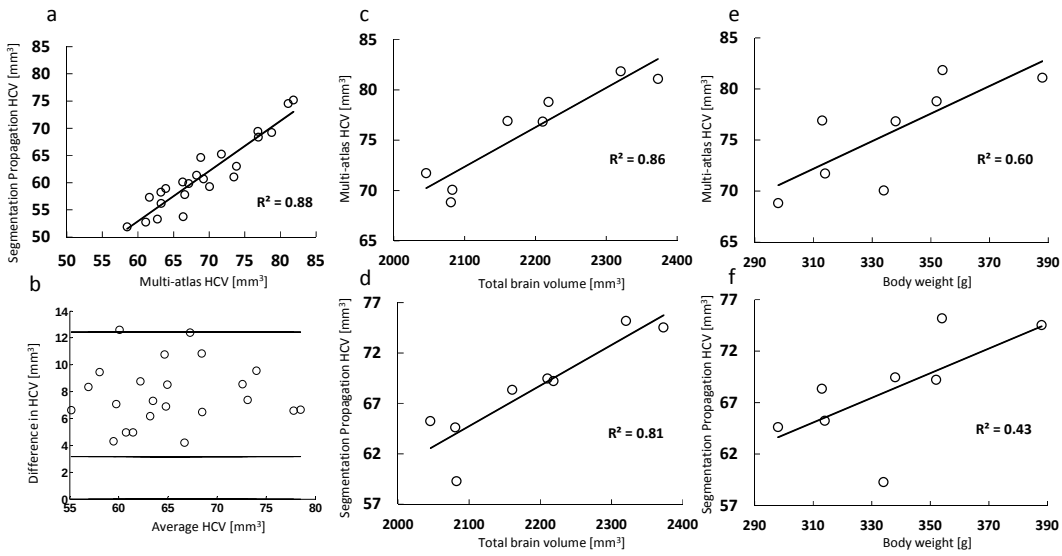

Figure 41: Agreement in hippocampal volume (HCV) measured by two different methods: multi-atlas segmentation and segmentation propagation. (a) Scatter plot showing the relationship between HCV measured via the two methods for all subjects (n=23). (b) Bland-Altman plot showing average of the two measurements plotted against the difference. Solid lines represent 1.96 standard deviations from the mean difference. (c)-(f) scatter plots only including control subjects (n=8). (c) Total brain volume (TBV) *vs.* multi-atlas HCV (d) TBV *vs.* segmentation propagation HCV. (e) Body weight *vs.* multi-atlas HCV. (f) Body weight *vs.* segmentation propagation HCV.

6.11.5 Agreement in Hippocampal Volume Measurements

Hippocampal volumes can also be measured by the semi-automated segmentation-propagation approach. This involves manually segmenting the group-wise template generated from the VBM analysis and then inverting the forward displacement fields. This inverse deformation was applied to the manually segmented label image to transform it to the space of original images. Figure 41a shows that HCV measurement via this method agrees well with the multi-atlas method shown in Figure 39c,d, (r=0.94). The Bland-Altman plot (Figure 41b) shows that although there was no evidence for a proportional bias (p=0.8), there was a systematic bias in that the mean difference between the two measurements is 7.8 mm^3. The 95% limits of agreement (1.96 SD from the mean) are ±4.62 mm^3, which indicates that there is good agreement between the two methods given the range of measurements is approximately 23 mm^3. The multi-atlas HCV and the segmentation-propagation HCV correlated with total brain volume in the control group (Figure 41c, r=0.93, p=0.001 and Figure 41c, r=0.9, p=0.002 respectively). Body weight correlated with

HCV for the multi-atlas method (Figure 41e, r=0.77, p=0.02) but was not significant for the segmentation-propagation method (Figure 41f, r=0.65, p=0.08).

6.12 Discussion

This study demonstrates that spatial normalisation and statistical parametric mapping can be used in order to localise differences between groups without the need for predefined anatomical labels and can therefore be used as a sensitive method of therapy monitoring if used in combination with meaningful parameters. The T_2 mapping in this study was subject to artifacts and therefore could not be used to determine conclusively whether EP reduced SE associated cerebral oedema. Nevertheless, the voxel-based relaxometry approach presented here shows that acute T_2 changes in the lithium-pilocarpine model affect certain subregions more than others therefore region-based approaches may be subject to reduced sensitivity and partial volume effects. Although the number of subjects was low, there was no evidence that EP was neuroprotective or detrimental based on hippocampal volume measurements. These results are contradictory to the results in a previous study that showed EP to be strongly protective against kainate induced seizures in mice(230) but could be attributed to the differences in the animal models or differences relating to the time point of drug administration. In the current study, the drug was administered 1 h following termination of SE, whereas Cho et al. administered the drug 12 h after the seizure. On the other hand, in the rat cerebral ischemia model the efficacy of the drug decreases with the time period between the insult and drug administration(231).

This is the first attempt to perform VBM in the rat lithium-pilocarpine model of epilepsy. One of the main strengths of VBM lies in its ability to identify very localised differences between groups. Regional differences in grey matter concentrations were found throughout the limbic regions as well as very localised parts of the thalamus, prefrontal and neocortex. Brain injury is not limited to the hippocampal formation in the lithium-pilocarpine model therefore grey matter density measurements using optimised VBM might be useful for assessing the efficacy of neuroprotective therapies. Alongside this VBM could be used to explain differences in cognitive impairment across animals and between groups. There are

some limitations of VBM that should also be noted here. One of these is that differences in grey matter density might result from a number of reasons and as such lower grey matter density might not be limited to neuronal loss. It could also be attributed to almost any biological change that results in abnormal signal intensity in T_2 weighted images and might be caused by gliosis in this model. Another limitation of VBM is that when brains are severely pathological, e.g. in subjects with enlarged ventricles, this could result in misclassification of tissue classes and the tissue classes being represented by an erroneous distribution of intensity values. This problem has been alleviated in the current work by using optimised VBM.

Group-wise registration using DARTEL method was also used to calculate hippocampal volumes and there was found to be good agreement between this and the multi-atlas method. A comparison was not made between these techniques and the gold standard i.e. manual segmentation. However, the stronger correlation in the control group between multi-atlas HCV, brain volume and body weight suggests that this method is superior to semi-automated segmentation-propagation.

Finally, this study found that 2D pulse sequences can also be used for the assessment of brain injury following SE as illustrated by the dramatic difference in rHCV between the Control and SE groups at just 2 weeks after SE. Using 2D sequences may enable shorter scan durations and therefore the possibility of using a larger number of subjects in preclinical therapy studies than would be possible with lengthy 3D acquisitions. Another advantage of 2D imaging is that it can be less sensitive to motion as the acquisition time is shorter and phase encoding, which is sensitive to motion is only performed in 1 direction. Longer TRs can be used in 2D sequences with the result that the acquired images are more T_2 weighted and therefore have greater contrast between grey matter, white matter and CSF. The main disadvantage is that the resolution in the slice direction is much lower, therefore the positioning of the imaging volume needs to be performed more accurately. In the future, the presence of multiple receiver coils and sensitivity encoding(232) could be used to circumvent these issues so that 3D imaging can be used to its full potential.

6.13 Conclusions

In conclusion, the first part of this chapter attempted to show that the corticosteroid dexamethasone could be used to modulate the expression of VCAM-1 and hence modulate the molecular imaging biomarker outlined in the previous chapter. Although the number of animals was low in these pilot studies, there was no evidence that this drug was able to modulate VCAM-1 expression. The second part of this chapter attempted find out if early dexamethasone treatment following SE could alleviate brain injury. It was shown that even low doses of dexamethasone worsen the regional effects that status epilepticus has on the brain. This may be a forewarning that if anti-inflammatory drugs such as corticosteroids are to be used in clinic during or following childhood status epilepticus as has been advocated(82), the type of drug and time course of administration are likely to be crucial. In the last part of this chapter, the anti-inflammatory drug ethyl pyruvate was tested for its potential as a neuroprotective agent. This drug was chosen as previous studies have shown that its efficacy is less sensitive to the time course of administration than other anti-inflammatory drugs due to its mechanism of action in which it suppresses the late inflammatory cytokine HMGB1. Little evidence was found to say that this drug was neuroprotective in the lithium-pilocarpine model. Despite this, data in this study were used to perform voxel-wise T_2 comparisons and voxel-based morphometry and was used to establish that these voxel-wise methods can be used in combination with volumetric imaging to provide information across the whole brain that is not restricted to predefined regions.

Chapter 7 Functional Connectivity

7.1 Aims

The preceding chapter demonstrated the power of structural MRI to detect seizure-induced brain injury and monitor neuroprotective strategies. The current chapter is concerned with seizure-induced changes in brain function and will test the hypothesis that functional connectivity is disrupted after status epilepticus.

7.2 Introduction

Functional connectivity (FC) can be defined as temporal correlations between spatially remote neurophysiological events(233). Functional connectivity is a useful concept as direct neuroanatomical connectivity does not necessarily imply correlations in neural activity and vice versa. Measuring neurophysiological events over time can be achieved using EEG, MEG (magnetoencephalography) or functional MRI (fMRI), albeit with different time resolutions for each of these methods. Recently it has been realised that measuring functional connectivity can be a powerful tool that can be used to aid in our understanding of the brain and its pathological states.

Even in the absence of prescribed tasks, the brain exhibits reproducible and measurable correlation in activity between different regions(234). This task-independent activity has been termed the ‘resting state’. Since this initial finding, there has been an explosion of interest in resting state functional MRI (rsfMRI), particularly in relation to understanding neurological diseases. Partly this interest has been fuelled by the convenience of the technique as it requires no experimental paradigm. The next section will describe how a technique called fMRI can be used as a surrogate marker for neuronal activity and the following sections will be concerned with how this has been used to observe FC in the epileptic brain.

7.3 Haemodynamic Response to Neural Activity

Local increases in neural activity can be indirectly detected using fMRI. The contrast mechanism in fMRI is thought to involve increases in energy demand which drive

local increases in cerebral blood flow. Alterations in blood flow in response to increases in energy demand is known as the haemodynamic response.

Deoxyhaemoglobin is paramagnetic and therefore higher concentrations lead to faster dephasing of magnetisation. Reductions in the concentration of deoxyhaemoglobin in the blood therefore cause an increase in signal intensity on gradient-echo (or spin-echo) images. This is the basis of the blood oxygen level-dependent (BOLD) contrast mechanism(235). Increases in neural activity leads to a haemodynamic response, which brings about an oversupply of oxygenated blood. As the supply in oxygenated blood exceeds demand, the result is a decrease in venous deoxyhaemoglobin levels, which leads to an increase in T_2* and therefore higher signal intensity on gradient echo images. Typically, the peak of stimulus-induced haemodynamic response is known to occur several seconds after the stimulus and fast imaging sequences such as echo-planar imaging (section 2.5) can be used to image events on this timescale.

7.4 Analysis of Resting State fMRI Data

As rsfMRI is a relatively new technique and as such there has yet to be a consensus on the most appropriate method of generating inferences about functional connectivity. Typical approaches fall under 4 different categories: seed-based correlation, ROI-based correlation, independent component analysis and graph theoretical approaches. These will be discussed in turn in the following sections.

7.4.1 Seed-Based Correlation

Seed-based correlation involves selection of a seed time course. This can be defined as the time course from an individual voxel, or the average time course across a ROI. This time series is then correlated to every other voxel in the brain. Using a seed-based method represents more of a hypothesis-driven approach to rsfMRI analyses. As noted by Constable et al., a reasonable starting point in epilepsy patients might be to use the suspected seizure focus as a seed ROI(236) to observe how its role has changed in the functional network.

7.4.2 ROI-Based Correlation

A ROI-based approach typically refers to correlating the time courses generated from pairs of ROIs. Clearly the difficulty with this method lies with the designation of the regions. A natural choice would be to use the anatomical regions as defined by an atlas. The danger with this approach is that it is possible that these anatomically defined regions do not represent functional regions, therefore other methods to define ROIs typically employ the use of task-based fMRI or independent component analysis, whilst more recent approaches use the voxel time series themselves to define ROIs(237).

7.4.3 Independent Component Analysis

Independent component analysis (ICA) represents a 'model-free approach' to the analysis of rsfMRI data. There are two major issues associated with using ICA, the first is that the number of components needs to be fixed at an estimated or an arbitrary value, and second that there is no consensus yet as to how to select components of interest. Typical methods to achieve component selection involve correlation with an atlas and/or measures involving the power spectrum of the time series(238).

7.4.4 Graph Theory

Graph theory-based approaches enable the quantitative characterisation of functional networks as a whole. Using graph theory the brain is modelled as a set of nodes which represent brain regions, and edges which represent the relationship between the nodes. In rsfMRI, the nodes can be defined as ROIs or as individual voxels and their edges can be characterised by how well the nodes correlate with one another. Weighted graphs have weights or distances associated with each of the edges e.g. the edge weights can be defined as the pairwise correlation efficient or these can be thresholded to give an unweighted graph. Given a set of nodes, edges and weights, several metrics can be calculated and the more commonly used ones will be briefly outlined below.

The degree of a node characterises how strongly it is connected to the rest of the graph and is defined as the number of edges directly connected to it. The connection

between two nodes i and j can be denoted as a_{ij}. Let a_{ij}=1 if nodes i and j are connected and a_{ij}=0 if otherwise. The degree (d) of node i can then be defined as $d(i)=\Sigma_j a_{ij}$. The strength of a node (in a weighted graph) also measures how closely a node is associated with the rest of the graph. It can be defined as the sum of all connection weights to a node i.e. the strength (s) of node i is defined as: $s(i)=\Sigma_j w_{ij}$, where w_{ij} is the weight of the edge between node i and j.

The average path length is a measure of how efficiently information is transferred across a network and is defined as the number of steps along the shortest path between any two nodes averaged across the entire graph. The clustering coefficient expresses the extent of local interconnectivity(239). For an unweighted graph it is the fraction of all possible nodes that exist within the neighbourhood of a node. For weighted graphs, a commonly adopted formula is the one derived by Onnela et al(240).

Constable et al. have recently reviewed the use of resting state fMRI in patients with partial epilepsy(241). This review discusses approaches to analysis that are based on correlation and graph theory. The authors conclude that modelling the entire degree distribution of each voxel in a fully connected graph can be used to summarise information about connectivity, thus taking into account both enhanced and reduced functional connectivity and at the same time circumventing the need for setting arbitrary thresholds for correlation coefficients in order to decide whether an edge exists or not. The measure that is proposed is termed the intrinsic connectivity distribution(242).

7.5 Functional Connectivity in Epilepsy

The interest in functional connectivity in the context of epilepsy stems from the fact that epilepsy is a network-based disorder. It is thought therefore that resting state fMRI could be used to predict outcomes following surgery in intractable epilepsy, the localisation of epileptogenic foci or predict the development of epilepsy. As the technique is relatively new, most studies to date have focussed on identifying differences between patient groups and controls. Despite rsfMRI being relatively free from experimental paradigms, comparisons between studies are hugely problematic because of the large range of preprocessing and analysis methods used.

Using the medial temporal structures as seeds for a seed-based correlation analysis, Pittau et al. found that patients with unilateral mTLE have decreased connectivity with the contralateral healthy mesial temporal structures(243). Bettus et al. found that left mTLE patients had decreased connectivity between the ipsilateral entorhinal cortex and the anterior hippocampus accompanied by increased connectivity between the contralateral anterior and posterior hippocampus(244). In patients with bilateral HS, Liao et al. observed significant increases in functional connectivity within the medial temporal structures and decreased connectivity within and between the frontal and parietal lobes(245). This study found patients to have abnormal graph theory metrics(7.4.4), such as a lower degree of connectivity, lower clustering coefficient and shorter path length compared to controls. Another study used graph theory metrics and supervised classification in order to elucidate the differences between mTLE patients and control subjects. Using a method of feature selection that is resistant to overfitting, they found it was possible to distinguish patients from controls with a sensitivity of 77% and a specificity of 83%(246). The most discriminating features were reduced strength and closeness of the right hippocampal node. Their study was based on a heterogeneous sample including patients with both right TLE and left TLE and therefore possibly underestimated the power of rsfMRI to distinguish patients from controls.

7.6 Resting State fMRI in Animal Models

The challenges involved in performing fMRI in rodents are typically greater than those in human studies, partly due to the need for stable physiology under anaesthesia. Many different anaesthetics have been tested for rsfMRI experiments and it is well-established that the pattern and strength of connectivity depends on the anaesthetic used. Recently, medetomidine(247, 248) or dexmedetomidine(249) have become the most popular choices for rsfMRI experiments. Studies that have used isoflurane suggest that functional connectivity shows a surprising dependence on the level of anaesthetic administered. Functional connectivity increases across the sensorimotor regions as the level of isoflurane is increased from 1% to 1.8%(250), but above 1.8%, spontaneous EEG activity is suppressed along with the synchronicity of the fMRI signal(251). Compared to medetomidine, rsfMRI experiments under 1.5% isoflurane exhibit higher ‘background’ correlations across

the whole brain and therefore seed-based correlations can be seen to exhibit much more widespread and less regional FC than under medetomidine(247). For this reason, medetomidine is frequently preferred over isoflurane for rsfMRI studies in rodents. Using ICA (section 7.4.3), Jonckers et al.(252) identified 9 meaningful and reproducible resting state 'networks' in rats anaesthetised with medetomidine, which were named based on their anatomical locations. These 9 components were: the motor cortex, somatosensory cortex, auditory cortex, retrosplenial cortex, hippocampus, striatum, cingulate cortex, visual cortex and inferior colliculus.

Only a handful of studies investigating functional connectivity in animal models of epilepsy have been reported. One such study looked at global network measures in the tetanus toxin rat model. In this model, tetanus toxin is administered to the right primary motor cortex. This manifests as spontaneous seizures for several weeks. Graph analysis showed an increase in global clustering coefficient and path length in the tetanus treated group which was accompanied by a decrease in interhemispheric connectivity(253).

7.7 Preprocessing of Images

Prior to any statistical analysis that is performed on fMRI data, there are several preprocessing steps that should be performed in order to attempt to remove sources of signal change that are not linked to haemodynamic changes. In reality, this is extremely difficult due to the inherent low signal-to-noise ratio of the technique. A typical sequence of pre-processing normally involves some or all of the following steps: brain extraction (masking), slice-timing correction, realignment (motion correction), unwarping (distortion correction), coregistration to an anatomical volume, normalisation to a standard space, regression of nuisance variables and spatial and/or temporal filtering. The following section will focus on realignment, nuisance variables and temporal filtering.

7.7.1 Realignment

Realignment is necessary as there is normally subject motion throughout the fMRI acquisition. Even in the situation in which there is no subject motion, changes in resonance frequency resulting from subject respiration could result in voxel shifts

along the phase encoding direction(254). This can be extremely problematic as small movements can cause large changes in signal intensity and it is commonplace to reject datasets that are unusable due to excessive motion. Realignment is usually performed using rigid registration to one of the images or to the mean image. This assumption that head motion occurs in a rigid manner is known to be flawed due to issues with slice timing(255). The realignment function in SPM8 was found to reduce the coefficient of variation (SD/mean) of a region in a single slice from 0.0236 in the raw data to 0.0226 post-realignment if performed on the entire 3D volume. However, the coefficient of variation was increased to 0.0237 if performed on the same single slice suggesting that multislice data is necessary for realignment to be performed.

7.7.2 Nuisance Variables

It is often assumed in fMRI studies that signals in the white matter and CSF are derived from non-neuronal sources e.g. physiological sources, scanner noise and motion etc. As these are of no interest in FC studies, they can be removed using regression so as not to lead to artificially high correlations in FC data. Global signal is also sometimes regressed out, however it is thought that this practice generates anti-correlations and therefore should not be used(256). It is also possible that there exists some collinearity between the nuisance variables, therefore orthogonalisation is sometimes performed prior to the linear regression. This is possible via the Gram-Schmidt process.

7.7.3 Temporal Filtering

Signals of interest in rsfMRI fall within the 0.01-0.1 Hz frequency range(234). Low-pass filtering of time series is often employed to minimise signal contributions from physiological sources. Slow alterations in signal (<0.01 Hz) are likely to be caused by changes in temperature or heart rate of the subject(248) or due to scanner instability(257). Removing low frequency drift can be achieved by detrending e.g. by fitting a low degree polynomial function to the data and retaining the residuals of the fit.

7.8 Study Design

In this study, it was hypothesised that status epilepticus leads to alterations in functional connectivity that can be detected using rsfMRI. Imaging was performed 2 weeks after the initial seizure in order to allow time for some degree of epileptogenesis to occur in SE rats. Longitudinal imaging was not possible due to the need for neuromuscular blockers. Isoflurane was chosen as the anaesthetic because even though medetomidine is typically the preferred anaesthetic (see section 7.6), previous studies in the department were performed under isoflurane and so the same protocol was used in order to allow for comparisons between these data. Furthermore, it is known that isoflurane suppresses seizure-like activity, which is not the case for medetomidine(258). The data included in this study were acquired as part of the same imaging session as the longitudinal imaging described in section 6.10.4.

Prior to performing the rsfMRI experiment, a forepaw stimulation experiment was performed using alpha-chloralose as the anaesthetic. The purpose of this experiment was to ensure that the imaging protocol and hardware was stable enough to be able to measure BOLD signal changes. Alpha-chloralose was used in this experiment as isoflurane is known to suppress the BOLD response under the conventionally used stimulation paradigm(259).

7.9 Materials and Methods

All procedures and protocols were performed in agreement with the policies established by the "*Animal Care Committee*" at Tohoku University, Sendai, Japan.

7.9.1 Forepaw Stimulation

In order to ensure that a BOLD signal response could be measured using the proposed imaging setup, a forepaw stimulation experiment was performed under alpha-chloralose anaesthesia. The anaesthetic protocol was previously optimised by Dr Sumiyoshi at Tohoku University(260) and consisted of a bolus injection of 80 mg/kg followed by continuous infusion (20 mg/kg/h, i.v.) of alpha-chloralose via a cannula inserted into the lateral tail vein. The animal was intubated and mechanically ventilated as in section 7.9.2. Pancuronium bromide (2 mg/kg/h, i.v.) was continuously infused via the tail vein cannula for muscle relaxation and reduction of

motion artifacts. A physiological monitoring system (SA Instruments, Stony Brook, NY) was used to monitor rectal body temperature. Temperature was maintained at 37±0.5°C using a water tubing warming system. Forepaw stimulation was performed by insertion of a pair of needle electrodes into the left forepaw. A block design was used with 10 blocks with each block comprising of 30 s stimulation and 40 s rest. Stimulation was implemented at a rate of 3 Hz, with a current of 2 mA and a pulse width 0.3 ms using a pulse generator (SEN-3401, Nihon Kohden) and isolator (SS-203J, Nihon Kohden). The SPM 8 t-test function was used to test the hypothesis that the stimulation condition > rest condition. For display purposes t-statistic maps were thresholded at $p<0.01$, family-wise error rate (FWE) corrected with a cluster extent threshold of 5 voxels. Gradient-echo EPI was used for functional imaging with the same parameters as in section 7.9.2.

7.9.2 Resting State fMRI

Rats were anaesthetised with 4% isoflurane in a 6:4 mixture of nitrogen and oxygen and were maintained on 1% isoflurane throughout the imaging protocol. The tail vein was cannulated and rats were intubated with a 19 gauge plastic cannula. Mechanical ventilation was performed at 60 breaths per minute with a tidal volume of 6-6.2 ml (SAR-830/AP, CWE Inc., Ardmore, PA, USA). Pancuronium bromide (2 mg/kg/h) was continuously infused via the tail vein cannula. Rats were secured in the MRI scanner using a bite-bar and surgical tape. A physiological monitoring system was used to monitor rectal body temperature. Temperature was maintained at 37±0.5°C using a water tubing warming system. Resting state fMRI was performed using a 7 T Bruker PharmaScan system (Bruker Biospin, Ettlingen, Germany) and a 38 mm diameter bird-cage receive/transmit coil. Shimming was at first instance done over the entire field of view and then over a voxel located in the brain using FASTMAP. fMRI was conducted using gradient-echo echo-planar imaging with the following parameters: TR=2 s, TE=15 ms, slice thickness=1.5 mm, matrix=70×35, number of volumes=300, dummy scans=4.

7.9.3 Spatial Normalisation

The average EPI image across all time points from each dataset was firstly interpolated in the slice direction to give a final voxel size of 400×400×750 µm. and

then brain extracted using the approach described in section 3.10 and then rigidly coregistered using NiftyReg to an EPI template using 6 free parameters(261). Following this, the new population specific mean image was calculated and each dataset was registered to this mean image using a 12 parameter affine registration. Registration to the mean image was performed 4 times and the mean image was updated after each iteration in order to create the population specific EPI template. The EPI data were transformed to this template using the calculated transformation matrices and were then smoothed in SPM 8 using a Gaussian filter of 0.8 mm full width at half maximum (FWHM).

7.9.4 Independent Component Analysis

Group ICA was performed using the Infomax algorithm in the GIFT toolbox (http://www.nitrc.org/projects/gift/). The default parameters were used and the number of components was fixed at 20. The weights of voxels for each ICA component were considered as random variables and a 1 sample t-test was performed in SPM 8 to test the null hypothesis that these weights significantly deviate from zero. These t-statistic maps were thresholded at $p<0.01$, uncorrected for multiple comparisons.

7.9.5 Seed-based Correlation

The nuisance covariates, which included the 6 realignment parameters and white matter time courses were orthogonalised with respect to each other using the Gram-Schmidt process. The data are displayed with and without including the global signal across the entire brain as a nuisance covariate. Each time series was normalised to have a mean of zero and unit variance and was detrended with a second order polynomial and filtered using a third order low pass Butterworth filter with a 0.1 Hz cutoff frequency. Seed-regions were chosen from the right cerebral hemisphere. Four regions were manually drawn on the normalised EPI template which included: the anterior hippocampus, thalamus, primary somatosensory cortex forelimb region and caudate putamen. The mean time-course across each region was correlated to every voxel in the brain using the Pearson product-moment correlation coefficient (r). For hypothesis testing, correlation coefficients were transformed using Fisher's r-to-z transformation.

7.9.6 Graph Theory Measures

Time courses were extracted from 20 different manually segmented regions: both right and left cingulate cortex (CG), primary motor cortex (M1), primary somatosensory cortex (S1), secondary somatosensory cortex (S2), caudate putamen (Cpu), anterior dorsal hippocampus (HippoAD), posterior hippocampus (HippoP), piriform cortex (Pir), corpus callosum (CC) and thalamus (Thal). Preprocessing was performed as in section 7.9.5, without global signal regression and each region was correlated to every other region to generate a correlation matrix. The correlation matrices for each subject were used as the weighted adjacency matrices. These matrices were not thresholded and so fully connected graphs were constructed. Two graph theory measures, strength and clustering coefficient were calculated using the brain connectivity toolbox(262) (https://sites.google.com/site/bctnet/). In order to obtain measures that are independent of differences in correlation across the entire network, 1000 surrogate random networks were calculated by randomly shuffling the edge weights and graph theory measures were normalised to the measures averaged over all 1000 random networks.

7.9.7 Statistical Analysis

(a) Graph Theory Measures

Statistical analysis was conducted on the normalised graph theoretical measures by using two-tailed randomisation tests. T-statistics were compared to the permutation distribution. The permutation distribution was found by calculating the t-statistic for 10000 random permutations of the dataset. Statistical significance was assigned at $p<0.05$. Correction for multiple comparisons was performed using the Benjamini-Hochberg procedure for false discovery rate (FDR) control(263).

(b) Seed-based correlation

Statistical analysis on seed-based correlation maps was performed without having removed the global signal component from the data as recommended by Gotts et al.(264). Hypothesis testing was done using two-sample t-tests in SPM 8 assuming unequal variance. Statistical significance was assessed on a voxel-wise basis using FDR<0.05 and a 3 voxel cluster extent threshold.

7.10 Results

7.10.1 Forepaw Stimulation

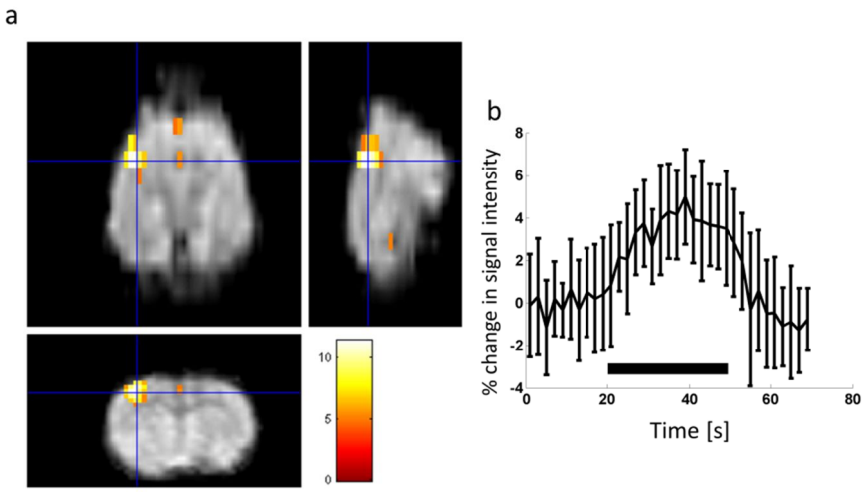

Figure 42: Forepaw stimulation experiment under alpha-chloralose anaesthesia. (a) SPM t-statistic map overlaid on a single EPI image. T-statistic map was thresholded at $p<0.01$, FWE corrected. (b) Signal change from baseline in the forelimb region of the left primary somatosensory cortex averaged across the 10 blocks, at rest (0-20 s and 50-70 s) and during stimulation (20-50 s, black bar). Error bars show ±standard deviation. (n=1).

The purpose of the forepaw stimulation experiment was to determine the feasibility of measuring a BOLD response using the proposed experimental setup. Figure 42a indicates that stimulation evokes a response in the contralateral primary somatosensory cortex forelimb region and Figure 42b shows there was a marked 4% change in signal intensity from baseline values.

7.10.2 Physiological Parameters

Arterial blood sampling was used to measure physiological parameters in one subject in each group before and after the rsfMRI experiment. The results are shown in Table 1. Rectal body temperature (T), heart rate (HR) and blood pressure (BP) were also recorded during the scan in the same subjects. For the control subject the average values across the EPI scan were: T=37ºC, HR=430 bpm and BP=117 mmHg. For the SE subject: T=36.5 ºC, HR=365 bpm and BP=133.5 mmHg.

	pH	pCO_2 (mmHg)	pO_2 (mmHg)	% O_2 sat
CTL before	7.42	41	103	97.8
CTL after	7.43	38	111	98.2
SE before	7.36	45	103	97.5
SE after	7.375	43	100	97.4

Table 1: Physiological parameters from arterial blood sampling before and after the rsfMRI experiment.

7.10.3 Motion Parameters

The average maximum displacement in any direction over the duration of the scan was 0.062±0.09 mm and 0.064±0.1 mm for the control and epilepsy group respectively (p=0.9). The maximum displacement was not greater than 0.12 mm (less than one third of a voxel) in any subject therefore no subjects were excluded from the analysis.

7.10.4 Independent Component Analysis in the Control Group

Group ICA was conducted only in the control group as an exploratory data analysis tool and out of the 20 fixed ICA components, 6 appeared to be ‘meaningful’ based on their time courses, interhemispheric symmetry and consistency with the literature(252). As noted in section 7.4.3, there is no well-established method to select ICA components and as such this is often carried out subjectively. These 6 components are displayed in Figure 43 for networks containing the: (a) striatum, (b) cingulate cortex, (c) somatosensory and motor cortex, (d) hippocampus, (e) thalamus and (f) piriform and entorhinal cortices.

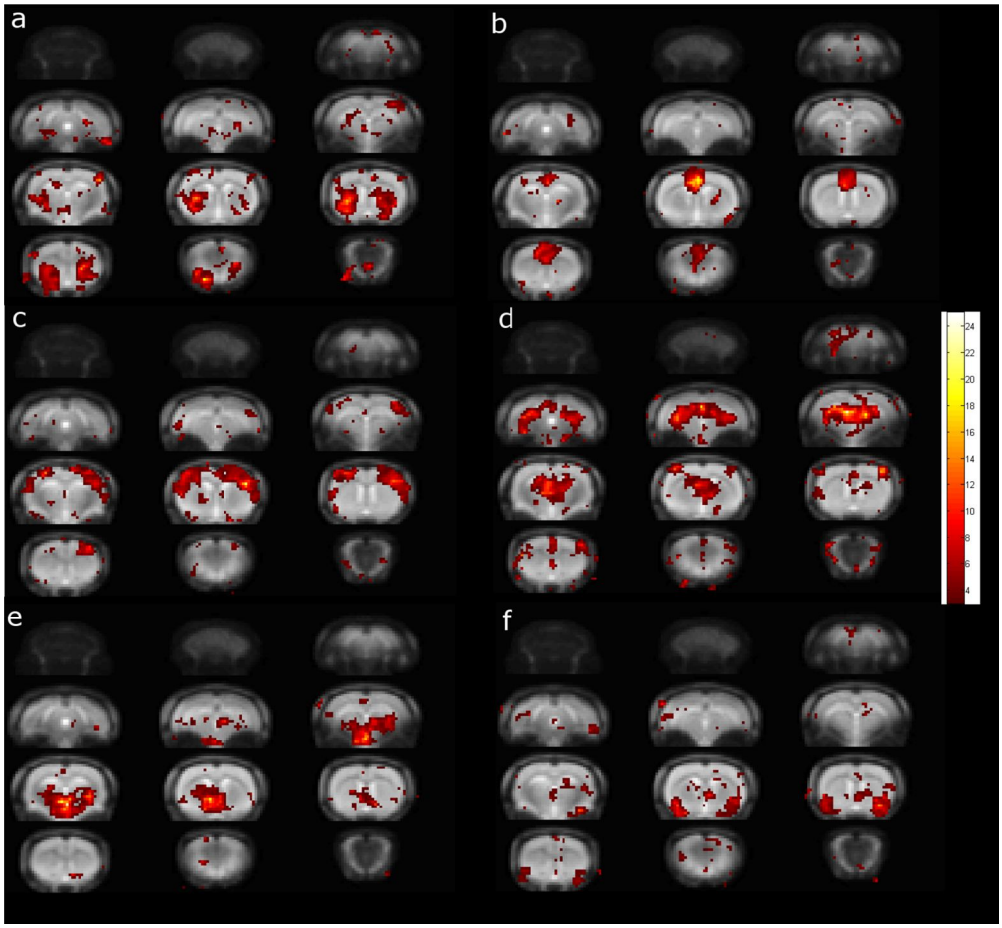

Figure 43: Functional connectivity maps resulting from group ICA of control subjects. T-statistic maps derived from one sample t-tests were overlaid on the EPI template. 6 components were identified corresponding to networks comprising primarily of the: (a) striatum, (b) cingulate cortex, (c) somatosensory and motor cortex, (d) hippocampus, (e) thalamus and (f) piriform and entorhinal cortices. T-statistic maps were thresholded at $p<0.01$ ($t>3$), uncorrected. (n=8).

7.10.5 Seed-based Correlation in the Control and SE groups

The comparison between the post-SE and control groups was conducted using seed-based and region-based correlation. Group ICA was not used for group comparisons because of the aforementioned issues associated with component selection. Figure 44 shows the average seed-based correlation coefficient maps (correlation maps) from the different seed regions without global signal regression. There appears to be highly widespread correlation in controls (Figure 44a,c,e,g,i) with a higher background correlation across all 5 seed regions compared to the epilepsy model (Figure 44b,d,f,h,j).

When global signal is regressed out (Figure 45), seed-based correlation maps appear to be remarkably similar between the two groups. As to be expected, the correlation maps with global signal regression resemble the group ICA components (Figure 43). With exception to the somatosensory seed region (Figure 45c,d), correlation maps from all seed regions exhibit clear correlations to the same contralateral brain structure.

7.10.6 Comparison between the Control and SE groups

T-tests were used to compare the two groups on the Fisher *z* transformed correlation maps. Only the anterior hippocampus and thalamus showed any significant voxels after FDR correction. Significantly reduced correlation can be observed in the SE group compared to controls using the hippocampal seed region. This reduced correlation can be seen in regions that are confined to the ipsilateral and contralateral hippocampus, piriform cortex, cingulate cortex, contralateral hypothalamus, entorhinal cortex and limited regions of the ipsilateral somatosensory cortex (Figure 46). Functional connectivity from the thalamus is reduced in regions that are confined only to the hypothalamus, ipsilateral cortex and ipsi- and contralateral piriform cortex (Figure 47). Remarkably, t-statistic maps comparing the two groups can be seen to exhibit a large degree of bilateral symmetry.

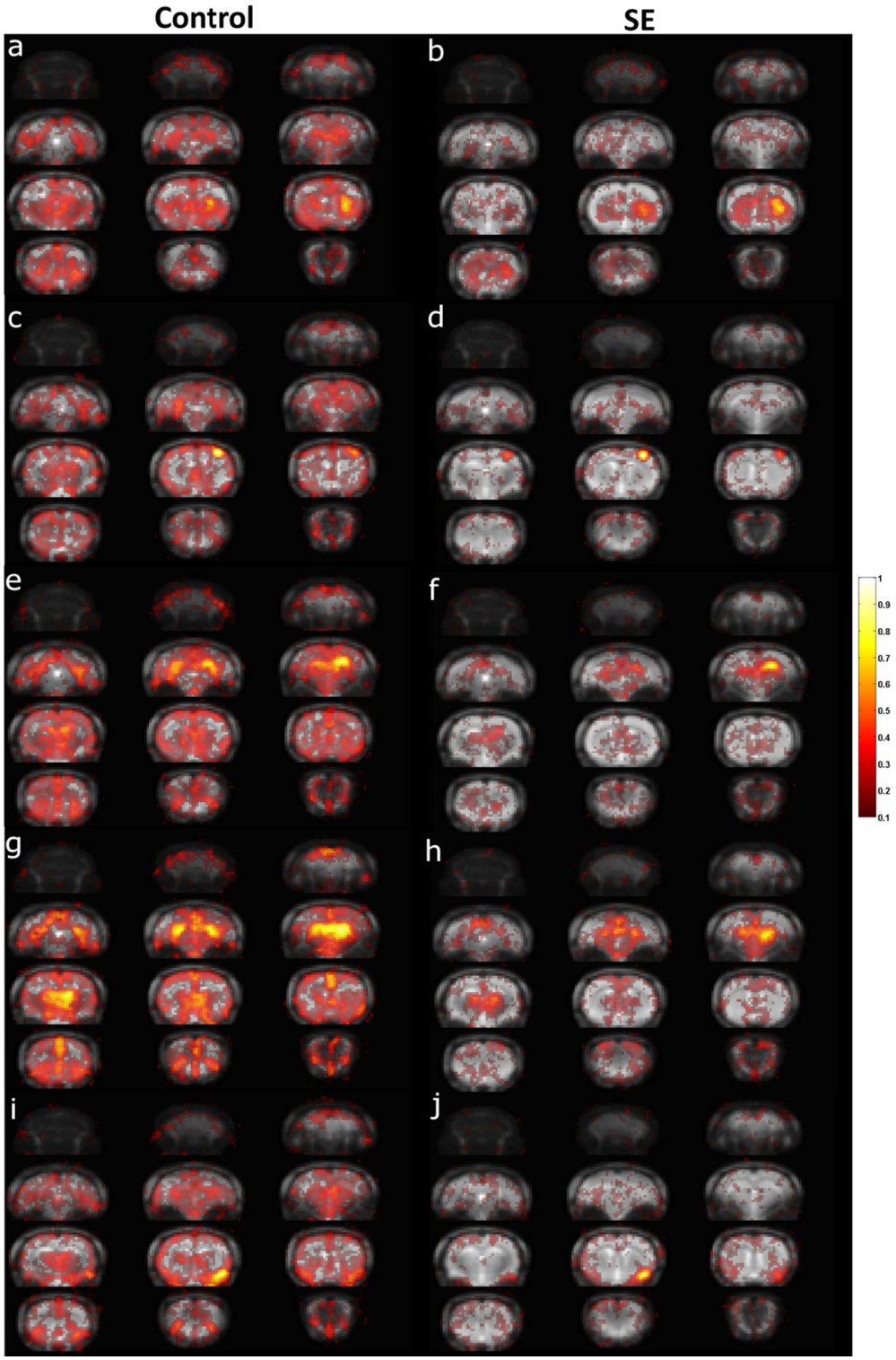

Figure 44: Mean seed-based correlation maps without global signal regression. Left column shows maps averaged across all control subjects (n=8) and the right column shows rats that underwent status epilepticus 2 weeks prior to imaging (n=11). All seed regions were chosen from the right cerebral hemisphere. (a)-(b) caudate putamen, (c)-(d) somatosensory cortex forelimb region, (e)-(f) anterior hippocampus (g)-(h) thalamus and (i)-(j) piriform cortex. Correlation maps are thresholded at r=0.1.

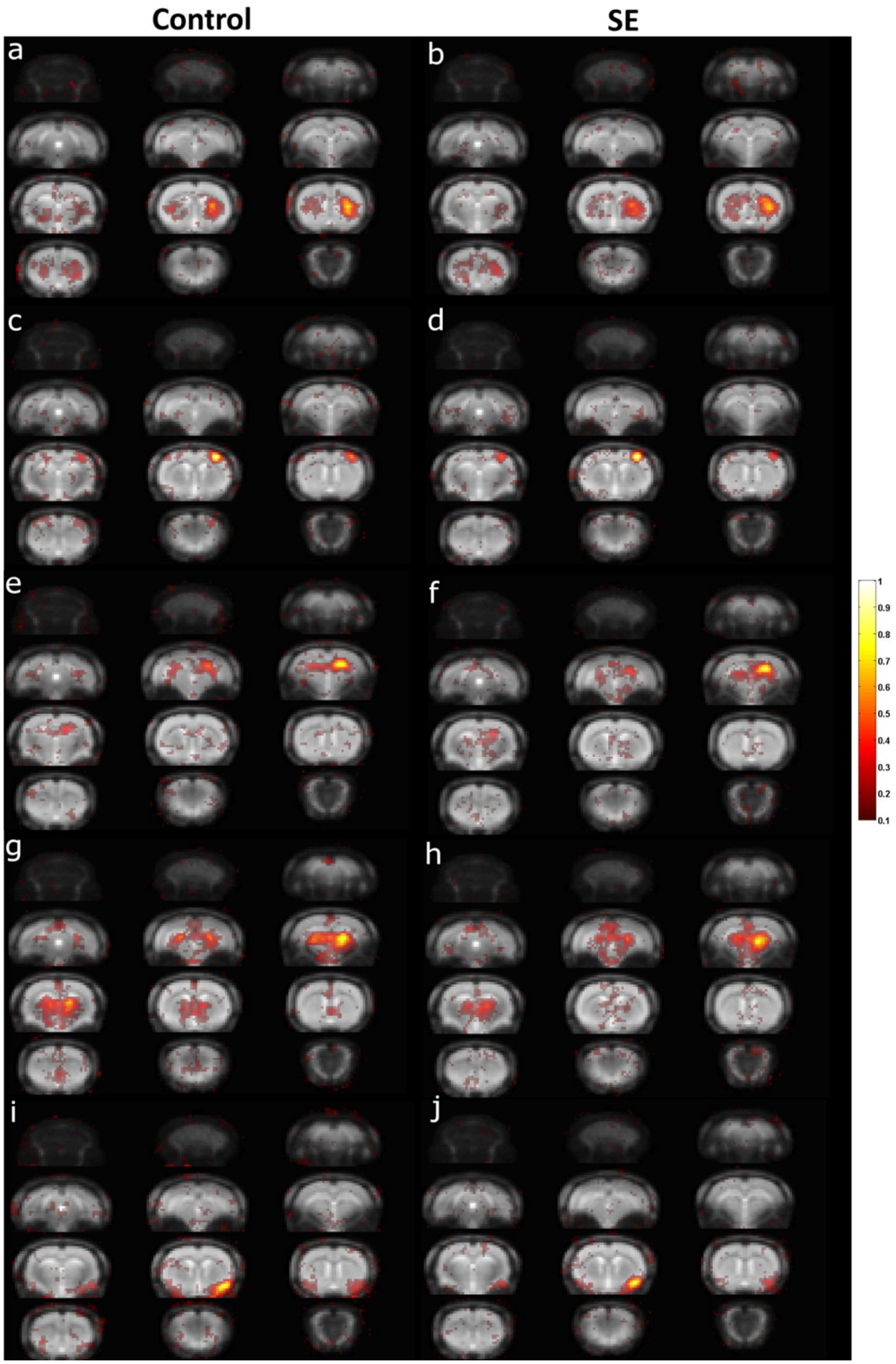

Figure 45: Mean seed-based correlation maps with global signal regression. Left column shows maps averaged across all control subjects (n=8) and the right column shows rats that underwent status epilepticus 2 weeks prior to imaging (n=11). All seed regions were chosen from the right cerebral hemisphere. (a)-(b) caudate putamen, (c)-(d) somatosensory cortex forelimb region, (e)-(f) anterior hippocampus (g)-(h) thalamus and (i)-(j) piriform cortex. Correlation maps are thresholded at r=0.1.

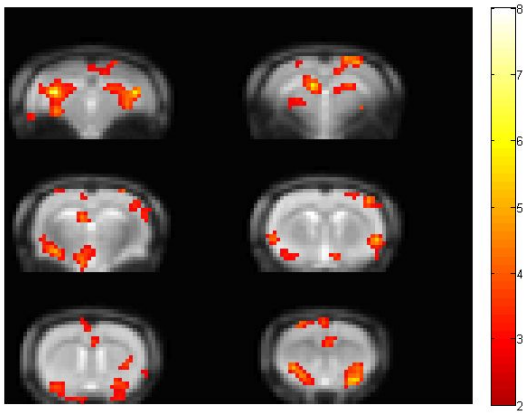

Figure 46: T-statistic map comparing the hypothesis that: CTL>SE for *z* correlation maps using the right anterior hippocampus as a seed region. Significance was assessed using voxel-wise FDR<0.05 and cluster extent threshold>3 voxels. CTL (n=8), SE (n=11).

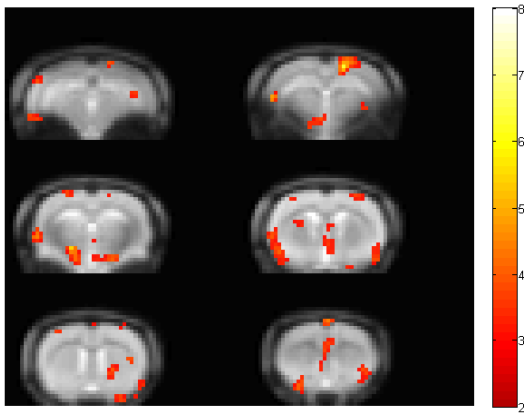

Figure 47: T-statistic map comparing the hypothesis that: CTL>SE for *z* correlation maps using the right thalamus as a seed region. Significance was assessed using voxel-wise FDR<0.05 and cluster extent threshold>3 voxels. CTL (n=8), SE (n=11).

7.10.7 Graph Theory Measures

The regions identified using ICA were identified, manually segmented on the EPI atlas and used in a graph theoretical analysis. The somatomotor regions were subdivided into M1, S1 and S2 and the hippocampus was divided into anterior and posterior.

No significant differences were observed in the global graph theory measures between the two groups. The normalised mean clustering coefficient across the whole network was 1.034±0.006 for controls and 1.026±0.007 for the SE group and the normalised average path length was 1.077±0.01 for controls and 1.076±0.01 for the SE group.

The unnormalised strength of all ROIs is higher in control subjects than the SE group (Figure 48a). Unnormalised strength in the white matter should be minimal because these signals were used as nuisance covariates. However, strength in these regions is closer to 1 than 0 as the right and left corpus callosum are strongly correlated with each other. Following normalisation no graph theory measures survived the FDR correction for multiple comparisons, therefore all p-values reported here are uncorrected. Strength is lower the SE group compared to controls in the right anterior hippocampus ($p=0.01$), left piriform cortex ($p=0.02$) and right thalamus ($p=0.03$) Figure 48d). The normalised clustering coefficient (NCC) was lower in the left piriform cortex in the SE group compared to controls ($p=0.02$). NCC was also lower in the right hippocampus and right thalamus but these did not reach statistical significance ($p=0.06$ and $p=0.05$). NCC was higher in the right motor cortex compared to controls ($p=0.02$).

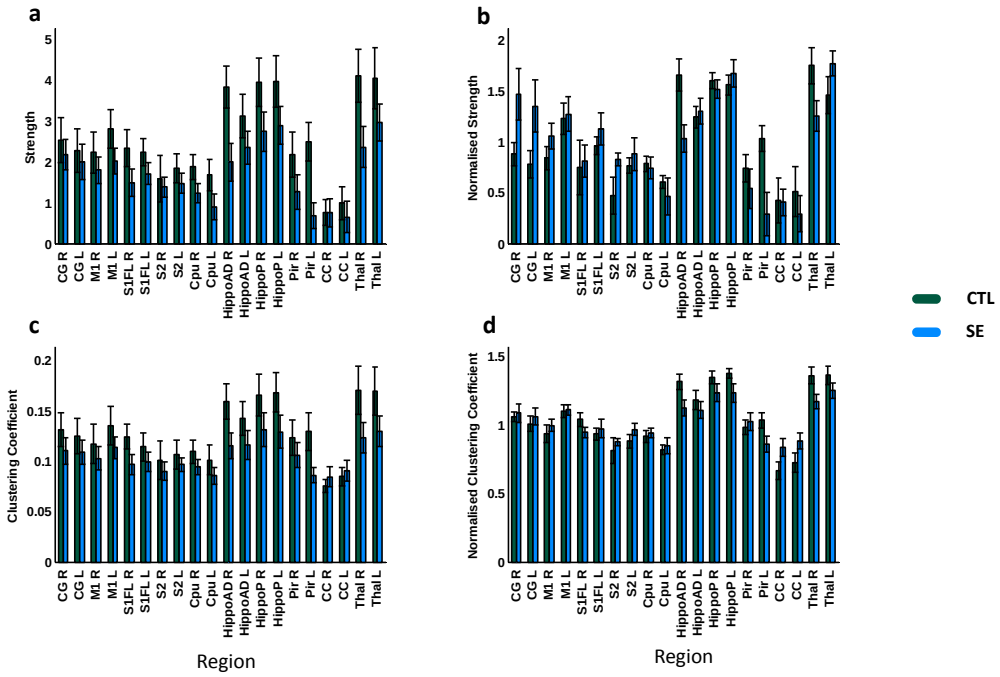

Figure 48: Graph theory measures in CTL and SE subjects. The first column shows unnormalised measures and the second column shows measures normalised to a surrogate random network. (a) Strength, (b) normalised strength, (c) clustering coefficient, (d) normalised clustering coefficient. Unnormalised strength and clustering coefficient is lower in the SE group. After normalisation, the strength is lower in the SE group in the right anterior hippocampus (HippoAD R), left piriform cortex (Pir L) and right thalamus (Thal R) compared to controls. Clustering coefficient was lower in the left piriform cortex but higher in the right motor cortex (M1 R) compared to controls. CTL (n=8), SE (n=11). Descriptive error bars are displayed as ±SEM.

7.11 Discussion

The main finding from this study is that differences in resting state fluctuations can be observed following lithium-pilocarpine induced SE. These occur primarily within the limbic regions but the thalamus and cortex are also affected. However, there are several limitations of this study that need to be addressed.

7.11.1 Study Limitations

Even though there was no significant difference in body weight between the two groups, it is possible that any differences between groups are caused by differences in systemic physiology. This is a limitation of the current study. However, the

physiology of the measured subjects was within the normal limits suggesting that the results are not artifactual. Another limitation of this study is that EEG was not measured therefore it is unknown whether any undesirable interictal spiking was present. Despite this, it is well known that isoflurane anaesthesia suppresses seizures as well as spikes in brain activity. Finally, the SE group had significant hippocampal volume loss (section 6.11.3). Although regions of CSF can largely be avoided when drawing ROIs, such a large and varying degree of atrophy may mean the coregistration to the EPI template might not perform as well for some of the MRI volumes in the SE group.

7.11.2 Independent Component Analysis

The functional connectivity networks identified using ICA agrees well with the literature. The striatal, sensorimotor, cingulate and hippocampal networks have also been observed by Jonckers et al.(252) under medetomidine. Kalthoff et al.(247), found that compared to medetomidine, the incidence of cortical and striatal networks is reduced in rats anaesthetised with 1.5% isoflurane. Similar to the current study, they also found no clear segregation of striatal and sensorimotor networks under isoflurane. In rats anaesthetised under 1% isoflurane, Hutchison et al.(265) observed all but one of the resting state networks that were found in the current study and to our knowledge, the component involving the piriform cortex has not previously been reported in the literature. This could be due to the fact that all other studies in rodent rsfMRI have employed surface receiver coils that exhibit steep drop-offs in sensitivity towards the ventral surface of the brain. The current study utilised a birdcage receiver coil that has a more homogeneous sensitivity across a larger imaging volume. In addition, Hutchison et al. found segregation of the primary, secondary, somatosensory and motor cortices. This was not observed in the current study but this could be because the number of components in their ICA analysis was fixed at twice the number of the current study.

7.11.3 Seed-based correlation

Previous studies in rats anaesthetised with isoflurane have demonstrated widespread correlation in seed-based analyses(266), which largely agrees with the results in the current study. In this study, significant reductions in functional connectivity were

found in the SE group compared to controls. Interestingly, the regions of reduced correlation are most dramatic in the regions that are known to be affected in the lithium-pilocarpine model e.g. the piriform cortex, entorhinal cortex, hippocampus and thalamus. This agrees with rsfMRI studies on mTLE patients which have found reduced correlation between the hippocampus and most other networks(267) as well as a more widespread disruption across most functional networks(268).

7.11.4 Graph Theory

There are only a few studies that have looked at FC in models of epilepsy. A study in the tetanus toxin rat model found increases in global normalised clustering coefficient and average path length(253), which contrasts with the current study as no difference in the global clustering coefficient or average path length could be observed here. However, the analysis method in the current study was different in that anatomical regions rather than single voxels were used as nodes.

Strength was lower in the right hippocampus, left piriform cortex and right thalamus in SE rats compared to controls, which shows some agreement with the seed-based analysis in which significant decreases in correlation were found in the SE group. In the graph-theory analysis, differences between groups were only observed unilaterally. This contrasts with the seed-based analysis and is difficult to reconcile with the structural imaging data which suggests alterations in this model are nearly always bilateral. The seed-based analysis highlights differences in functional connectivity between the two groups, whereas the significant differences did not survive correction for multiple comparisons in the graph theory analysis. This could be because averaging the signal over such large anatomically defined regions might eliminate some of the signals of interest and that ROIs should be smaller in order to characterise the FC network. Data-driven approaches, such as ICA, might be preferable and enable more functionally relevant designation of nodes than using anatomically defined boundaries.

7.11.5 Possible Explanations

There is a large degree of atrophy 2 weeks after lithium-pilocarpine induced SE (section 6.11.4). Therefore, it is possible that disruption in functional connectivity in the current study is partly due to neuronal loss or even a departure from normal

metabolism interfering with the haemodynamic response. On the other hand, significant decreases in correlation were observed between the thalamus and the neocortical regions, which are relatively preserved in this model (section 6.11.4). Atrophy in one brain region might also lead to widespread dysfunction in brain networks(268). In general, the effects of structural damage on functional connectivity are largely unknown(267). Such severe atrophy could obscure abnormal increases in functional connectivity and this might explain the discrepancy between increases in interictal synchronicity on EEG and decreases in fMRI in epilepsy subjects(269).

7.12 Conclusions

To our knowledge, this is the first study to observe differences in functional connectivity in the lithium-pilocarpine model of temporal lobe epilepsy. Significant reductions in correlations were observed in seed-based analyses from hippocampal and thalamic seed regions. These reductions occurred in the regions that are known to be affected in this model and exhibit noteworthy bilateral symmetry. Future work will be necessary to determine the relationship between functional connectivity measures, cognitive impairment and the development of epilepsy.

Chapter 8 Conclusions and Further Work

Chapter 1 summarised the dramatic progress that has been made in recent years in identifying new targets for anti-epileptogenic therapies. It also emphasised that finding biomarkers for therapy monitoring and epileptogenesis will be crucial in the search for new therapies. Recent advances in imaging methods have enabled the real possibility of identifying these biomarkers and it is almost certain that animal models and *in vivo* preclinical imaging will be instrumental in this pursuit.

Chapter 4 and Chapter 5 show that using iron oxide contrast agents for molecular imaging of VCAM-1 could be used as a meaningful biomarker for monitoring anti-inflammatory therapies. Using these contrast agents, Chapter 5 outlines the first demonstration of non-invasive imaging of VCAM-1 in an animal model of status epilepticus. As iron oxide is non-toxic and biodegradable there is potential that these iron oxide contrast agents can be used in a clinical setting either for therapy monitoring or for selecting suitable patients to undergo treatment. Several challenges will have to be overcome before this will be feasible. First, the biodistribution studies reported in Chapter 4 show that these particles may aggregate *in vivo* and become trapped in pulmonary vasculature. It was also found that blood clearance of micron-sized iron oxide particles is extremely rapid. Altering the physicochemical properties particles or coating with hydrophilic polymers could lead to improvements in contrast agent kinetics. Another approach to improve the sensitivity and specificity of these agents might be to use different targeting moieties, such as antibody fragments or peptides. Pretargeting strategies could be used, in which the contrast agent is conjugated to the targeting moiety *in vivo* using the biotin/streptavidin interaction. This pretargeting approach could prove to be especially advantageous for nuclear imaging in which high background signal could obscure the signal of interest.

The first part of Chapter 6 outlines experiments that attempted to use molecular imaging for the purpose of therapy monitoring. Anti-inflammatory therapies were administered after status epilepticus and imaging of VCAM-1 was performed 1 day later. These attempts at therapy monitoring proved unsuccessful i.e. there was no evidence that the anti-inflammatory drug dexamethasone reduced expression of VCAM-1. These results were extremely surprising but could be because

dexamethasone given acutely after SE does not modify expression of VCAM-1. Because of these unsuccessful attempts at therapy monitoring, follow-up experiments were planned which aimed to utilise more well-established imaging biomarkers for this purpose. T_2 relaxometry and volumetric imaging were chosen for this purpose because they are well accepted markers of oedema and brain injury.

Before starting a longitudinal study based on acquiring high resolution 3D images. The problems of data analysis needed to be considered. In order to ascertain volumetric measurements, image segmentation is required, which can be prohibitively laborious if this is attempted using manual methods. For this reason, automated methods of segmentation were employed.

Multi-atlas based segmentation was used for automated hippocampal volume and total brain volume measurements. Before being using to assess the drug therapies, it was first cross-validated and the results of this are displayed in Chapter 3. Chapter 6 shows that using well-established MRI techniques such as relaxometry and volumetric approaches can be coupled with automated analysis methods to efficiently screen neuroprotective strategies *in vivo* and longitudinally.

Imaging methods offer advantages over purely histological studies as they allow access to 3D data and to longitudinal data. If these imaging methods are combined with automated analysis methods, they can also be less labour intensive and cost effective. Longitudinal studies require fewer animals compared to cross-sectional studies and its wider adoption will hopefully lead to a reduction in the number of animals used in basic research and drug development in the future.

Using these automated analysis techniques, dexamethasone was tested for its ability to reduce brain injury following SE. The data conclusively demonstrated that dexamethasone had detrimental effects at two different doses. Furthermore, dexamethasone regionally exacerbated early brain oedema as well as delayed mortality. These data are feasible given recently published data in a rat model of TBI showing corticosteroids to exacerbate oedema when brain tissue is acidotic(206). This effect was found to be mediated by aquaporin-1 (ACP-1), as giving ACP-1 blockers reduced this effect. It would be interesting to determine if blocking ACP-1 also reduces this effect in the lithium-pilocarpine model.

Under non-acidotic conditions, Tran et al. found that dexamethasone improves oedema(206). Therefore a natural extension of the work presented in Chapter 6 would be to determine whether dexamethasone can be seen to have beneficial effects for SE of a shorter duration. This study could also determine if there is a relationship between outcome (after administering corticosteroids) and arterial blood pH levels. Another simple experiment could be performed to determine whether dexamethasone exacerbates or reduces the brain's inflammatory response by immunohistochemical staining for reactive astrocytes (glial fibrillary acidic protein). Given the worsening of oedema found in Chapter 6, it is likely that leakage of serum proteins will cause a worsening of gliosis and might even exacerbate the development of epilepsy.

The final part of Chapter 6 applies the aforementioned techniques to test another anti-inflammatory compound - ethyl pyruvate, which also did not prove to be efficacious in the rat lithium-pilocarpine model. Part III of Chapter 6 further discusses why spatial normalisation and voxel-wise statistics should be conducted alongside region-of-interest based approaches. The reasons for this are that brain injury in this model is not localised to the hippocampus so that hippocampal volumetry should be combined with voxel-based approaches. Another reason for using voxel-based approaches is that certain subregions are affected much more than others therefore region-based methods are likely to be less sensitive due to partial volume effects. Chapter 6 displays the first demonstration of voxel-based morphometry in an epilepsy animal model. VBM is based on a unified approach to tissue class image segmentation i.e. the bias field and the tissue classes are modelling in the same framework. It is extremely sensitive for detecting abnormal signal intensities, but this strength is also a limitation as the biological changes that are the basis for these abnormalities may be hard to interpret. New implementations of the SPM segmentation algorithm will make it possible to incorporate multispectral data (e.g. T_1, T_2, mean diffusivity etc.) as prior information and therefore they could improve the specificity of the technique.

The discrepancy in the literature between the efficacies of different anti-inflammatory drugs is disconcerting. The results depend to a large extent on which model of epileptogenesis is used and the time course of drug administration. This is exemplified by the recent study by Noe et al.(122) who coadministered the ICE

inhibitor - VX765 and an interleukin-1 receptor antagonist after electrically induced SE. They found this combination therapy to be neuroprotective in the electrical SE model but found there to be almost no effect in the lithium-pilocarpine model. They explained these findings by the more dramatic inflammatory response (number of IL-1β positive astrocytes) in the lithium-pilocarpine model. An extension of the work presented in this thesis would therefore be to test the effects of corticosteroids or EP in the electrically induced SE model. The effects of the combination treatment reported by Noe et al. appear to be regional i.e. the drug was most effective in the neocortex and CA1 region of the hippocampus. Therefore another possible future study could be to use a similar drug combination in the electrical SE model to determine whether voxel-based imaging methods can be used to detect these regional differences in treated and untreated groups *in vivo*.

Corticosteroids are currently used as a last-resort treatment in cases of super refractory status epilepticus(270). Further basic research will be necessary to determine whether these or other anti-inflammatory drugs should be translated to the clinic as a neuroprotective strategy. It is encouraging that studies which have found drugs to have limited or no efficacy are published. Despite this, there is a culture of not publishing negative results which may be ethically problematic if these same drugs are to be translated to the clinic and it is likely that a publication bias exists towards studies which have found positive outcomes(271, 272). Partly, this publication bias may arise from the need to ensure a rigorous safeguarding against type II errors(273).

Finally, as a component of the same study outlined in Chapter 6, functional connectivity is explored in Chapter 7. Although there has been rapidly expanding interest in applying resting state fMRI to patients with epilepsy, there has been a dearth of preclinical studies in this area due to the immense challenges involved. Preclinical studies should be able to disentangle the confounding factors from real effects in studies on functional connectivity. The study reported in Chapter 7 found reduced correlation in the SE group between the anterior hippocampus and the limbic regions of the brain as well as parts of the neocortex. Significant decreases in correlation were also observed between the thalamus and the piriform cortex along with similar regions of the cortex. It is possible that these findings were as a result of

the significant neuronal injury that is present at this time point in the lithium-pilocarpine model. Further analysis is required to determine the relationship between structure and function. More experimentation will be necessary to determine whether rsfMRI will be useful in predicting cognitive deficits or epileptogenesis.

For the purpose of predicting epileptogenesis, molecular imaging is likely to be one of the most powerful techniques available. On the other hand it is less clinically translatable compared to the already approved imaging methods. In the near future, currently available techniques should be employed to assess the feasibility of predicting brain injury and epilepsy. For example, intrinsic image contrast in MRI, (such as T_1, T_2, mean diffusivity etc.) could be coupled with voxel-based imaging methods and long-term electrophysiology to determine which parameters are predictive of SRS. A study of this nature has recently been reported by Kharatishvili et al.(63). An extension of their work would be to use more powerful supervised learning algorithms with better validation approaches to determine the generalizability of the model.

References:

1. Fisher RS, Boas WV, Blume W, Elger C, Genton P, Lee P, et al. Epileptic seizures and epilepsy: Definitions proposed by the International League against Epilepsy (ILAE) and the International Bureau for Epilepsy (IBE). Epilepsia. 2005;46(4):470-2.
2. Blume WT, Luders HO, Mizrahi E, Tassinari C, van Emde Boas W, Engel J, Jr. Glossary of descriptive terminology for ictal semiology: report of the ILAE task force on classification and terminology. Epilepsia. 2001;42(9):1212-8.
3. Bernasconi N, Bernasconi A, Caramanos Z, Antel SB, Andermann F, Arnold DL. Mesial temporal damage in temporal lobe epilepsy: a volumetric MRI study of the hippocampus, amygdala and parahippocampal region. Brain. 2003;126:462-9.
4. Fuerst D, Shah J, Shah A, Watson C. Hippocampal sclerosis is a progressive disorder: A longitudinal volumetric MRI study. Annals of Neurology. 2003;53(3):413-6.
5. Briellmann RS, Berkovic SF, Syngeniotis A, King MA, Jackson GD. Seizure-associated hippocampal volume loss: A longitudinal magnetic resonance study of temporal lobe epilepsy. Annals of Neurology. 2002;51(5):641-4.
6. Liu RSN, Lemieux L, Bell GS, Sisodiya SM, Bartlett PA, Shorvon SD, et al. Cerebral Damage in Epilepsy: A Population-based Longitudinal Quantitative MRI Study. Epilepsia. 2005;46(9):1482-94.
7. Wiebe S, Blume WT, Girvin JP, Eliasziw M, Effectiveness Efficiency Surgery T. A randomized, controlled trial of surgery for temporal-lobe epilepsy. New England Journal of Medicine. 2001;345(5):311-8.
8. Sadleir LG, Scheffer IE. Febrile seizures. British Medical Journal. 2007;334(7588):307-11.
9. Nelson KB, Ellenberg JH. Predictors of epilepsy in children who have experienced febrile seizures. New England Journal of Medicine. 1976;295(19):1029-33.
10. Annegers JF, Hauser WA, Shirts SB, Kurland LT. Factors prognostic of unprovoked seizures after febrile convulsions. N Engl J Med. 1987;316(9):493-8.
11. Walker MC, White HS, Sander J. Disease modification in partial epilepsy. Brain. 2002;125:1937-50.
12. Gastaut H. Classification of status epilepticus. Adv Neurol. 1983;34:15-35.
13. Delgado-Escueta AV, Bajorek JG. Status epilepticus: mechanisms of brain damage and rational management. Epilepsia. 1982;23 Suppl 1:S29-41.
14. Hesdorffer DC, Logroscino G, Cascino G, Annegers JF, Hauser WA. Risk of unprovoked seizure after acute symptomatic seizure: Effect of status epilepticus. Annals of Neurology. 1998;44(6):908-12.
15. Lemos T, Cavalheiro EA. Suppression of Pilocarpine-Induced Status Epilepticus and the Late Development of Epilepsy in Rats. Experimental Brain Research. 1995;102(3):423-8.
16. Dube CM, Ravizza T, Hamamura M, Zha QQ, Keebaugh A, Fok K, et al. Epileptogenesis Provoked by Prolonged Experimental Febrile Seizures: Mechanisms and Biomarkers. Journal of Neuroscience. 2010;30(22):7484-94.
17. Pujar SS, Neville BGR, Scott RC, Chin RFM, Network NLER. Death within 8 years after childhood convulsive status epilepticus: a population-based study. Brain. 2011;134:2819-27.

18. Hesdorffer DC, Shinnar S, Lewis DV, Moshe SL, Nordli DR, Jr., Pellock JM, et al. Design and phenomenology of the FEBSTAT study. Epilepsia. 2012;53(9):1471-80.
19. Martinos MM, Yoong M, Patil S, Chong WK, Mardari R, Chin RF, et al. Early developmental outcomes in children following convulsive status epilepticus: a longitudinal study. Epilepsia. 2013;54(6):1012-9.
20. Baulac M, Pitkänen A. Research priorities in epilepsy for the next decade—A representative view of the European scientific community: Summary of the ILAE Epilepsy Research Workshop, Brussels, 17–18 January 2008. Epilepsia. 2009;50(3):571-8.
21. Kwan P, Brodie MJ. Early identification of refractory epilepsy. N Engl J Med. 2000;342(5):314-9.
22. Helmstaedter C, Kurthen M, Lux S, Reuber M, Elger CE. Chronic epilepsy and cognition: A longitudinal study in temporal lobe epilepsy. Annals of Neurology. 2003;54(4):425-32.
23. Ortinski P, Meador KJ. Cognitive side effects of antiepileptic drugs. Epilepsy & Behavior. 2004;5, Supplement 1(0):60-5.
24. Loscher W. Animal models of epilepsy for the development of antiepileptogenic and disease-modifying drugs. A comparison of the pharmacology of kindling and post-status epilepticus models of temporal lobe epilepsy. Epilepsy Research. 2002;50(1-2):105-23.
25. Dube C, Richichi C, Bender RA, Chung G, Litt B, Baram TZ. Temporal lobe epilepsy after experimental prolonged febrile seizures: prospective analysis. Brain. 2006;129:911-22.
26. D'Ambrosio R, Fairbanks JP, Fender JS, Born DE, Doyle DL, Miller JW. Post-traumatic epilepsy following fluid percussion injury in the rat. Brain. 2004;127(Pt 2):304-14.
27. Blair RE, Deshpande LS, Holbert Ii WH, Churn SB, DeLorenzo RJ. Age-dependent mortality in the pilocarpine model of status epilepticus. Neuroscience Letters. 2009;453(3):233-7.
28. Maytal J, Shinnar S, Moshe SL, Alvarez LA. Low morbidity and mortality of status epilepticus in children. Pediatrics. 1989;83(3):323-31.
29. Albala BJ, Moshe SL, Okada R. Kainic-acid-induced seizures: a developmental study. Brain Res. 1984;315(1):139-48.
30. Scholl EA, Dudek FE, Ekstrand JJ. Neuronal degeneration is observed in multiple regions outside the hippocampus after lithium pilocarpine-induced status epilepticus in the immature rat. Neuroscience. 2013;252(0):45-59.
31. Curia G, Longo D, Biagini G, Jones RSG, Avoli M. The pilocarpine model of temporal lobe epilepsy. Journal of Neuroscience Methods. 2008;172(2):143-57.
32. Glien M, Brandt C, Potschka H, Voigt H, Ebert U, Loscher W. Repeated low-dose treatment of rats with pilocarpine: low mortality but high proportion of rats developing epilepsy. Epilepsy Research. 2001;46(2):111-9.
33. Gröticke I, Hoffmann K, Löscher W. Behavioral alterations in the pilocarpine model of temporal lobe epilepsy in mice. Experimental Neurology. 2007;207(2):329-49.
34. Marchi N, Fan QY, Ghosh C, Fazio V, Bertolini F, Betto G, et al. Antagonism of peripheral inflammation reduces the severity of status epilepticus. Neurobiology of Disease. 2009;33(2):171-81.
35. Foster AC, Mena EE, Monaghan DT, Cotman CW. Synaptic localization of kainic acid binding sites. Nature. 1981;289(5793):73-5.

36. Perl TM, Bedard L, Kosatsky T, Hockin JC, Todd ECD, Remis RS. An outbreak of toxic encephalopathy caused by eating mussels contaminated with domoic acid. New England Journal of Medicine. 1990;322(25):1775-80.
37. Cendes F, Andermann F, Carpenter S, Zatorre RJ, Cashman NR. Temporal-lobe epilepsy caused by domoic acid intoxication - evidence for glutamate receptor - mediated excitotoxicity in humans. Annals of Neurology. 1995;37(1):123-6.
38. Mazarati AM, Thompson KW, Suchomelova L, Sankar R, Shirasaka Y, Nissinen J, et al. Chapter 36 - Status Epilepticus: Electrical Stimulation Models. In: Asla P, Philip A. Schwartzkroin and Solomon L. MoshéA2 - Asla Pitkänen PAS, Solomon LM, editors. Models of Seizures and Epilepsy. Burlington: Academic Press; 2006. p. 449-VIII.
39. Sutula TP, Ockuly J. Chapter 32 - Kindling, Spontaneous Seizures, and the Consequences of Epilepsy: More Than a Model. In: Asla P, Philip A. Schwartzkroin and Solomon L. MoshéA2 - Asla Pitkänen PAS, Solomon LM, editors. Models of Seizures and Epilepsy. Burlington: Academic Press; 2006. p. 395-406.
40. Racine RJ. Modification of seizure activity by electrical stimulation. II. Motor seizure. Electroencephalogr Clin Neurophysiol. 1972;32(3):281-94.
41. Goffin K, Nissinen J, Van Laere K, Pitkanen A. Cyclicity of spontaneous recurrent seizures in pilocarpine model of temporal lobe epilepsy in rat. Exp Neurol. 2007;205(2):501-5.
42. Scimemi A, Semyanov A, Sperk G, Kullmann DM, Walker MC. Multiple and plastic receptors mediate tonic GABAA receptor currents in the hippocampus. The Journal of neuroscience. 2005;25(43):10016-24.
43. Chandler KE, Princivalle AP, Fabian-Fine R, Bowery NG, Kullmann DM, Walker MC. Plasticity of GABAB receptor-mediated heterosynaptic interactions at mossy fibers after status epilepticus. The Journal of neuroscience. 2003;23(36):11382-91.
44. Choy M, Cheung KK, Thomas DL, Gadian DG, Lythgoe MF, Scott RC. Quantitative MRI predicts status epilepticus-induced hippocampal injury in the lithium-pilocarpine rat model. Epilepsy Research. 2010;88(2-3):221-30.
45. Williams PA, White AM, Clark S, Ferraro DJ, Swiercz W, Staley KJ, et al. Development of Spontaneous Recurrent Seizures after Kainate-Induced Status Epilepticus. Journal of Neuroscience. 2009;29(7):2103-12.
46. Sloviter RS, Bumanglag AV. Defining “epileptogenesis” and identifying “antiepileptogenic targets” in animal models of acquired temporal lobe epilepsy is not as simple as it might seem. Neuropharmacology. 2013;69(0):3-15.
47. Sloviter RS. Hippocampal epileptogenesis in animal models of mesial temporal lobe epilepsy with hippocampal sclerosis: the importance of the "latent period" and other concepts. Epilepsia. 2008;49 Suppl 9:85-92.
48. Wasterlain CG, Fujikawa DG, Penix L, Sankar R. Pathophysiological mechanisms of brain-damage from Status Epilepticus. Epilepsia. 1993;34:S37-S53.
49. Epstein FH, Lipton SA, Rosenberg PA. Excitatory amino acids as a final common pathway for neurologic disorders. New England Journal of Medicine. 1994;330(9):613-22.
50. Wasterlain CG, Fujikawa DG, Penix L, Sankar R. Pathophysiological mechanisms of brain damage from status epilepticus. Epilepsia. 1993;34(s1):S37-S53.
51. Wasterlain CG. Mortality and morbidity from serial seizures. Epilepsia. 1974;15(2):155-76.

52. Fabene PF, Merigo F, Galie M, Benati D, Bernardi P, Farace P, et al. Pilocarpine-induced status epilepticus in rats involves ischemic and excitotoxic mechanisms. PLoS One. 2007;2(10):e1105.
53. Evans MC, Griffiths T, Meldrum BS. Kainic acid seizures and the reversibility of calcium loading in vulnerable neurons in the hippocampus. Neuropathol Appl Neurobiol. 1984;10(4):285-302.
54. Drislane FW. Who's Afraid of Status Epilepticus? Epilepsia. 2006;47(1):7-9.
55. Baram TZ, Jensen FE, Brooks-Kayal A. Does Acquired Epileptogenesis in the Immature Brain Require Neuronal Death? Epilepsy Currents. 2011;11(1):21-6.
56. Sloviter RS. The functional organization of the hippocampal dentate gyrus and its relevance to the pathogenesis of temporal lobe epilepsy. Annals of neurology. 1994;35(6):640-54.
57. Avoli M, D'Antuono M, Louvel J, Köhling R, Biagini G, Pumain R, et al. Network and pharmacological mechanisms leading to epileptiform synchronization in the limbic system in vitro. Progress in neurobiology. 2002;68(3):167-207.
58. Monaghan DT, Cotman CW. Distribution of N-methyl-D-aspartate-sensitive L-[3H]glutamate-binding sites in rat brain. J Neurosci. 1985;5(11):2909-19.
59. Ratzliff AH, Santhakumar V, Howard A, Soltesz I. Mossy cells in epilepsy: rigor mortis or vigor mortis? Trends in Neurosciences. 2002;25(3):140-4.
60. Sloviter RS, Zappone CA, Harvey BD, Bumanglag AV, Bender RA, Frotscher M. "Dormant basket cell" hypothesis revisited: relative vulnerabilities of dentate. J Comp Neurol. 2003;459(1):44-76.
61. Sloviter RS. Decreased hippocampal inhibition and a selective loss of interneurons in experimental epilepsy. Science. 1987;235(4784):73-6.
62. Bernard C, Esclapez M, Hirsch JC, Ben-Ari Y. Interneurones are not so dormant in temporal lobe epilepsy: a critical reappraisal of the dormant basket cell hypothesis. Epilepsy Research. 1998;32(1–2):93-103.
63. Kharatishvili I, Shan Z, She D, Foong S, Kurniawan N, Reutens D. MRI changes and complement activation correlate with epileptogenicity in a mouse model of temporal lobe epilepsy. Brain Structure and Function. 2013:1-24.
64. Pitkänen A, Nissinen J, Nairismägi J, Lukasiuk K, Gröhn OHJ, Miettinen R, et al. Progression of neuronal damage after status epilepticus and during spontaneous seizures in a rat model of temporal lobe epilepsy. In: Thomas Sutula AP, editor. Progress in Brain Research. Volume 135: Elsevier; 2002. p. 67-83.
65. Scott RC, King MD, Gadian DG, Neville BG, Connelly A. Hippocampal abnormalities after prolonged febrile convulsion: a longitudinal MRI study. Brain. 2003;126(Pt 11):2551-7.
66. Longo BM, Mello L. Blockade of pilocarpine- or kainate-induced mossy fiber sprouting by cycloheximide does not prevent subsequent epileptogenesis in rats. Neuroscience Letters. 1997;226(3):163-6.
67. Longo BM, Mello LEAM. Supragranular mossy fiber sprouting is not necessary for spontaneous seizures in the intrahippocampal kainate model of epilepsy in the rat. Epilepsy research. 1998;32(1):172-82.
68. Crespel A, Coubes P, Rousset MC, Brana C, Rougier A, Rondouin G, et al. Inflammatory reactions in human medial temporal lobe epilepsy with hippocampal sclerosis. Brain Res. 2002;952(2):159-69.
69. Maroso M, Balosso S, Ravizza T, Liu J, Aronica E, Iyer AM, et al. Toll-like receptor 4 and high-mobility group box-1 are involved in ictogenesis and can be targeted to reduce seizures. Nature Medicine. 2010;16(4):413-U91.

70. Ravizza T, Gagliardi B, Noe F, Boer K, Aronica E, Vezzani A. Innate and adaptive immunity during epileptogenesis and spontaneous seizures: Evidence from experimental models and human temporal lobe epilepsy. Neurobiology of Disease. 2008;29(1):142-60.
71. Wang S, Cheng Q, Malik S, Yang J. Interleukin-1beta inhibits gamma-aminobutyric acid type A (GABA(A)) receptor current in cultured hippocampal neurons. J Pharmacol Exp Ther. 2000;292(2):497-504.
72. Zeise ML, Espinoza J, Morales P, Nalli A. Interleukin-1beta does not increase synaptic inhibition in hippocampal CA3 pyramidal and dentate gyrus granule cells of the rat in vitro. Brain Res. 1997;768(1-2):341-4.
73. Zhang R, Yamada J, Hayashi Y, Wu Z, Koyama S, Nakanishi H. Inhibition of NMDA-induced outward currents by interleukin-1beta in hippocampal neurons. Biochem Biophys Res Commun. 2008;372(4):816-20.
74. Viviani B, Bartesaghi S, Gardoni F, Vezzani A, Behrens MM, Bartfai T, et al. Interleukin-1 beta enhances NMDA receptor-mediated intracellular calcium increase through activation of the Src family of kinases. Journal of Neuroscience. 2003;23(25):8692-700.
75. Rodgers KM, Hutchinson MR, Northcutt A, Maier SF, Watkins LR, Barth DS. The cortical innate immune response increases local neuronal excitability leading to seizures. Brain. 2009;132:2478-86.
76. Eriksson C, Tehranian R, Iverfeldt K, Winblad B, Schultzberg M. Increased expression of mRNA encoding interleukin-1β and caspase-1, and the secreted isoform of interleukin-1 receptor antagonist in the rat brain following systemic kainic acid administration. Journal of Neuroscience Research. 2000;60(2):266-79.
77. Rizzi M, Perego C, Aliprandi M, Richichi C, Ravizza T, Colella D, et al. Glia activation and cytokine increase in rat hippocampus by kainic acid-induced status epilepticus during postnatal development. Neurobiol Dis. 2003;14(3):494-503.
78. Blamire AM, Anthony DC, Rajagopalan B, Sibson NR, Perry VH, Styles P. Interleukin-1 beta-induced changes in blood-brain barrier permeability, apparent diffusion coefficient, and cerebral blood volume in the rat brain: A magnetic resonance study. Journal of Neuroscience. 2000;20(21):8153-9.
79. Mihály A, Bozóky B. Immunohistochemical localization of extravasated serum albumin in the hippocampus of human subjects with partial and generalized epilepsies and epileptiform convulsions. Acta Neuropathologica. 1984;65(1):25-34.
80. van Vliet EA, Araujo SD, Redeker S, van Schaik R, Aronica E, Gorter JA. Blood-brain barrier leakage may lead to progression of temporal lobe epilepsy. Brain. 2007;130:521-34.
81. David Y, Cacheaux LP, Ivens S, Lapilover E, Heinemann U, Kaufer D, et al. Astrocytic Dysfunction in Epileptogenesis: Consequence of Altered Potassium and Glutamate Homeostasis? Journal of Neuroscience. 2009;29(34).
82. Ravizza T, Balosso S, Vezzani A. Inflammation and prevention of epileptogenesis. Neuroscience Letters. 2011;497(3):223-30.
83. Pitkanen A, Lukasiuk K. Mechanisms of epileptogenesis and potential treatment targets. Lancet Neurology. 2011;10(2):173-86.
84. Galanopoulou AS, Buckmaster PS, Staley KJ, Moshe SL, Perucca E, Engel J, Jr., et al. Identification of new epilepsy treatments: Issues in preclinical methodology. Epilepsia. 2012;53(3):571-82.
85. Pitkanen A, Sutula TP. Is epilepsy a progressive disorder? Prospects for new therapeutic approaches in temporal-lobe epilepsy. Lancet Neurology. 2002;1(3):173-81.

86. Pitkanen A. Therapeutic approaches to epileptogenesis-Hope on the horizon. Epilepsia. 2010;51:2-17.
87. Schmidt D. Is antiepileptogenesis a realistic goal in clinical trials? Concerns and new horizons. Epileptic Disorders. 2012;14(2):105-13.
88. Blumenfeld H. New strategies for preventing epileptogenesis: Perspective and overview. Neuroscience Letters. 2011;497(3):153-4.
89. Mani R, Pollard J, Dichter MA. Human clinical trails in antiepileptogenesis. Neuroscience Letters. 2011;497(3):251-6.
90. Loescher W, Brandt C. Prevention or Modification of Epileptogenesis after Brain Insults: Experimental Approaches and Translational Research. Pharmacological Reviews. 2010;62(4):668-700.
91. Giblin KA, Blumenfeld H. Is Epilepsy a Preventable Disorder? New Evidence from Animal Models. Neuroscientist. 2010;16(3):253-75.
92. Kobow K, Auvin S, Jensen F, Loescher W, Mody I, Potschka H, et al. Finding a better drug for epilepsy: Antiepileptogenesis targets. Epilepsia. 2012;53(11):1868-76.
93. Scharfman H, Goodman J, Macleod A, Phani S, Antonelli C, Croll S. Increased neurogenesis and the ectopic granule cells after intrahippocampal BDNF infusion in adult rats. Experimental Neurology. 2005;192(2):348-56.
94. Paradiso B, Marconi P, Zucchini S, Berto E, Binaschi A, Bozac A, et al. Localized delivery of fibroblast growth factor-2 and brain-derived neurotrophic factor reduces spontaneous seizures in an epilepsy model. Proceedings of the National Academy of Sciences of the United States of America. 2009;106(17):7191-6.
95. Brandt C, Potschka H, Loscher W, Ebert U. N-methyl-D-aspartate receptor blockade after status epilepticus protects against limbic brain damage but not against epilepsy in the kainate model of temporal lobe epilepsy. Neuroscience. 2003;118(3):727-40.
96. Sacco RL, DeRosa JT, Haley EC, Jr., Levin B, Ordronneau P, Phillips SJ, et al. Glycine antagonist in neuroprotection for patients with acute stroke: GAIN Americas: a randomized controlled trial. Jama. 2001;285(13):1719-28.
97. Albers GW, Goldstein LB, Hall D, Lesko LM. Aptiganel hydrochloride in acute ischemic stroke: a randomized controlled trial. Jama. 2001;286(21):2673-82.
98. Davis SM, Lees KR, Albers GW, Diener HC, Markabi S, Karlsson G, et al. Selfotel in acute ischemic stroke : possible neurotoxic effects of an NMDA antagonist. Stroke. 2000;31(2):347-54.
99. Temkin NR. Antiepileptogenesis and seizure prevention trials with antiepileptic drugs: Meta-analysis of controlled trials. Epilepsia. 2001;42(4):515-24.
100. Lynch BA, Lambeng N, Nocka K, Kensel-Hammes P, Bajjalieh SM, Matagne A, et al. The synaptic vesicle protein SV2A is the binding site for the antiepileptic drug levetiracetam. Proceedings of the National Academy of Sciences of the United States of America. 2004;101(26):9861-6.
101. Margineanu DG, Matagne A, Kaminski RM, Klitgaard H. Effects of chronic treatment with levetiracetam on hippocampal field responses after pilocarpine-induced status epilepticus in rats. Brain Research Bulletin. 2008;77(5):282-5.
102. Brandt C, Glien M, Gastens AM, Fedrowitz M, Bethmann K, Volk HA, et al. Prophylactic treatment with levetiracetam after status epilepticus: Lack of effect on epileptogenesis, neuronal damage, and behavioral alterations in rats. Neuropharmacology. 2007;53(2):207-21.

103. Francois J, Germe K, Ferrandon A, Koning E, Nehlig A. Carisbamate has powerful disease-modifying effects in the lithium-pilocarpine model of temporal lobe epilepsy. Neuropharmacology. 2011;61(1-2):313-28.
104. Tang SJ, Reis G, Kang H, Gingras AC, Sonenberg N, Schuman EM. A rapamycin-sensitive signaling pathway contributes to long-term synaptic plasticity in the hippocampus. Proceedings of the National Academy of Sciences of the United States of America. 2002;99(1):467-72.
105. Zeng LH, Rensing NR, Wong M. The Mammalian Target of Rapamycin Signaling Pathway Mediates Epileptogenesis in a Model of Temporal Lobe Epilepsy. Journal of Neuroscience. 2009;29(21):6964-72.
106. Huang X, Zhang H, Yang J, Wu J, McMahon J, Lin Y, et al. Pharmacological inhibition of the mammalian target of rapamycin pathway suppresses acquired epilepsy. Neurobiol Dis. 2010;40(1):193-9.
107. Sunnen CN, Brewster AL, Lugo JN, Vanegas F, Turcios E, Mukhi S, et al. Inhibition of the mammalian target of rapamycin blocks epilepsy progression in NS‐Pten conditional knockout mice. Epilepsia. 2011;52(11):2065-75.
108. van Vliet EA, Forte G, Holtman L, den Burger JC, Sinjewel A, de Vries HE, et al. Inhibition of mammalian target of rapamycin reduces epileptogenesis and blood-brain barrier leakage but not microglia activation. Epilepsia. 2012;53(7):1254-63.
109. Buckmaster PS, Lew FH. Rapamycin suppresses mossy fiber sprouting but not seizure frequency in a mouse model of temporal lobe epilepsy. J Neurosci. 2011;31(6):2337-47.
110. Holtman L, van Vliet EA, van Schaik R, Queiroz CM, Aronica E, Gorter JA. Effects of SC58236, a selective COX-2 inhibitor, on epileptogenesis and spontaneous seizures in a rat model for temporal lobe epilepsy. Epilepsy Research. 2009;84(1):56-66.
111. Polascheck N, Bankstahl M, Loscher W. The COX-2 inhibitor parecoxib is neuroprotective but not antiepileptogenic in the pilocarpine model of temporal lobe epilepsy. Experimental Neurology. 2010;224(1):219-33.
112. Jung KH, Chu K, Lee ST, Kim J, Sinn DI, Kim JM, et al. Cyclooxygenase-2 inhibitor, celecoxib, inhibits the altered hippocampal neurogenesis with attenuation of spontaneous recurrent seizures following pilocarpine-induced status epilepticus. Neurobiology of Disease. 2006;23(2):237-46.
113. Serrano GE, Lelutiu N, Rojas A, Cochi S, Shaw R, Makinson CD, et al. Ablation of cyclooxygenase-2 in forebrain neurons is neuroprotective and dampens brain inflammation after status epilepticus. J Neurosci. 2011;31(42):14850-60.
114. Meijer O, De Lange E, Breimer D, De Boer A, Workel J, De Kloet E. Penetration of dexamethasone into brain glucocorticoid targets is enhanced in mdr1A P-glycoprotein knockout mice. Endocrinology. 1998;139(4):1789-93.
115. Rhen T, Cidlowski JA. Antiinflammatory action of glucocorticoids—new mechanisms for old drugs. New England Journal of Medicine. 2005;353(16):1711-23.
116. Cucullo L, Hallene K, Dini G, Dal Toso R, Janigro D. Glycerophosphoinositol and dexamethasone improve transendothelial electrical resistance in an in vitro study of the blood-brain barrier. Brain Research. 2004;997(2).
117. Bertorelli R, Adami M, Di Santo E, Ghezzi P. MK 801 and dexamethasone reduce both tumor necrosis factor levels and infarct volume after focal cerebral ischemia in the rat brain. Neuroscience Letters. 1998;246(1):41-4.

118. Marchi N, Granata T, Freri E, Ciusani E, Ragona F, Puvenna V, et al. Efficacy of Anti-Inflammatory Therapy in a Model of Acute Seizures and in a Population of Pediatric Drug Resistant Epileptics. Plos One. 2011;6(3).
119. Al-Shorbagy MY, El Sayeh BM, Abdallah DM. Diverse effects of variant doses of dexamethasone in lithium-pilocarpine induced seizures in rats. Canadian Journal of Physiology and Pharmacology. 2012;90(1):13-21.
120. Abbott NJ, Ronnback L, Hansson E. Astrocyte-endothelial interactions at the blood-brain barrier. Nat Rev Neurosci. 2006;7(1):41-53.
121. Ravizza T, Noe F, Zardoni D, Vaghi V, Sifringer M, Vezzani A. Interleukin Converting Enzyme inhibition impairs kindling epileptogenesis in rats by blocking astrocytic IL-1beta production. Neurobiol Dis. 2008;31(3):327-33.
122. Noe FM, Polascheck N, Frigerio F, Bankstahl M, Ravizza T, Marchini S, et al. Pharmacological blockade of IL-1β/IL-1 receptor type 1 axis during epileptogenesis provides neuroprotection in two rat models of temporal lobe epilepsy. Neurobiology of Disease. 2013;59(0):183-93.
123. Fabene PF, Mora GN, Martinello M, Rossi B, Merigo F, Ottoboni L, et al. A role for leukocyte-endothelial adhesion mechanisms in epilepsy. Nature Medicine. 2008;14(12):1377-83.
124. Katz R. Biomarkers and surrogate markers: an FDA perspective. NeuroRx. 2004;1(2):189-95.
125. Engel J, Jr. Biomarkers in epilepsy: introduction. Biomark Med. 2011;5(5):537-44.
126. Roch C, Leroy C, Nehlig A, Namer IJ. Predictive value of cortical injury for the development of temporal lobe epilepsy in 21-day-old rats: An MRI approach using the lithium-pilocarpine model. Epilepsia. 2002;43(10):1129-36.
127. Bragin A, Wilson CL, Almajano J, Mody I, Engel J, Jr. High-frequency oscillations after status epilepticus: epileptogenesis and seizure genesis. Epilepsia. 2004;45(9):1017-23.
128. Rigden JS. Quantum states and precession: The two discoveries of NMR. Reviews of modern physics. 1986;58(2):433.
129. Matt A. Bernstein KFK, Xiaohong Joe Zhou. Chapter 11 - Signal Acquisition and k-Space Sampling. In: Matt AB, Ph.D, Kevin FK, Xiaohong Joe Zhou PD, editors. Handbook of MRI Pulse Sequences. Burlington: Academic Press; 2004. p. 367-442.
130. Jackson GD, Berkovic SF, Tress BM, Kalnins RM, Fabinyi GC, Bladin PF. Hippocampal sclerosis can be reliably detected by magnetic resonance imaging. Neurology. 1990;40(12):1869-75.
131. Leite JP, Garcia-Cairasco N, Cavalheiro EA. New insights from the use of pilocarpine and kainate models. Epilepsy Res. 2002;50(1-2):93-103.
132. Chaudhary G, Malhotra J, Chaudhari JD, Gopinath G, Gupta YK. Effect of different lithium priming schedule on pilocarpine-induced status epilepticus in rats. Methods Find Exp Clin Pharmacol. 1999;21(1):21-4.
133. Heyn C, Bowen CV, Rutt BK, Foster PJ. Detection threshold of single SPIO-Labeled cells with FIESTA. Magnetic Resonance in Medicine. 2005;53(2):312-20.
134. Mills PH, Ahrens ET. Theoretical MRI contrast model for exogenous T-2 agents. Magnetic Resonance in Medicine. 2007;57(2):442-7.
135. Shapiro EM, Skrtic S, Koretsky AP. Sizing it up: Cellular MRI using micron-sized iron oxide particles. Magnetic Resonance in Medicine. 2005;53(2):329-38.
136. Grohn O, Pitkanen A. Magnetic resonance imaging in animal models of epilepsy - Noninvasive detection of structural alterations. Epilepsia. 2007;48:3-10.

137. Loubinoux I, Volk A, Borredon J, Guirimand S, Tiffon B, Seylaz J, et al. Spreading of vasogenic edema and cytotoxic edema assessed by quantitative diffusion and T2 magnetic resonance imaging. Stroke. 1997;28(2):419-26; discussion 26-7.
138. Neumann-Haefelin T, Kastrup A, de Crespigny A, Yenari MA, Ringer T, Sun GH, et al. Serial MRI after transient focal cerebral ischemia in rats: dynamics of tissue injury, blood-brain barrier damage, and edema formation. Stroke. 2000;31(8):1965-72; discussion 72-3.
139. Qiao M, Malisza KL, Del Bigio MR, Tuor UI. Correlation of cerebral hypoxic-ischemic T2 changes with tissue alterations in water content and protein extravasation. Stroke. 2001;32(4):958-63.
140. Knight RA, Ordidge RJ, Helpern JA, Chopp M, Rodolosi LC, Peck D. Temporal evolution of ischemic damage in rat brain measured by proton nuclear magnetic resonance imaging. Stroke. 1991;22(6):802-8.
141. Ordidge RJ, Helpern JA, Knight RA, Qing ZX, Welch KM. Investigation of cerebral ischemia using magnetization transfer contrast (MTC) MR imaging. Magn Reson Imaging. 1991;9(6):895-902.
142. Allen PS, Castro ME, Treiber EO, Lunt JA, Boisvert DP. A proton NMR relaxation evaluation of a model of brain oedema fluid. Phys Med Biol. 1986;31(7):699-711.
143. Coan AC, Bonilha L, Morgan PS, Cendes F, Li LM. T2-weighted and T2 relaxometry images in patients with medial temporal lobe epilepsy. J Neuroimaging. 2006;16(3):260-5.
144. Lebel RM, Wilman AH. Transverse relaxometry with stimulated echo compensation. Magnetic Resonance in Medicine. 2010;64(4):1005-14.
145. Miller AJ, Joseph PM. The Use of Power Images to Perform Quantitative-Analysis on Low SNR MR-Images. Magnetic Resonance Imaging. 1993;11(7):1051-6.
146. Rohlfing T, Brandt R, Menzel R, Maurer CR, Jr. Evaluation of atlas selection strategies for atlas-based image segmentation with application to confocal microscopy images of bee brains. Neuroimage. 2004;21(4):1428-42.
147. Sled JG, Zijdenbos AP, Evans AC. A nonparametric method for automatic correction of intensity nonuniformity in MRI data. Ieee Transactions on Medical Imaging. 1998;17(1):87-97.
148. Ashburner J, Friston KJ. Voxel-based morphometry - The methods. Neuroimage. 2000;11(6):805-21.
149. Tustison NJ, Avants BB, Cook PA, Zheng Y, Egan A, Yushkevich PA, et al. N4ITK: Improved N3 Bias Correction. Ieee Transactions on Medical Imaging. 2010;29(6):1310-20.
150. Yushkevich PA, Piven J, Hazlett HC, Smith RG, Ho S, Gee JC, et al. User-guided 3D active contour segmentation of anatomical structures: Significantly improved efficiency and reliability. Neuroimage. 2006;31(3):1116-28.
151. Arnold JB, Liow JS, Schaper KA, Stern JJ, Sled JG, Shattuck DW, et al. Qualitative and quantitative evaluation of six algorithms for correcting intensity nonuniformity effects. Neuroimage. 2001;13(5):931-43.
152. Nyul LG, Udupa JK, Zhang X. New variants of a method of MRI scale standardization. Ieee Transactions on Medical Imaging. 2000;19(2):143-50.
153. Jiehua L, Xiaofeng L, Jiachen Z, Gullapalli RP, Zara JM. A deformable surface model based automatic rat brain extraction method. 2011 8th IEEE

International Symposium on Biomedical Imaging : From Nano to Macro (ISBI 2011). 2011.
154. Uberti MG, Boska MD, Liu Y. A semi-automatic image segmentation method for extraction of brain volume from in vivo mouse head magnetic resonance imaging using Constraint Level Sets. Journal of Neuroscience Methods. 2009;179(2):338-44.
155. Murugavel M, Sullivan JM, Jr. Automatic cropping of MRI rat brain volumes using pulse coupled neural networks. Neuroimage. 2009;45(3):845-54.
156. Swathanthira Kumar MM, Sullivan JM, Jr. Automatic brain cropping enhancement using active contours initialized by a PCNN. Proceedings of the SPIE - The International Society for Optical Engineering. 2009;7259.
157. Chou N, Wu J, Bingren JB, Qiu A, Chuang K-H. Robust Automatic Rodent Brain Extraction Using 3-D Pulse-Coupled Neural Networks (PCNN). Ieee Transactions on Image Processing. 2011;20(9):2554-64.
158. Smith SM. Fast robust automated brain extraction. Human Brain Mapping. 2002;17(3):143-55.
159. Warfield SK, Zou KH, Wells WM. Simultaneous truth and performance level estimation (STAPLE): An algorithm for the validation of image segmentation. Ieee Transactions on Medical Imaging. 2004;23(7):903-21.
160. Ourselin S, Stefanescu R, Pennec X. Robust registration of multi-modal images: towards real-time clinical applications. Medical Image Computing and Computer-Assisted Intervention—MICCAI 2002. 2002:140-7.
161. Bobinski M, de Leon MJ, Wegiel J, DeSanti S, Convit A, Saint Louis LA, et al. The histological validation of post mortem magnetic resonance imaging-determined hippocampal volume in Alzheimer's disease. Neuroscience. 1999;95(3):721-5.
162. Klein A, Mensh B, Ghosh S, Tourville J, Hirsch J. Mindboggle: automated brain labeling with multiple atlases. BMC medical imaging. 2005;5:7-.
163. Artaechevarria X, Munoz-Barrutia A, Ortiz-de-Solorzano C. Combination Strategies in Multi-Atlas Image Segmentation: Application to Brain MR Data. Ieee Transactions on Medical Imaging. 2009;28(8):1266-77.
164. Heckemann RA, Hajnal JV, Aljabar P, Rueckert D, Hammers A. Automatic anatomical brain MRI segmentation combining label propagation and decision fusion. Neuroimage. 2006;33(1):115-26.
165. Cardoso JM, Leung K, Modat M, Keihaninejad S, Cash D, Barnes J, et al. STEPS: Similarity and Truth Estimation for Propagated Segmentations and its application to hippocampal segmentation and brain parcelation. Medical Image Analysis. 2013;17(6):671-84.
166. Rueckert D, Sonoda LI, Hayes C, Hill DLG, Leach MO, Hawkes DJ. Nonrigid registration using free-form deformations: Application to breast MR images. Ieee Transactions on Medical Imaging. 1999;18(8):712-21.
167. Pell GS, Briellmann RS, Waites AB, Abbott DF, Jackson GD. Voxel-based relaxometry: a new approach for analysis of T2 relaxometry changes in epilepsy. Neuroimage. 2004;21(2):707-13.
168. Ashburner J, Friston KJ. Unified segmentation. Neuroimage. 2005;26(3):839-51.
169. Ashburner J. A fast diffeomorphic image registration algorithm. Neuroimage. 2007;38(1):95-113.

170. McAteer MA, Sibson NR, von zur Muhlen C, Schneider JE, Lowe AS, Warrick N, et al. In vivo magnetic resonance imaging of acute brain inflammation using microparticles of iron oxide. Nature Medicine. 2007;13:1253-8.
171. Hoyte LC, Brooks KJ, Nagel S, Akhtar A, Chen RL, Mardiguian S, et al. Molecular magnetic resonance imaging of acute vascular cell adhesion molecule-1 expression in a mouse model of cerebral ischemia. Journal of Cerebral Blood Flow and Metabolism. 2010;30(6):1178-87.
172. Serres S, Mardiguian S, Campbell SJ, McAteer MA, Akhtar A, Krapitchev A, et al. VCAM-1-targeted magnetic resonance imaging reveals subclinical disease in a mouse model of multiple sclerosis. Faseb Journal. 2011;25(12):4415-22.
173. Montagne A, Gauberti M, Macrez R, Jullienne A, Briens A, Raynaud J-S, et al. Ultra-sensitive molecular MRI of cerebrovascular cell activation enables early detection of chronic central nervous system disorders. Neuroimage. 2012;63(2):760-70.
174. Akhtar AM, Chen Y, Schneider JE, Digby JE, McAteer MA, Wood K, et al. Magnetic Resonance Imaging Of Renal Ischemia Reperfusion Injury Using Microparticles Of Iron Oxide Targeting VCAM-1. Circulation. 2008;118(18):S555-S.
175. McAteer MA, Schneider JE, Ali ZA, Warrick N, Bursill CA, von zur Muhlen C, et al. Magnetic resonance imaging of endothelial adhesion molecules in mouse atherosclerosis using dual-targeted microparticles of iron oxide. Arteriosclerosis Thrombosis and Vascular Biology. 2008;28(1):77-83.
176. Akhtar AM, Schneider JE, Chapman SJ, Jefferson A, Digby JE, Mankia K, et al. In vivo quantification of VCAM-1 expression in renal ischemia reperfusion injury using non-invasive magnetic resonance molecular imaging. PloS one. 2010;5(9):e12800-e.
177. Elices MJ, Osborn L, Takada Y, Crouse C, Luhowskyj S, Hemler ME, et al. VCAM-1 on Activated Endothelium Interacts with the Leukocyte Integrin VLA-4 at a Site Distinct from the VLA-4 Fibronectin Binding-Site. Cell. 1990;60(4):577-84.
178. Serres S, Soto MS, Hamilton A, McAteer MA, Carbonell WS, Robson MD, et al. Molecular MRI enables early and sensitive detection of brain metastases. Proceedings of the National Academy of Sciences of the United States of America. 2012;109(17):6674-9.
179. Aller M-A, Arias J. Microsurgery in Liver Research: Bentham Science Publishers; 2009.
180. Romero IA, Prevost MC, Perret E, Adamson P, Greenwood J, Couraud PO, et al. Interactions between brain endothelial cells and human T-cell leukemia virus type 1-infected lymphocytes: Mechanisms of viral entry into the central nervous system. Journal of Virology. 2000;74(13):6021-30.
181. Duffy BA, Choy M, Riegler J, Wells JA, Anthony DC, Scott RC, et al. Imaging seizure-induced inflammation using an antibody targeted iron oxide contrast agent. Neuroimage. 2012;60(2):1149-55.
182. Stokes KY, Granger DN. Role of Nitric Oxide in Ischemia-Reperfusion Injury. In: Louis JI, editor. Nitric Oxide. San Diego: Academic Press; 2000. p. 633-47.
183. Fabene PF, Marzola P, Sbarbati A, Bentivoglio M. Magnetic resonance imaging of changes elicited by status epilepticus in the rat brain: diffusion-weighted and T2-weighted images, regional blood volume maps, and direct correlation with tissue and cell damage. Neuroimage. 2003;18(2):375-89.

184. Marchi N, Oby E, Batra A, Uva L, De Curtis M, Hernandez N, et al. In vivo and in vitro effects of pilocarpine: Relevance to ictogenesis. Epilepsia. 2007;48(10):1934-46.
185. Turski WA, Cavalheiro EA, Schwarz M, Czuczwar SJ, Kleinrok Z, Turski L. Limbic seizures produced by pilocarpine in rats - behavioural, electroencephalographic and neuropathological study. Behavioural Brain Research. 1983;9(3):315-35.
186. Paxinos G, Watson C. The rat brain in stereotaxic coordinates: hard cover edition: Access Online via Elsevier; 2006.
187. Riazi K, Galic MA, Pittman QJ. Contributions of peripheral inflammation to seizure susceptibility: Cytokines and brain excitability. Epilepsy Research. 2010;89(1):34-42.
188. Schulz M, Engelhardt B. The circumventricular organs participate in the immunopathogenesis of experimental autoimmune encephalomyelitis. Cerebrospinal Fluid Res. 2005;2:8.
189. Wuerfel E, Infante-Duarte C, Glumm R, Wuerfel JT. Gadofluorine M-enhanced MRI shows involvement of circumventricular organs in neuroinflammation. J Neuroinflammation. 2010;7:70.
190. Clifford DB, Olney JW, Maniotis A, Collins RC, Zorumski CF. The Functional-Anatomy and Pathology of Lithium Pilocarpine and High-Dose Pilocarpine Seizures. Neuroscience. 1987;23(3):953-68.
191. Toyoda I, Bower MR, Leyva F, Buckmaster PS. Early activation of ventral hippocampus and subiculum during spontaneous seizures in a rat model of temporal lobe epilepsy. The Journal of Neuroscience. 2013;33(27):11100-15.
192. Fernandes MJD, Dube C, Boyet S, Marescaux C, Nehlig A. Correlation between hypermetabolism and neuronal damage during status epilepticus induced by lithium and pilocarpine in immature and adult rats. Journal of Cerebral Blood Flow and Metabolism. 1999;19(2):195-209.
193. Handforth A, Treiman DM. Fucntional Mapping of the Early Stages of Status Epilepticus - a C-14 2-Deoxyglucose Study in the Lithium Pilocarpine Model in Rat. Neuroscience. 1995;64(4):1057-73.
194. Motte J, Fernandes MJD, Baram TZ, Nehlig A. Spatial and temporal evolution of neuronal activation, stress and injury in lithium-pilocarpine seizures in adult rats. Brain Research. 1998;793(1-2):61-72.
195. Librizzi L, Regondi MC, Pastori C, Frigerio S, Frassoni C, de Curtis M. Expression of adhesion factors induced by epileptiform activity in the endothelium of the isolated guinea pig brain in vitro. Epilepsia. 2007;48(4):743-51.
196. Turrin NP, Rivest S. Innate immune reaction in response to seizures: implications for the neuropathology associated with epilepsy. Neurobiology of Disease. 2004;16(2):321-34.
197. Zattoni M, Mura ML, Deprez F, Schwendener RA, Engelhardt B, Frei K, et al. Brain Infiltration of Leukocytes Contributes to the Pathophysiology of Temporal Lobe Epilepsy. Journal of Neuroscience. 2011;31(11):4037-50.
198. Andre V, Dube C, Francois J, Leroy C, Rigoulot MA, Roch C, et al. Pathogenesis and pharmacology of epilepsy in the lithium-pilocarpine model. Epilepsia. 2007;48:41-7.
199. Scott RC, Gadian DG, King MD, Chong WK, Cox TC, Neville BGR, et al. Magnetic resonance imaging findings within 5 days of status epilepticus in childhood. Brain. 2002;125:1951-9.

200. Choy M, Wells JA, Thomas DL, Gadian DG, Scott RC, Lythgoe MF. Cerebral blood flow changes during pilocarpine-induced status epilepticus activity in the rat hippocampus. Experimental Neurology. 2010;225(1):196-201.
201. Mishra AM, Bai H, Gribizis A, Blumenfeld H. Neuroimaging biomarkers of epileptogenesis. Neuroscience letters. 2011;497(3):194-204.
202. Vezzani A, French J, Bartfai T, Baram TZ. The role of inflammation in epilepsy. Nat Rev Neurol. 2011;7(1):31-40.
203. Shapira Y, Davidson E, Weidenfeld Y, Cotev S, Shohami E. Dexamethasone and indomethacin do not affect brain edema following head injury in rats. J Cereb Blood Flow Metab. 1988;8(3):395-402.
204. Altman D, Young R, Yagel S. Effects of dexamethasone in hypoxic-ischemic brain injury in the neonatal rat. Neonatology. 1984;46(3):149-56.
205. Mima T, Shigeno T. Lipocortin-1 fails to ameliorate cold-injury brain edema in the rat. Acta Neurochir Suppl. 2000;76:307-10.
206. Tran ND, Kim S, Vincent HK, Rodriguez A, Hinton DR, Bullock MR, et al. Aquaporin-1-mediated cerebral edema following traumatic brain injury: effects of acidosis and corticosteroid administration. J Neurosurg. 2010;112(5):1095-104.
207. Liu C, Guan J, Kang Y, Xiu H, Chen Y, Deng B, et al. Inhibition of dehydration-induced water intake by glucocorticoids is associated with activation of hypothalamic natriuretic peptide receptor-A in rat. PloS one. 2010;5(12):e15607-e.
208. Schwarz AJ, Danckaert A, Reese T, Gozzi A, Paxinos G, Watson C, et al. A stereotaxic MRI template set for the rat brain with tissue class distribution maps and co-registered anatomical atlas: application to pharmacological MRI. Neuroimage. 2006;32(2):538-50.
209. Ourselin S, Roche A, Subsol G, Pennec X, Ayache N. Reconstructing a 3D structure from serial histological sections. Image and Vision Computing. 2001;19(1-2):25-31.
210. Modat M, Ridgway GR, Taylor ZA, Lehmann M, Barnes J, Hawkes DJ, et al. Fast free-form deformation using graphics processing units. Computer Methods and Programs in Biomedicine. 2010;98(3):278-84.
211. Pinheiro J, Bates D, DebRoy S, Sarkar D. the R Development Core Team. nlme: Linear and Nonlinear Mixed Effects Models. R package version 3.1-105. The R Foundation for Statistical Computing. Vienna, Austria. 2013.
212. Roch C, Leroy C, Nehlig A, Namer IJ. Magnetic resonance imaging in the study of the lithium-pilocarpine model of temporal lobe epilepsy in adult rats. Epilepsia. 2002;43(4):325-35.
213. Lazovic J, Basu A, Lin H-W, Rothstein RP, Krady JK, Smith MB, et al. Neuroinflammation and Both Cytotoxic and Vasogenic Edema Are Reduced in Interleukin-1 Type 1 Receptor-Deficient Mice Conferring Neuroprotection. Stroke. 2005;36(10):2226-31.
214. Scott RC, King MD, Gadian DG, Neville BGR, Connelly A. Prolonged Febrile Seizures Are Associated with Hippocampal Vasogenic Edema and Developmental Changes. Epilepsia. 2006;47(9):1493-8.
215. Levin JR, Serrano G, Dingledine R. Reduction in delayed mortality and subtle improvement in retrograde memory. Epilepsia. 2012;53(8):1411-20.
216. Rolls A, Shechter R, Schwartz M. The bright side of the glial scar in CNS repair. Nat Rev Neurosci. 2009;10(3):235-41.
217. Holtman L, van Vliet EA, Edelbroek PM, Aronica E, Gorter JA. Cox-2 inhibition can lead to adverse effects in a rat model for temporal lobe epilepsy. Epilepsy Research. 2010;91(1):49-56.

218. Baik EJ, Kim EJ, Lee SH, Moon CH. Cyclooxygenase-2 selective inhibitors aggravate kainic acid induced seizure and neuronal cell death in the hippocampus. Brain Research. 1999;843(1-2):118-29.
219. Penkowa M, Molinero A, Carrasco J, Hidalgo J. Interleukin-6 deficiency reduces the brain inflammatory response and increases oxidative stress and neurodegeneration after kainic acid-induced seizures. Neuroscience. 2001;102(4):805-18.
220. Sherman DG, Bes A, Easton JD, Hacke W, Kaste M, Polmar SH, et al. Use of anti-ICAM-1 therapy in ischemic stroke - Results of the Enlimomab Acute Stroke Trial. Neurology. 2001;57(8):1428-34.
221. Edwards P, Arango M, Balica L, Cottingham R, El-Sayed H, Farrell B, et al. Final results of MRC CRASH, a randomised placebo-controlled trial of intravenous corticosteroid in adults with head injury - outcomes at 6 months. Lancet. 2005;365(9475):1957-9.
222. Munhoz CD, Lepsch LB, Kawamoto EM, Malta MB, Lima LD, Avellar MCW, et al. Chronic unpredictable stress exacerbates lipopolysaccharide-induced activation of nuclear factor-kappa B in the frontal cortex and hippocampus via glucocorticoid secretion. Journal of Neuroscience. 2006;26(14):3813-20.
223. Dinkel K, MacPherson A, Sapolsky RM. Novel glucocorticoid effects on acute inflammation in the CNS. Journal of Neurochemistry. 2003;84(4):705-16.
224. Cho IH, Kim SW, Kim JB, Kim TK, Lee KW, Han PL, et al. Ethyl pyruvate attenuates kainic acid-induced neuronal cell death in the mouse hippocampus. J Neurosci Res. 2006;84(7):1505-11.
225. Yu YM, Kim JB, Lee KW, Kim SY, Han PL, Lee JK. Inhibition of the cerebral ischemic injury by ethyl pyruvate with a wide therapeutic window. Stroke. 2005;36(10):2238-43.
226. Ulloa L, Ochani M, Yang H, Tanovic M, Halperin D, Yang R, et al. Ethyl pyruvate prevents lethality in mice with established lethal sepsis and systemic inflammation. Proceedings of the National Academy of Sciences. 2002;99(19):12351-6.
227. Valdés-Hernández PA, Sumiyoshi A, Nonaka H, Haga R, Aubert-Vásquez E, Ogawa T, et al. An in vivo MRI template set for morphometry, tissue segmentation, and fMRI localization in rats. Frontiers in neuroinformatics. 2011;5.
228. Mechelli A, Price CJ, Friston KJ, Ashburner J. Voxel-based morphometry of the human brain: Methods and applications. Current Medical Imaging Reviews. 2005;1(2):105-13.
229. Cremillieux Y, Ding S, Dunn JF. High-resolution in vivo measurements of transverse relaxation times in rats at 7 Tesla. Magn Reson Med. 1998;39(2):285-90.
230. Cho I-H, Kim S-W, Kim J-B, Kim T-K, Lee K-W, Han P-L, et al. Ethyl pyruvate attenuates kainic acid-induced neuronal cell death in the mouse hippocampus. Journal of Neuroscience Research. 2006;84(7).
231. Yu YM, Kim JB, Lee KW, Kim SY, Han PL, Lee JK. Inhibition of the cerebral ischemic injury by ethyl pyruvate with a wide therapeutic window. Stroke. 2005;36(10).
232. Pruessmann KP, Weiger M, Scheidegger MB, Boesiger P. SENSE: sensitivity encoding for fast MRI. Magn Reson Med. 1999;42(5):952-62.
233. Friston KJ, Frith CD, Liddle PF, Frackowiak RSJ. Functional Connectivity - The Principal-component analysis of large (PET) data sets. Journal of Cerebral Blood Flow and Metabolism. 1993;13(1):5-14.

234. Biswal B, Yetkin FZ, Haughton VM, Hyde JS. Functional connectivity in the motor cortex of the resting human brain using echo-planar mri. Magnetic Resonance in Medicine. 1995;34(4):537-41.
235. Ogawa S, Menon R, Kim S-G, Ugurbil K. On the characteristics of functional magnetic resonance imaging of the brain. Annual review of biophysics and biomolecular structure. 1998;27(1):447-74.
236. Constable RT, Scheinost D, Finn ES, Shen X, Hampson M, Winstanley FS, et al. Potential use and challenges of functional connectivity mapping in intractable epilepsy. Front Neurol. 2013;4:39.
237. Shen X, Tokoglu F, Papademetris X, Constable RT. Groupwise whole-brain parcellation from resting-state fMRI data for network node identification. NeuroImage. 2013;82(0):403-15.
238. McKeown MJ, Hansen LK, Sejnowsk TJ. Independent component analysis of functional MRI: what is signal and what is noise? Current Opinion in Neurobiology. 2003;13(5):620-9.
239. Wang J, Zuo X, He Y. Graph-based network analysis of resting-state functional MRI. Front Syst Neurosci. 2010;4:16.
240. Onnela JP, Saramaki J, Kertesz J, Kaski K. Intensity and coherence of motifs in weighted complex networks. Phys Rev E Stat Nonlin Soft Matter Phys. 2005;71(6 Pt 2):065103.
241. Constable RT, Scheinost D, Finn ES, Shen X, Hampson M, Winstanley FS, et al. Potential use and challenges of functional connectivity mapping in intractable epilepsy. Frontiers in neurology. 2013;4:39-.
242. Scheinost D, Benjamin J, Lacadie CM, Vohr B, Schneider KC, Ment LR, et al. The intrinsic connectivity distribution: a novel contrast measure reflecting voxel level functional connectivity. Neuroimage. 2012;62(3):1510-9.
243. Pittau F, Grova C, Moeller F, Dubeau F, Gotman J. Patterns of altered functional connectivity in mesial temporal lobe epilepsy. Epilepsia. 2012;53(6):1013-23.
244. Bettus G, Guedj E, Joyeux F, Confort-Gouny S, Soulier E, Laguitton V, et al. Decreased basal fMRI functional connectivity in epileptogenic networks and contralateral compensatory mechanisms. Human Brain Mapping. 2009;30(5):1580-91.
245. Liao W, Zhang Z, Pan Z, Mantini D, Ding J, Duan X, et al. Altered Functional Connectivity and Small-World in Mesial Temporal Lobe Epilepsy. PLoS ONE. 2010;5(1):e8525.
246. Zhang X, Tokoglu F, Negishi M, Arora J, Winstanley S, Spencer DD, et al. Social network theory applied to resting-state fMRI connectivity data in the identification of epilepsy networks with iterative feature selection. Journal of Neuroscience Methods. 2011;199(1):129-39.
247. Kalthoff D, Po C, Wiedermann D, Hoehn M. Reliability and spatial specificity of rat brain sensorimotor functional connectivity networks are superior under sedation compared with general anesthesia. NMR in Biomedicine. 2013;26(6):638-50.
248. Kalthoff D, Seehafer JU, Po C, Wiedermann D, Hoehn M. Functional connectivity in the rat at 11.7T: Impact of physiological noise in resting state fMRI. Neuroimage. 2011;54(4):2828-39.
249. Lu H, Zou Q, Gu H, Raichle ME, Stein EA, Yang Y. Rat brains also have a default mode network. Proceedings of the National Academy of Sciences. 2012;109(10):3979-84.

250. Liu X, Zhu XH, Zhang Y, Chen W. The change of functional connectivity specificity in rats under various anesthesia levels and its neural origin. Brain Topogr. 2013;26(3):363-77.
251. Liu X, Zhu X-H, Zhang Y, Chen W. Neural Origin of Spontaneous Hemodynamic Fluctuations in Rats under Burst–Suppression Anesthesia Condition. Cerebral Cortex. 2011;21(2):374-84.
252. Jonckers E, Van Audekerke J, De Visscher G, Van der Linden A, Verhoye M. Functional connectivity fMRI of the rodent brain: comparison of functional connectivity networks in rat and mouse. PloS one. 2011;6(4):e18876.
253. Otte WM, Dijkhuizen RM, van Meer MPA, van der Hel WS, Verlinde SAMW, van Nieuwenhuizen O, et al. Characterization of Functional and Structural Integrity in Experimental Focal Epilepsy: Reduced Network Efficiency Coincides with White Matter Changes. PLoS ONE. 2012;7(7):e39078.
254. Raj D, Paley DP, Anderson AW, Kennan RP, Gore JC. A model for susceptibility artefacts from respiration in functional echo-planar magnetic resonance imaging. Physics in Medicine and Biology. 2000;45(12):3809-20.
255. Bannister PR, Brady JM, Jenkinson M. Integrating temporal information with a non-rigid method of motion correction for functional magnetic resonance images. Image and Vision Computing. 2007;25(3):311-20.
256. Murphy K, Birn RM, Handwerker DA, Jones TB, Bandettini PA. The impact of global signal regression on resting state correlations: Are anti-correlated networks introduced? NeuroImage. 2009;44(3):893-905.
257. Bianciardi M, Fukunaga M, van Gelderen P, Horovitz SG, de Zwart JA, Shmueli K, et al. Sources of functional magnetic resonance imaging signal fluctuations in the human brain at rest: a 7 T study. Magn Reson Imaging. 2009;27(8):1019-29.
258. Airaksinen AM, Hekmatyar SK, Jerome N, Niskanen J-P, Huttunen JK, Pitkänen A, et al. Simultaneous BOLD fMRI and local field potential measurements during kainic acid–induced seizures. Epilepsia. 2012;53(7):1245-53.
259. Masamoto K, Kim T, Fukuda M, Wang P, Kim SG. Relationship between neural, vascular, and BOLD signals in isoflurane-anesthetized rat somatosensory cortex. Cereb Cortex. 2007;17(4):942-50.
260. Sumiyoshi A, Riera JJ, Ogawa T, Kawashima R. A mini-cap for simultaneous EEG and fMRI recording in rodents. NeuroImage. 2011;54(3):1951-65.
261. Schwarz AJ, Danckaert A, Reese T, Gozzi A, Paxinos G, Watson C, et al. A stereotaxic MRI template set for the rat brain with tissue class distribution maps and co-registered anatomical atlas: Application to pharmacological MRI. Neuroimage. 2006;32(2).
262. Zhou D, Thompson WK, Siegle G. MATLAB toolbox for functional connectivity. NeuroImage. 2009;47(4):1590-607.
263. Benjamini Y, Hochberg Y. Controlling the false discovery rate: a practical and powerful approach to multiple testing. Journal of the Royal Statistical Society Series B (Methodological). 1995:289-300.
264. Gotts SJ, Saad ZS, Jo HJ, Wallace GL, Cox RW, Martin A. The perils of global signal regression for group comparisons: a case study of Autism Spectrum Disorders. Front Hum Neurosci. 2013;7:356.
265. Hutchison RM, Mirsattari SM, Jones CK, Gati JS, Leung LS. Functional networks in the anesthetized rat brain revealed by independent component analysis of resting-state FMRI. Journal of neurophysiology. 2010;103(6):3398-406.

266. Williams KA, Magnuson M, Majeed W, LaConte SM, Peltier SJ, Hu X, et al. Comparison of α-chloralose, medetomidine and isoflurane anesthesia for functional connectivity mapping in the rat. Magnetic Resonance Imaging. 2010;28(7):995-1003.
267. Voets NL, Beckmann CF, Cole DM, Hong S, Bernasconi A, Bernasconi N. Structural substrates for resting network disruption in temporal lobe epilepsy. Brain. 2012;135(Pt 8):2350-7.
268. Cataldi M, Avoli M, de Villers-Sidani E. Resting state networks in temporal lobe epilepsy. Epilepsia. 2013;54(12):2048-59.
269. Bettus G, Ranjeva JP, Wendling F, Benar CG, Confort-Gouny S, Regis J, et al. Interictal functional connectivity of human epileptic networks assessed by intracerebral EEG and BOLD signal fluctuations. PLoS One. 2011;6(5):e20071.
270. Shorvon S, Ferlisi M. The treatment of super-refractory status epilepticus: a critical review of available therapies and a clinical treatment protocol. Brain. 2011;134(Pt 10):2802-18.
271. Sena ES, van der Worp HB, Bath PM, Howells DW, Macleod MR. Publication bias in reports of animal stroke studies leads to major overstatement of efficacy. PLoS Biol. 2010;8(3):e1000344.
272. ter Riet G, Korevaar DA, Leenaars M, Sterk PJ, Van Noorden CJ, Bouter LM, et al. Publication bias in laboratory animal research: a survey on magnitude, drivers, consequences and potential solutions. PLoS One. 2012;7(9):e43404.
273. Journal of Cerebral Blood Flow and Metabolism website. http://mc.manuscriptcentral.com/societyimages/jcbfm/JCBFM%20Guide%20to%20Authors.pdf [cited 2013 November 27].